

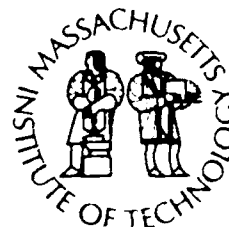
1

DTIC FILE COPY

Woods Hole Oceanographic Institution Massachusetts Institute of Technology



Joint Program
in Oceanography
and
Oceanographic Engineering



AD-A218 712

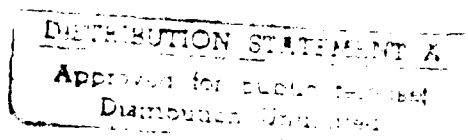
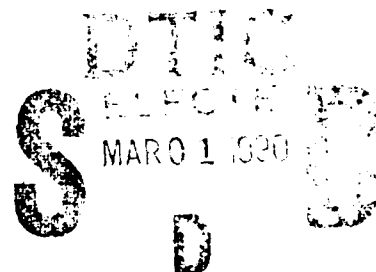
MASTER OF SCIENCE

Evaluation of GEOSAT Data and Application
to Variability of the Northeast Pacific Ocean

by

Jeffrey W. Campbell

October 1988



90 02 28 034

WHOI-88-40

**Evaluation of GEOSAT Data and Application to Variability
of the Northeast Pacific Ocean**

by

Jeffrey W. Campbell

Woods Hole Oceanographic Institution
Woods Hole, Massachusetts 02543

and

The Massachusetts Institute of Technology
Cambridge, Massachusetts 02139

October 1988

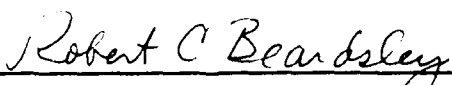
Master of Science Dissertation

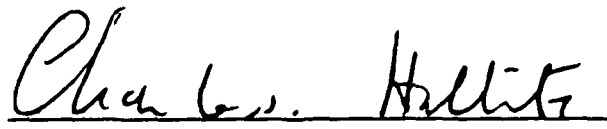
Support was provided by the United States Navy.

Reproduction in whole or in part is permitted for any purpose of the
United States Government. This thesis should be cited as:
Jeffrey W. Campbell, 1988. Evaluation of GEOSAT Data and
Application to Variability of the Northeast Pacific Ocean.
S.M. Thesis. MIT/WHOI, WHOI-88-40.

Approved for publication; distribution unlimited.

Approved for Distribution:


Robert C. Beardsley, Chairman
Physical Oceanography


Charles D. Hollister
Dean of Graduate Students

EVALUATION OF GEOSAT DATA
AND APPLICATION TO VARIABILITY OF
THE NORTHEAST PACIFIC OCEAN

by

Jeffrey William Campbell

B.S., Oceanography
United States Naval Academy
1982

SUBMITTED IN PARTIAL FULFILLMENT OF THE
REQUIREMENTS FOR THE DEGREE OF

MASTER OF SCIENCE

at the

MASSACHUSETTS INSTITUTE OF TECHNOLOGY

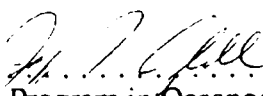
and the

WOODS HOLE OCEANOGRAPHIC INSTITUTION

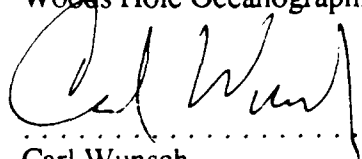
September, 1988

This thesis is not subject to U.S. copyright.

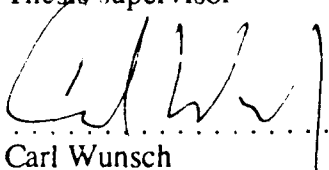
Signature of the Author


Joint Program in Oceanography,
Massachusetts Institute of Technology-
Woods Hole Oceanographic Institution, September 1988

Certified by


Carl Wunsch
Thesis supervisor

Accepted by


Carl Wunsch
Chairman, Joint Committee for Physical Oceanography,
Massachusetts Institute of Technology-
Woods Hole Oceanographic Institution

EVALUATION OF GEOSAT DATA
AND APPLICATION TO VARIABILITY OF
THE NORTHEAST PACIFIC OCEAN

by

Jeffrey William Campbell

Submitted to the Massachusetts Institute of Technology-
Woods Hole Oceanographic Institution Joint Program
in September, 1988 in partial fulfillment of the
requirements for the Degree of Master of Science

ABSTRACT

A portion of the northeast Pacific ocean was chosen within which to evaluate and use altimetric data from the U.S. Navy Geodetic Satellite GEOSAT. The zero-order accuracy of the major GEOSAT geophysical data record (GDR) channels was verified, and occasional gaps in the altimeter coverage were noted. GEOSAT'S 17-day repeat orbit allowed use of collinear-track processing to create profiles of the difference between the sea surface height along a given satellite repeat, and the mean sea surface height along that repeat's groundtrack. Detrending of sea surface bias and tilt on each repeat reduced orbit and other long wavelength errors in the difference profiles.

The corrections provided on the GEOSAT GDR were examined for their effects on the difference profiles of three test arcs. It was found that only the ocean tide, electromagnetic bias, and inverted barometer corrections varied enough over the arc lengths (~4400 km) to have any noticeable effect on the difference profiles. Only the ocean tide correction was accurate enough to warrant using it to adjust the sea surface heights. The recommended processing of GEOSAT data for the area included making the ocean tide correction, three-point block averaging successive sea surface heights, and forming the mean height profiles from 18 repeat cycles (to reduce aliasing of the M2 tidal component). A set of difference profiles for one GEOSAT arc indicated that a reasonable estimate of GEOSAT's system precision was ~4.5 cm (RMS). The mid wavelength range (100-500 km) of these profiles was found to be the only range in which oceanic mesoscale features could be separated from altimeter errors. *Theses 1.10*

Mean alongtrack wavenumber spectra of oceanic variability for two GEOSAT arcs were compared with a SEASAT-derived regional spectrum of Fu (1983). Agreement was good, with GEOSAT showing less system noise at short wavelengths, and greater oceanic variability at long wavelengths. The GEOSAT spectra were fit well by a $k^{-1.5}$ slope at wavelengths from 100 to 1000 km.

Sea surface temporal variability as a function of location was compared with the SEASAT results of Cheney et al. (1983). Qualitative agreement was excellent and quantitative differences were largely accounted for. GEOSAT picked up the variability of the major current systems of the northeast Pacific, including the Alaskan, Californian, and North Equatorial currents. Error bounds on GEOSAT-derived oceanic variability showed that the effects of uncorrected electromagnetic bias, inverted barometer, and wet troposphere were significant. Further work in the areas of error modelling, orbit determination, and geoid calculation were called for.

Thesis Supervisor: Dr. Carl Wunsch

Title: Cecil and Ida Green Professor of Physical Oceanography
Secretary of the Navy Research Professor

TABLE OF CONTENTS

ABSTRACT	1
CHAPTER 1: BACKGROUND	4
1.1 INTRODUCTION TO SATELLITE ALTIMETRY	5
1.2 OCEANOGRAPHY FROM ALTIMETRY	15
1.3 GEOGRAPHY AND TERMINOLOGY	21
1.4 THE GEOPHYSICAL DATA RECORD	22
1.5 SUMMARY	36
CHAPTER 1 FIGURES	38
CHAPTER 1 TABLES	51
CHAPTER 2: EVALUATING THE DATA	53
2.1 COLLINEAR PROCESSING SCHEMES	54
2.2 A COLLINEAR ALGORITHM	55
2.3 THE TEST ARCS	58
2.4 ARC 82	59
2.5 ARC 209	67
2.6 ARC 293	73
2.7 SUCCESSIVE POINT AVERAGING	83
CHAPTER 2 FIGURES	84
CHAPTER 2 TABLES	110
CHAPTER 3: USING THE DATA	114
3.1 OVERVIEW	115
3.2 VARIABILITY ON ARC 293	116
3.3 DATA COMPARISON	126
3.4 ERROR BOUNDS ON GEOSAT VARIABILITY CALCULATIONS	135
3.5 SUMMARY AND CONCLUSIONS	137
CHAPTER 3 FIGURES	142
APPENDIX A	156
REFERENCES	158
ACKNOWLEDGEMENTS	163

Accession No.	
NTIS GRA&I	<input checked="" type="checkbox"/>
DTIC TAB	<input type="checkbox"/>
Unannounced	<input type="checkbox"/>
Justification	
By	
Distribution	
Availability Codes	
Dist	
A-1	

CHAPTER ONE - BACKGROUND

1.1 INTRODUCTION TO SATELLITE ALTIMETRY

The purpose of this thesis is to evaluate data from the U.S. Navy altimetric satellite GEOSAT (Geodetic Satellite), and use that data to investigate oceanic variability in the northeast Pacific Ocean. In a broader sense, however, this thesis also acquaints the reader with the history, fundamentals, and limitations of satellite altimetry, as well as oceanographic uses to which altimetric data may be put. Sections 1.1 and 1.2 are directed to these background topics, while Sections 1.3 and beyond are devoted primarily to the evaluation and use of the GEOSAT data set.

The primary function of a satellite radar altimeter is to measure the distance between itself and the surface beneath it. This measurement, when combined with a determination of the satellite's position, allows the topography of that surface to be mapped. Radar beam scattering constraints limit the use of altimetric measurements to relatively smooth surfaces such as flatlands and ice fields. Most commonly, however, satellite altimetry is used to determine the changing topography of the sea surface, and that is the application to which this thesis is directed.

To lowest order, the sea surface lies along a gravitational equipotential surface known as the geoid. This equipotential may be thought of as that surface to which sea level would correspond if the oceans were at rest with respect to the earth and not subject to any wind or other forcing. The geoid varies by some ± 100 m worldwide, as a result of the earth's mass distribution; with its short wavelength undulations being primarily a function of bathymetry, and features of increasing horizontal scale reflecting conditions deeper in the earth (Stacey, 1977). The departure of the sea surface from the geoid is known as the sea surface topography and is usually less than 1-2 m in amplitude. Causes of such topography include the tides*, winds, atmospheric pressure changes, and current systems with their associated mesoscale features such as eddies (Stewart, 1985). With increased

* The tides also modify the geoid itself, as is discussed in the section on altimeter errors.

accuracy from the altimeter system, increasingly useful information about these features may be determined. For example, overall system accuracies of 1-2 m allow for a reasonable estimate of the geoid, while accuracies of several decimeters enable strong current systems such as the Gulf Stream and Kuroshio (with typical topography of >100 cm) to be tracked (Stewart, 1985). Repeated altimeter measurements of the same area, with instrument precisions of a few centimeters, may be processed so as to minimize the uncertainties due to orbit and geoid, and allow for observations of the variable surface geostrophic currents. These are typically associated with eddies and are manifested in topography with magnitudes of ten centimeters or more. Chapter 14 of Stewart (1985) contains a useful description of phenomena which influence the sea surface topography and is also highly recommended as an introduction to the field of altimetry. His excellent review of that discipline served as the basis for Section 1.1 of this work and uncited descriptions of altimetric methods found therein are credited to him.

The basic idea of an altimeter is straightforward. The altimeter transmits sharp radar pulses straight down to the sea surface, and the height of the satellite relative to the surface is determined from the travel time there and back. If the satellite's position relative to the center of the earth is also known, the absolute sea surface height with respect to the earth may be calculated. In addition, the return pulses' amplitude and shape give information about waves and winds at the sea surface. The former phenomenon is explored extensively in later passages.

The construction of workable altimeters requires several modifications of the basic theory, however. For example, while a sharp pulse is necessary to ensure good measurement precision, a long pulse can carry more radio energy and ensure a higher signal to noise ratio at the satellite receiver. To satisfy both criteria, altimeters use the technique of pulse compression (Rihaczek, 1969): The sharp pulse generated by the transmitter is lengthened by a dispersive filter prior to leaving the satellite, and is inverted to the original form upon its return.

Determining the arrival time of the return pulse with high accuracy requires an additional modification. From Fourier transform theory (see Bracewell [1986], Chapter 8), it can be shown that high time resolution requires a large pulse bandwidth. Unfortunately, the resolution needed to ensure height precisions of a few cm necessitates a bandwidth which is unacceptably large (Stewart [1985] links a measurement precision of 1 cm to a bandwidth of 30 GHz). This problem may be solved with the technique of pulse averaging, which maintains high measurement precision while allowing the use of narrowband pulses. The individual returns created by the reflection of each narrowband pulse off the wavecrests and troughs on the sea surface are plotted for received power as a function of time, within the tracking circuitry onboard the spacecraft. For a number of consecutive pulses averaged together, the set of returns will lie generally along a smooth waveform curve such as those shown in figure 1.1a. To reduce the noise in this curve, a large number of pulses must be averaged (according to the GEOSAT specifications in MacArthur et al. [1987], GEOSAT averages together around a hundred pulses for each height measurement). Travel time is reckoned from the half-power point on the leading edge of the averaged waveform, and is converted to height using the speed of the pulses. These calculations are computed onboard the satellite and stored with the spacecraft clock count.

The final modification of theory which is inherent in satellite altimeter design involves the extent of the sea surface illuminated by the radar pulse. For the altimeter to have sufficient horizontal resolution, this footprint size should be kept fairly small, and antenna theory gives two options. The first is the beam-limited situation whereby a narrow radar beam is used. A narrow beam requires a large and expensive antenna, as well as very good pointing accuracy. The second involves pulse-limiting whereby a fairly wide beam is used, but the pulses are kept short. With this technique, the returned power from a flat sea increases linearly with time until the trailing edge of the pulse reaches the water. Then, the radar footprint becomes a spreading annulus of constant area until the outer rim of the

annulus exceeds the beamwidth. The latter technique is the one used in altimetry, and is depicted in figure 1.1b.

Altimeter errors

Following Stewart (1985), altimeter errors may be divided into two categories: those which influence the actual altimeter measurement, and those which affect the interpretation of those measurements. Within the first category, instrument noise has been alluded to already. As has been mentioned, the limitation on pulse bandwidth requires the altimeter to determine the pulse travel time from the sloping front edge of a broad averaged waveform. This determination introduces error, as the shape of the waveform is uncertain due to the variability of the individual reflections from which it is determined. The variability is the main source of the instrument noise, and it increases with increasing significant wave height.* Instrument noise (often called measurement precision) is random in nature, of short wavelength (<10's of km), and is at the few cm level (RMS) in current generation altimeters. Correcting for it is not possible, though averaging successive sea surface height measurements together is an option for reducing it. This possibility is explored in the next chapter.

Of the remaining errors which influence the actual altimeter measurement, the most severe is the orbit error. Orbit error is a result of the calculated satellite position being different from the true satellite position. While various ground tracking stations fix the position of the altimeter at isolated spots, the vast majority of orbit determination is from ephemeris calculations. Sources of ephemeris error are discussed in Section 1.4, but their effects on the altimeter-derived sea surface topography are easily understood. For example, if the satellite is actually higher than calculated, the measured distance to the ocean will be larger than it should be for the alleged position, and the sea surface will be calculated to be lower than it really is. Alongtrack errors, whether produced by ephemeris

* Significant wave height (SWH) is defined as the average height of the highest third of the waves at a point, and is about 4 times the RMS wave height (Fedor and Brown, 1982).

or clock error, also result in height error, as the satellite possesses a vertical velocity component with respect to the ocean surface (mainly due to the ellipticity of the orbit). Altogether, orbit error accounts for an RMS error in the current GEOSAT sea surface heights of about 3 m (Born, 1988). Fortunately, the alongtrack error wavelength is very large; tending to be once per orbit (see Douglas and Goad [1978]), so the orbit error over short distances on the ocean surface may be greatly reduced by methods discussed later in this chapter.

Satellite attitude is another factor influencing the altimeter measurement. Essentially, off-nadir altimeter pointing results in the distance to the surface being calculated as too large. Current generation altimeters such as GEOSAT are able to correct for this through waveform analysis, however, because off-nadir pointing causes the slope of the trailing portion of the return waveform to decrease. This change in slope is calculated and used to correct the altimeter measurement (MacArthur et al., 1987).

Surface waves influence the altimeter measurement in a number of ways. As alluded to earlier, the shape of a return pulse is a function of its reflection history off the peaks and valleys of the wave-modified sea surface. As the significant wave height increases, the individual reflections will be more spread out in time and the leading edge of the final waveform will be less steep, making it more difficult to find the half-power point. In addition, the irregularity of the sea surface caused by waves is a major source of the instrument noise discussed earlier. Finally, high significant wave height will cause the spherically expanding radar pulses to intersect the sea surface at more distant radii from the beam center than would occur with a flat sea. The radar footprint size is thus increased, and horizontal resolution is decreased. None of these errors are correctable. There are, however, certain wave-induced biases which may be corrected for, and these will be investigated in subsequent sections.

The remaining errors which affect the actual altimeter measurement are environmental in nature and are often termed the delay corrections. This is so because

these phenomena slow the radar pulses as they travel to and from the sea surface, delaying the travel time and thus depressing the calculated topography.* These effects are due to the gases in the atmosphere (including water vapor), and free electrons in the ionosphere. While they are described in more detail later in the chapter, the point to note here is that they may have to be corrected for in order to determine the real sea surface topography. The word "may" is a key one, because in a number of circumstances, such correction is unnecessary or even impossible. Chapter 2 is largely devoted to investigating these circumstances and to determining whether or not the various error corrections should be applied to the GEOSAT sea surface height data.

The second category of altimeter errors consists of those phenomena which influence how one interprets the altimeter-derived sea surface topography. These phenomena are the tides - both solid and ocean. The solid tide essentially biases the surface topography up or down on long wavelength scales as the earth adjusts its shape to the tidal potentials induced primarily by the sun and moon. The ocean tide involves similar height biases, as well as tidal currents and long waves. The height biases are essentially the result of the ocean's attempt to follow the changes in the earth's geoid height induced by the apparent motion of the sun and moon. The additional dynamic nature of the ocean tide makes this a more complicated phenomenon than the solid tide, however (see Section 1.4).

Often, oceanographers treat tidal effects as noise when studying oceanic flow; modelled tides are removed from the sea surface topography. But, altimeters are also important tools in improving the tidal models themselves - as evidenced by Cartwright and Alcock (1981), who used SEASAT data to map the M2 tide in the north Atlantic; Brown and Hutchinson (1981), who mapped the M2 tide in the northeast Pacific, and Mazzega

* The delay corrections slow the pulses relative to a vacuum. In practice, the mean value of a delay phenomenon along a satellite track causes the apparent sea surface to be biased downwards all along the track. As the phenomenon fluctuates along track about its mean value, so too will the calculated sea surface. Thus the sign of a delay correction is always the same, but the apparent effect on the observed sea surface can be positive or negative.

(1983), who determined tides in the Indian Ocean from altimeter data. This thesis seeks, among other things, to determine the effectiveness of modelled ocean and solid tide corrections in removing unwanted features from the surface topography, for purposes of studying the circulation. In this regard, the earth's geoid is considered invariant over all GEOSAT repeats, as its tide-induced fluctuations are assumed to be separable (and removable).

An additional source of altimeter system error, though not germane to this work, nevertheless bears mention. This involves the coordinate systems used in satellite altimetry. There are a number of such systems (see Mueller [1981]), including the satellite tracking coordinates, earth shape and geoid coordinates, and inertial reference coordinates, among others. These systems do not coincide and thus lead to errors when attempting to define an "absolute" sea surface height. This is not a problem to lowest order, however, when one seeks the variability of the sea surface, as variability is relative in nature and not dependent on the coordinate system in use. Since this thesis will be concentrating on the latter approach, further discussion of coordinate systems is unnecessary.

Satellite Altimeter Systems

Prior to GEOSAT, three other satellite altimeters were flown: on SKYLAB (1973) GEOS-3 (1975), and SEASAT (1978). The SKYLAB altimeter was essentially a proof of concept mission, and with a range resolution of only about 1 m it produced few oceanographic results.

GEOS-3 was the first dedicated altimetric mission, and its altimeter operated at 13.9 GHz with an 80 MHz bandwidth. Pulse compression was a factor of 30, and pulsewidth was 12.5 ns (or 3.8 m). The rated range resolution (consisting of all errors except orbital) was 0.5 m after 0.2 s of data averaging. Significant wave height, calculated from the slope of the leading edge of the waveform, was rated at $\pm 25\%$ of the actual SWH, for SWH values from 4-10 m (altimeter specifications from Stewart [1985]).

GEOS-3 spawned a number of oceanographic and geophysical advances, as well as various algorithms and data handling techniques whose refined versions are still in use. Huang et al. (1978), for example, studied the temporal and spatial changes of the Gulf Stream front and its associated eddies by using the crossover method on GEOS-3 data (this method is discussed in Section 1.2). Mather et al. (1980) investigated variable features south of the Gulf Stream via the collinear method discussed in Douglas and Gaborski (1979), and expressed confidence in locating eddies larger than 50 cm in magnitude at scales of 30-100 km with the GEOS-3 data. Marsh et al. (1980) computed the mean sea surface in a variety of locales using GEOS-3 outputs, while Diamante and Nee (1981) determined tidal constituents from GEOS-3 derived sea surfaces. Cheney and Marsh (1981b) mapped mesoscale variability measured by GEOS-3, and others used the data to improve geoid models (e.g., Rapp [1979], Lerch et al. [1979]).

GEOS-3 was followed by SEASAT; which, along with four other microwave sensors, flew an improved altimeter similar to GEOSAT's. The SEASAT altimeter operated at 13.5 GHz with a 320 MHz bandwidth and pulse compression factor of 1000. Pulsewidth was 3.6 ns (1.1 m); shorter than that of GEOS-3 and thus allowing more accurate SWH determination. The latter output was rated at ± 5 m or 10% of the actual SWH (whichever was greater), for SWH values from 1-20 m. Range resolution was comparable to the current generation GEOSAT, being 0.1 m after 1 s of data averaging (Stewart, 1985).

SEASAT was launched on 28 June 1978 and failed due to a massive short circuit on 10 October 1978. Additional down time in the altimeter further reduced the amount of sea surface height measurements - the final data set consisted only of some 70 days of altimeter readings. Nevertheless, SEASAT continued to advance the field of satellite altimetry and increase knowledge of the oceans. Two excellent sources on the evaluation and results of SEASAT are the SEASAT Special Issues I and II reprinted from the *Journal of Geophysical Research* in 1982 and 1983 (Vols. 87 [C5] and 88 [C3], respectively).

Some notable results from the SEASAT altimeter include the following: Cheney and Marsh (1981) observed the Gulf Stream position and movement of a cyclonic ring, and Cheney et al. (1983) mapped global mesoscale variability from collinear tracks of SEASAT data. Wavenumber spectra of the oceanic mesoscale were computed by Fu (1983), while Marsh and Martin (1982) produced global contour maps of the mean sea surface topography. Tai and Wunsch (1983) mapped the subtropical gyre in the north Pacific; the first direct measurement of such a feature not dependent on conventional hydrography. Fu and Chelton (1984) used SEASAT data to provide the first direct evidence for zonal coherence in the temporal variability of the Antarctic Circumpolar Current, and Douglas et al. (1984) observed global oceanic circulation with the SEASAT data set. Geoid model improvement continued with work such as Rapp (1983).

Eight years elapsed from the untimely demise of SEASAT to the launch of GEOSAT, which is described in the next subsection. Future plans for satellite altimeters include the European Space Agency's ERS-1 in late 1990, and the joint French-American mission of TOPEX/POSEIDON in mid 1991.

GEOSAT

On 30 September 1986, the U.S. Navy altimetric satellite GEOSAT completed its classified primary mission of marine geoid mapping, after some 18 months of operation. On 1 October, a series of maneuvers was initiated to alter the geodetic orbit to produce groundtracks within a few km of the previously released SEASAT tracks, allowing the data to be unclassified. The new orbit was designed to repeat within a 1 km band after 244 revolutions (17.05 days), and yields an equatorial groundtrack spacing of 164 km. This configuration, termed the Exact Repeat Mission (ERM), became operational on 8 November 1986, and was optimized for the study of oceanic variability (Cheney et al., 1987).

GEOSAT carries an improved SEASAT class altimeter operating at 13.5 GHz with a 320 MHz bandwidth. Pulse compression is over 32,000 and the (compressed)

pulsewidth is 3.125 ns - somewhat shorter than for SEASAT. The specified measurement precisions are: Sea surface heights to 3.5 cm (RMS) for 2 m SWH and less, after 1 s of data averaging; and significant wave height to 10% of the actual SWH or 0.5 m, whichever is greater (specifications from MacArthur et al. [1987]).

It is important to note the distinction between measurement precision and range resolution. The former is inherent to the altimeter itself and may be thought of as the ability of the altimeter to repeat the distance measurement to a surface, all other factors constant. As an example, the 3.5 cm precision figure indicates that a motionless GEOSAT taking repeated measurements to an unchanging sea surface would still have a 3.5 cm RMS variability in those measurements, just due to the altimeter noise level. Range resolution, on the other hand, includes all of the altimeter errors mentioned earlier (except the orbit error), and reflects the accuracy with which the altimeter makes a "real world" determination of the distance to the sea surface, after corrections for the errors are implemented. GEOSAT's rated range resolution is similar to SEASAT's - about 0.1 m (refer to Summary Section at the end of this chapter).

This thesis focuses on the evaluation and use of the GEOSAT data with regards to the study of mesoscale variability in the ocean. This is an important work for a number of reasons. First, the GEOSAT data set is a relatively new and untried product. As with any such product, initial care must be taken to ensure that the data appears reasonable to the knowledgeable eye. This is the purpose of Section 1.4. The second contribution of this thesis is an analysis of the corrections provided with the GEOSAT sea surface height data, which purport to reduce the aforementioned altimeter errors. Many of these corrections are new; and some, like the wet troposphere models, are actually a step back from SEASAT (which could compute its own correction on board). Rather than indiscriminately applying the corrections and focusing on some area of the ocean with obvious mesoscale features, this thesis takes a subtler approach. To this end, Chapter 2 uses the GEOSAT data in an essentially quiet part of the ocean (the northeastern Pacific), where any oceanographic

signals may be easily obscured by altimeter errors. Spectral and statistical methods are employed to observe the actual effects the corrections have on the sea surface heights. Do the corrections make it easier or harder to spot the oceanography, or do they make little difference at all? If one of the latter two turn out to be the case, then the correction should not be made. Chapter 2 in a sense passes judgement on the GEOSAT corrections and also explores the possibility of averaging successive sea surface heights together to decrease noise and computer storage space.

The final chapter in the thesis uses GEOSAT data edited according to Chapter 2, to investigate oceanic variability in the northeastern Pacific. GEOSAT-derived results are compared with independent studies and new insights into the oceanography of the region are explored. Suggestions for further work are also presented.

1.2 OCEANOGRAPHY FROM ALTIMETRY

Prior to discussing the specifics of GEOSAT, it is both useful and motivational to examine what sorts of oceanographic knowledge may be gained from satellite altimeter data and why that data is often preferable to more conventional measurements. Basically, an altimeter is a useful oceanographic tool because of the high spatial and temporal density of its measurements. This density allows for synoptic scale coverage of the oceans while avoiding the expense, difficulty, and limited scope of traditional shipboard measurements.

Given synoptic scale sea surface height measurements, what may be learned about the oceans? Perhaps the most fundamental product is the determination of the surface geostrophic currents. Additional knowledge of the three-dimensional density distribution in the ocean allows the geostrophic currents to be fixed at all depths (Wunsch and Gaposchkin, 1980). Knowing where the water goes is absolutely central to physical oceanography, as this knowledge enables quantities such as mass, heat, and chemical transports to be calculated. These in turn are crucial variables in such diverse fields as climatology, marine biology and pollution control.

To a good approximation, surface currents are in geostrophic equilibrium and hydrostatic balance (Wunsch and Gaposchkin, 1980). The former states that the pressure-induced force caused by a sloping sea surface is largely balanced by the Coriolis force acting on the moving water parcel. Thus water tends to flow clockwise around oceanic "hills", instead of down them. Pure geostrophy allows no evolution of the flow with time, however (see eq. 3), and the actual flow is really only quasigeostrophic. In non-dimensional terms, the deviation of the ocean currents from geostrophy is of the order of the Rossby number, defined by $R_0 = U/fL$, where U is a characteristic velocity, L is a characteristic length scale, and $f = 2\Omega\sin(\text{latitude})$ is the Coriolis parameter (Ω being the rotation rate of the earth). Over most of the oceans the Rossby number is very small (typically $\leq 10^{-2}$), indicating that the geostrophic approximation is a good one. However, geostrophy breaks down at the oceanic boundaries, the equator (where f approaches zero), and in the cross-stream velocity components of major currents such as the Gulf Stream (Wunsch and Gaposchkin [1980], Stommel [1965]). In these regions, one may still calculate the surface velocity fields from the sea surface slopes, but more complex relationships than the geostrophic one (soon to be presented) must be used.

The approximation of hydrostatic balance simply states that pressure changes in the water column are due to the weight of the water above and are independent of water motion. In a local Cartesian coordinate system with x horizontal and z upward, the hydrostatic balance implies

$$g = - \frac{1}{\rho} \frac{\partial p}{\partial z} \quad (1)$$

where g is the local vertical component of gravity, ρ is the water density, and p is the pressure. The aforementioned geostrophic balance says that

$$fv = \frac{-1}{\rho} \frac{\partial p}{\partial x} \quad (2)$$

where f is again the Coriolis parameter and v is the velocity normal to the x, z plane. The connection between the oceanic density structure and the geostrophic currents is found by eliminating pressure between (1) and (2), and integrating vertically from some reference level z_r , to obtain

$$v = \frac{g}{\rho f} \int_{z_r}^z \frac{\partial \rho}{\partial x} dz + v_r \quad (3)$$

where v_r is the velocity at the arbitrary reference level and v is the velocity at z . Thus, if the density structure between two levels is known (from hydrography, for example), the integral may be evaluated, determining the relative velocity between them. The desired result is the calculation of absolute velocities, however, and for that, the reference level velocity v_r must be fixed. Traditionally, two approaches have been used. The first has been to go out and measure the current at some level, which is expensive, time-consuming, and inherently limited in scope. The second was to assume that little was going on in the deep oceans, and so choose some deep z_r and assign it a reference velocity of zero. Recent work indicates that this is not an accurate assumption (Wunsch and Gaposchkin, 1980), which is where the real usefulness of altimetry becomes apparent.

Altimeters allow the geostrophic velocity at the surface to be fixed, because that velocity is related to the surface topography through the hydrostatic and geostrophic equations by

$$v_s = \frac{g}{f} \frac{\partial \eta}{\partial x} \quad (4)$$

where v_s is the surface geostrophic velocity and η is the displacement of the sea surface from the geoid, which may be obtained from an altimeter. Thus, (3) and (4) allow for the calculation of the geostrophic velocity at any depth from

$$v = \frac{g}{\rho f} \int \frac{\partial \rho}{\partial x} dz + v_s \quad (5)$$

Even with highly accurate altimetry, the practical application of (5) has its limitations. First, only the geostrophic component of the total velocity may be determined from the sea surface slope. Near the surface, other components such as the wind-driven Ekman flow may be of much larger magnitude than the geostrophic current.* Second, lack of knowledge of the oceanic density field limits the usefulness of altimeter data alone in defining the oceanic circulation. Acoustic tomography may eventually replace conventional hydrography and ease this restriction, but that time still lies in the future. An additional method of some promise is the technique of assimilating altimeter-derived sea surface heights into global and regional circulation models. Here, the in situ density field can be solved for from the surface boundary conditions as the model propagates the surface velocities downward through the water column (e.g., Hurlburt [1986]). Such models are *currently far from perfect*, however, and it may be a number of years before they may be confidently used with only sea surface heights for boundary conditions.

The third practical limitation on the use of (5) is the lack of sufficiently accurate geoids. The sea surface must be referenced to the local geoid to determine its true slope and hence the surface geostrophic current. The use of mean altimeter-derived sea surfaces to approximate the geoid is prohibited because they already contain the effects of the mean circulation (See Section 2.1). Thus independent gravity-derived geoids are required, which are costly and have been determined only in a few areas. The Marsh and Chang (1978) gravimetric geoid for the Northwest Atlantic is a noteworthy example, which has been used in several altimetric studies to draw inferences about circulation in the Gulf Stream region.

There are ways to gain valuable information about the oceans while circumventing the need for an accurate geoid, however. These involve looking at the variability of the sea

* Knowledge of the geostrophic velocity is still in itself a very useful thing, as this component of the total velocity is important throughout the water column.

surface height with time, which allows for the computation of the variable geostrophic currents. Essentially, these techniques use the altimeter data to create a mean sea surface over all the satellite repeat cycles. They then calculate the difference between the surface topography during any one repeat and the mean surface topography. Since the geoid (and the mean circulation) are expressed by non-varying surface topography, the differencing procedure causes them to fall out of the problem and highlights the variable features. This technique forms the basis of the so-called crossover and collinear methods of satellite altimetry, which have the additional advantage of reducing orbital and other long wavelength errors.

The crossover technique uses sea-surface height data obtained at points where the ascending and descending ground tracks cross each other. Excluding the small contribution of the variable surface topography, these separate heights should agree with each other. They rarely do, however, mainly because of the different orbit error between the two tracks. As mentioned before, this orbit error is of very long wavelength, and so over arc segments it may be approximated by a linear (or quadratic) polynomial (see Tai and Fu [1986]). The crossover technique seeks to minimize the crossover differences in a least squares sense by adjusting the sea surface heights along the tracks with the desired polynomial. The result is a separate sea surface height map for each satellite repeat cycle (approximately every 17 days for GEOSAT). These maps may then be used to form the mean and differenced surfaces described above. Examples of the use of the crossover technique may be found in Huang et al. (1978), Cheney and Marsh (1981b), and Tai and Wunsch (1983), among others. An additional advantage of the crossover technique is that determining the satellite orbit at various times with precision tracking or ephemerides of high accuracy can essentially fix the crossover mesh with respect to the earth and allow for absolute sea surface height mapping. This was performed on GEOS-3 data by Marsh et al. (1980), and on SEASAT data by Marsh and Martin (1982), for example. A recent variation of the crossover technique is to represent the orbital error by a Fourier series

whose coefficients are then adjusted to minimize the crossover differences (Douglas et al., 1984).

The crossover technique is not without its drawbacks, and three of these in particular prevented its use in this work. First, it is time and storage intensive on a computer, and difficult to master in a limited period of time. Second, effective error estimates are difficult to define as errors of all wavelengths (from altimeter noise to orbit error) contribute to the calculated RMS crossover differences. Most importantly, though, the large gaps between the crossover points (see figure 1.3) preclude use of the short spatial scales in investigating the effectiveness of the altimeter corrections or the smaller mesoscale features. Since these pursuits are central to this work, the collinear approach was adopted instead. This technique is presented more fully in Chapter 2, but a few points are salient at this time.

Sea surface variability can be obtained from the collinear method when the satellite groundtracks repeat after some interval. A mean sea surface height profile for a segment of a selected groundtrack is calculated by averaging together the profiles of individual passes along it. Then, the difference between any given repeat and the mean may be determined, again taking the geoid out of the problem and highlighting variable features. Orbit error is reduced as in the crossover method by removing a low order polynomial from each sea surface height profile. The length of the groundtracks used in this work (some 4400 km) allows a simple bias and tilt removal to suffice. Note that this linear trend removal will also reduce long wavelength errors in any applied corrections, as well as eliminate the need to correct for any long wavelength processes in the first place. Bias and tilt removal also eliminates any oceanographic signals of wavelengths comparable to the groundtrack length, but this loss is acceptable if mesoscale effects are the focus; as they are in the present case. Examples of the collinear technique may be seen in the work of Douglas and Gaborski (1979), Mather et al. (1980), Cheney et al. (1983), and Fu (1983).

1.3 GEOGRAPHY AND TERMINOLOGY

The area under investigation in this work is a rectangular portion of the northeastern Pacific, bounded by 20°N , 55°N , 180°W and 115°W (see figure 1.2). It is primarily deep ocean, though it also contains the western coast of the United States, the Hawaiian islands, and portions of the Aleutian island chain. This region was chosen because it is fairly well known in an oceanographic sense and independent sources exist which may be used for data comparison. In addition, much of it is relatively quiet in mesoscale variability, and so this area may also be used to find a lower noise threshold on GEOSAT-derived sea surfaces, and more rigorously determine the effects of corrections.

The geometry of the area, along with GEOSAT's orbit, gives rise to a pattern of satellite sub-tracks which may be described as follows (this terminology will be adhered to throughout this work): In a given 24-hr period, GEOSAT overflies the area about 6 times; each overflight is called a pass. The six overflights appear in 2 clusters of 3 passes each. One cluster contains all ascending passes, and the other, only descending. Clusters are separated by from about four and a half to seven and a half hours when no passes are made over the area. Passes within a cluster are separated in their starting times by about 101 minutes, and in perpendicular distance by about 2200 km. Figure 1.2 shows the area and satellite sub-tracks for day one of the ERM.

During any 17-day period, each pass will be along a distinct arc within the area, and the set of passes during a 17-day repeat cycle will fill out a skewed checkerboard pattern (see figure 1.3). After 17 days however, the passes start to repeat themselves, tracing over the same arcs as before. Thus, each arc is a great circle passing through the area, and may be considered as an ensemble of those passes separated by 17 days which are traced along it. The spatial and temporal sampling which result from this scheme are fairly close to the 20-day repeat and 140 km equatorial groundtrack spacing suggested by Mitchell (1983) as being nearly optimal for adequately resolving the oceanic mesoscale (which has typical spatial scales of 100 km and time scales of 30+ days).

Note from figure 1.3 the significant amount of missing data in the area. These data dropouts occur mainly on descending passes and result from the satellite's waveform tracker being unable to lock onto the return pulses after passing over land. Extensive dropouts present obvious problems for the collinear technique, and repeat passes which contain them are largely avoided in this work.

1.4 THE GEOPHYSICAL DATA RECORD

The GEOSAT Geophysical Data Record (GDR) is prepared from Sensor Data Records and provides the user with 34 channels of data approximately every second. These 1/sec values include time, latitude and longitude of the satellite subpoint, orbit height, sea surface height, geoid height, several diagnostics, and corrections which were already applied to the sea surface heights. In addition, corrections for the errors mentioned in the preceding sections are given, which may be applied as the user sees fit. The Sensor Data Records (SDR's) are described in detail in the GEOSAT Interface Control Document (Cole, 1985). The main reference on the GDR is the GDR User Handbook (Cheney et al., 1987).

The following subsections describe the initial forays into the GDR. Quite simply, these were attempts to see if what was actually on tape made sense compared to observational and/or theoretical knowledge of what was supposed to be there. Accordingly, discussions of applicable physical processes are presented, with descriptions of their corresponding GDR channels. In addition, the literature search necessitated by the above revealed numerous (and sometimes conflicting) error estimates for the various GEOSAT measurements and corrections. I attempt to reconcile these estimates and provide as meaningful an error budget as is currently achievable.

The "zero-order" look at the GDR data was at a long arc passing completely through the area and comprised of six gap-free passes. For identification purposes, it was arc 82; a descending track with approximate limits of 55°N, 138°W and 20°N, 161°W

(identified on figure 1.3). During the first few repeat cycles, this arc consisted of passes on days 3, 21, 38, 55, 72 and 88 of the ERM.

Time

GEOSAT's raw measurements are recorded on board the satellite with the spacecraft clock count, and then dumped about twice a day when the satellite is in view of the Ground Station. The station keeps its own time as well, which is used to calibrate the spacecraft clock during periodic real-time downlinks. The calibration is used to generate a corrected "time tag" for each processed altimetry data frame (see Jones et al. [1987] and Cole [1985] for further discussion). The accuracy of the final time tagging of the data is rated at $<100 \mu\text{sec}$ (Jones et al., 1987), and studies by Cheney et al. (1987b) of crossover differences have revealed no time tag biases thus far. As will be seen shortly, GEOSAT's time accuracy is not a limiting factor in its error budget.

The GDR has two 4 byte (integer) channels devoted to time. They indicate seconds and microseconds of UTC (Universal Time Coordinated, or *Greenwich Mean Time*) referenced to 1 January 1985. A printout of these channels shows that successive points on a pass are separated by the correct time of about 98 seconds, and the repeat passes on the arc are separated by the published value of 17.05 days (cited times are from Cheney et al., 1987).

Latitude and Longitude

The GDR has two 4 byte (integer) channels for location information - one each for latitude and longitude of the satellite subpoint, in microdegrees. Printouts show that successive subpoints on a pass are separated by approximately 6.7 km, which is appropriate for the groundspeed of a satellite with a nodal period of 6037.55 sec (Born et al., 1987). They also indicate that the groundtracks of the repeats on arc 82 are separated by a crosstrack distance of less than 1 km, as desired. The subpoints are a product of the ephemeris calculated by the Navy Astronautics Group (NAG), and their horizontal accuracy is about 3 to 5 times the radial orbit accuracy (Born, 1988); or about 15 m (RMS).

Horizontal positioning uncertainties of this size should not significantly affect the accuracy of the measured sea surface topography, for two reasons. First, the deep ocean surface height simply doesn't change by much on that horizontal scale, assuming waves are averaged out (which they are for GEOSAT). Second, GEOSAT's radar footprint is itself of order 4 to 5 km, depending on significant wave height (Shuhy et al., 1987), so errors of a few meters in its horizontal position are negligible.

Orbit

GEOSAT is currently in a 17 day exact repeat and frozen orbit. Exact repeat refers to the fact that groundtracks should repeat to within ± 1 km for each repeat cycle. Frozen means that the mean argument of the perigee (\bar{w}) and the mean eccentricity (\bar{e}) have no long term variation, being chosen such that perturbing forces in the earth's gravity field will cancel each other out (see Born et al. [1987]). In the hypothetical case of no other orbit perturbations, a frozen orbit will result in a near invariant satellite altitude profile from repeat to repeat on any arc (in actuality, even in a frozen orbit, \bar{w} and \bar{e} will vary cyclically). The mean argument of the perigee and mean eccentricity for GEOSAT are 90° and .0008 respectively (orbit parameters from Born et al. [1987]). The perigee argument places apogee for GEOSAT over the equator and perigee nearest the poles. The low eccentricity indicates that GEOSAT is in a near circular orbit, which is desirable to keep small the radial component of the satellite's velocity (less than about 50 m/s in GEOSAT's case [Cheney et al., 1987b]). Small radial speeds are necessary to maintain the rate of satellite-sea surface distance variation within the limits of the altimeter tracking circuitry, and to minimize altimeter measurement error due to timing inaccuracies. At the cited radial speeds, GEOSAT's timing uncertainty of 100 μ sec gives rise to only a .5 cm error in the sea surface heights, which is negligible compared to the other uncertainties, as will be seen shortly. Two final orbital parameters of interest are GEOSAT's mean semimajor axis \bar{a} , and its mean inclination \bar{i} . These are 7167.4 km, giving an actual altitude of about 800 km; and about 108° , putting GEOSAT in a retrograde orbit. Chapter 15 of Stewart (1985)

contains an excellent description of orbital terminology, and is recommended for further reading.

Any satellite's orbit is perturbed by gravitational forces from such sources as the earth's geopotential, the sun and moon, solid and earth tides, as well as by nongravitational forces. The latter include atmospheric drag and the radiation pressure due to the solar flux (see Parke et al. [1987]). Incomplete knowledge of these forces naturally affect the accuracy of the orbit calculation. GEOSAT's ephemeris is computed from doppler tracking data in conjunction with a calculated trajectory using the NASA GEM (Goddard Earth Model) 10B geopotential model (Lerch et al., 1981). This model does not include gravitational effects other than the earth's fixed geopotential, or any non-gravitational effects. Cheney et al. (1987) cite the overall radial accuracy of the ephemeris as approximately 4 meters (RMS), which will directly propagate into uncertainty in the sea surface heights.* Fortunately, as mentioned earlier, most of the orbit error may be removed by simple detrending of the sea surface heights on each pass.

Each orbital value on the GDR is a 4 byte integer and gives the satellite height in mm above the earth's reference ellipsoid defined by $a = 6378.137$ km and $f = 1/298.257223563$. Printouts show the orbit height close to the known range near 800 km and the difference between repeat passes on arc 82 to be on the order of hundreds of meters.

Sea Surface Height

The following discussion is based upon MacArthur et al. (1987), and Cole (1985). Repeated citation is avoided in the interest of readability.

The GDR sea surface height channel (H) is a 2 byte integer (as are all the subsequent channels discussed in the GDR section), and is the one-second average sea surface height in cm above the reference ellipsoid. H is computed at the GDR rate of

* Recent work puts the uncertainty at about 3 m RMS (Born, 1988).

~1/second from a linear fit with iterative outlier rejection of the 10 surrounding height values H1 through H10 which are at the full GEOSAT data rate of 10/sec (Cheney et al., 1987). Each full-rate height is calculated by $H(n) = \text{ORBIT}/10 - \text{ALTIMETER}$, where ALTIMETER is the measured height in cm between the satellite and the sea surface and ORBIT is the satellite height in mm above the reference ellipsoid. The height is determined by the travel time taken from pulse transmission to the half power point on the leading edge of the averaged return waveform.

Prior to the computation of $H(n)$, the altimeter measurement is corrected for a number of effects. The GEOSAT waveform processing module takes 8 return waveform samples at the full rate and averages them every second. Corrections are made to the waveforms based on prior calibration, and the corrected waveforms are used to produce a voltage term proportional to satellite attitude (VATT) at the 1/second rate. VATT also depends on significant wave height (SWH), however, and its accuracy is degraded at high values of SWH. The VATT values are corrected for SWH based on adjustable coefficients initially determined by prelaunch tests.

The corrected 1/second VATT values are edited to delete outliers, as well as any values lying outside the range corresponding to the expected off-nadir excursions of GEOSAT. The remaining values are sent to a first order fit routine that assigns a VATT value at the 1/second GDR rate, which is the average of the edited VATT values in a window of up to ± 2 minutes. The window span is determined by SWH, as the increased noise at high SWH requires a longer averaging period. The fitted VATT values, in conjunction with the SWH, are used to compute a 1/second height correction to the ALTIMETER measurement. In essence, this height correction compensates for the apparent depression of the sea surface caused by an off-nadir radar beam. Cole (1985) lists the correction uncertainty as ± 2 cm. It appears in the GDR channel labelled DH (for "Delta H") and has already been applied to the sea surface heights.

Another 1/second correction applied to the ALTIMETER measurement is due to the range/doppler crosstalk of linear FM (Frequency Modulated) waveforms like those of the GEOSAT radar. In essence, the doppler shift caused by a vertically travelling GEOSAT is seen as a height bias in the ALTIMETER measurement (This is another reason why the orbital eccentricity was kept small). Cole (1985) writes that it is only necessary to know the vertical speed to a precision of 1 m/s to determine the FM correction to better than .5 cm. This precision is easily achieved by averaging ten of the raw satellite altitude measurements before determining the vertical speed. The FM crosstalk correction is given in the GDR as FM/DH, and like DH, has already been applied to sea surface heights in the GDR.

Three other corrections are made to the sea surface heights before being placed in the GDR. The first accounts for the location and movement of the spacecraft center of gravity with respect to the altimeter and was determined prior to launch (this corrects for the ORBIT values being computed to GEOSAT's center of gravity while altimeter measurements are actually made from the radar antenna). The second is a bias periodically computed from the on-board calibrate mode of the satellite, and the third corrects for inherent system effects such as antenna focal length and internal signal delays.

The reader will note that all corrections are at the GDR rate of 1/second, while the $H(n)$ which are averaged to calculate H occur at a rate of 10/sec. This is not a discrepancy. The ten $H(n)$ each have the same correction applied, which is the one appropriate to their central time value (Cole, 1985).

The GEOSAT altimeter is designed to measure the satellite-sea surface distance with a precision of 3.5 cm for 2 m significant wave height (MacArthur et al., 1987). Ground tests have verified that the altimeter noise level is near 2 cm at low SWH after 1 second averaging. In flight, the performance was evaluated by computing the standard deviation about a linear fit to a set of 10 heights at the full 10/sec rate, repeating this for 10 consecutive sets, and averaging the resultant standard deviations. MacArthur et al. (1987)

found the agreement between the ground test data and this in-flight evaluation to be quite good and so assigned an in-orbit RMS precision of 3.5 cm for 2 m SWH to H values averaged over 1 second (as on the GDR). Being an in-orbit test, the 3.5 cm figure should include the aforementioned corrections of attitude, crosstalk, etc. One must remember, though, that the in-orbit evaluation used standard deviations calculated from short spans of time (~10 sec for the final averages), over which effects such as attitude excursions and bias drift would be small. For the longer times appropriate to the arcs under study in this work, the system noise level might therefore be greater.

As previously mentioned the GDR H channel is determined not only from the ALTIMETER measurement, with its nominal 3.5 cm precision, but also from the ORBIT calculation, with its 3 m accuracy (RMS). In this regard, the GDR looks good to zero order. At a given time on a pass, the H1 through H10 values (whose relative magnitudes over their span of 1 second are negligibly affected by the long wavelength orbit error), fluctuate on the order of a couple cm, which is appropriate to the altimeter precision. (The actual standard deviation for each set of H1-H10 values is included as a separate GDR channel denoted as SIG H, for "sigma H". Printouts show that this too is in the few cm range for the passes on arc 82). The H values at a given geographic location on the arc differ by up to ~300 cm between passes, which is primarily a reflection of the orbit error. Figure 1.4 is a plot of the values of H along arc 82 during the fourth repeat cycle. By comparison with figure 1.5, note how, to first order, the sea surface merely follows the geoid, which is now discussed.

Geoid

The GDR Geoid channel contains geoid height in cm above the reference ellipsoid, computed with bilinear interpolation of 1 degree geoid height estimates computed from Rapp (1978). The Rapp geoid was originally determined to degree and order 12, which represents features in the geoid down to a wavelength of $2\pi R/12 \approx 3300$ km (where R is the radius of the earth). While this resolution is far too coarse for oceanographic

applications, the Rapp geoid is nevertheless included in the GDR as a way of reducing the variability of the sea surface heights. Since the sea surface topography follows the geoid to lowest order; subtracting out the geoid reduces the sea surface height variation from the ± 100 m range to the ± 5 m range. This makes data plotting and visual inspection much easier and is used in this work.

GDR printouts look good with respect to the known characteristics of the Rapp geoid. Geoid heights on successive passes for the same geographic area differ by a few cm, which is appropriate, since cross and alongtrack track distances can differ by a few kilometers for the different repeats. A plot of the geoid channel along the fourth repeat on arc 82 (see figure 1.5), agrees quite well with the sea surface height profile of the same repeat (figure 1.4); though one can clearly see that the geoid model does not fully resolve Hawaii at $\sim 22^\circ\text{N}$. Orbit error is also evident in the offset between the profiles. Figure 1.6 is a plot of figure 1.4 minus figure 1.5, or H minus geoid for repeat 4 on arc 82, and indicates the efficacy of a geoid correction in reducing variability. The major features of this profile are due to uncertainty in the modelled geoid.

Significant Wave Height

The GDR Significant Wave Height (SWH) channel is listed once per second, and similar to the H channel, is the one second average of the surrounding full-rate SWH data. The averaging process is identical with that used for H; a linear least squares fit with iterative outlier rejection (the maximum number of rejections allowed for both SWH and H is four. After that, flag values of 32767 cm are set in the GDR). The 10/second SWH are determined onboard GEOSAT by measuring the leading edge slope of the reflected pulse. Since this measurement varies with attitude and is also a function of SWH itself, a correction is made for these effects, as well as a small calibration adjustment (Cole, 1985).

The design precision of the GEOSAT SWH after averaging is 10% of SWH or 0.5 meters (whichever is greater). Based on comparisons with buoy data it appears that this goal has been met (Dobson et al., 1987). As noted in the sea surface height section, SWH

is a necessary input in calculating the attitude/SWH correction to H . Since the verification of the H precision was performed inflight with these corrections applied, though, SWH uncertainties in this regard should be included in the 3.5 cm precision value.

Significant wave height is also a measure of other effects that have an impact on the sea surface height measurement. These effects have, singly or in concert, been termed electromagnetic (EM) bias. Wave peaks tend to disperse radar energy, while troughs tend to focus it in the direction of the spacecraft. Thus the satellite receives more return energy from the troughs than the peaks and so sees the sea surface as depressed from the actual mean level (Tapley et al., 1982). An additional factor is the wave skewness, or asymmetry (i.e. narrow high peaks and broad shallow troughs) that tends to further bias the altimetry measurement towards the troughs. Lipa and Barrick (1981), extending the theory of Jackson (1979) determined that the EM bias correction at the SEASAT altimeter frequency, which is the same as GEOSAT's, should be about 2% of the SWH. This was supported by SEASAT data as calculated by Born et al. (1982). For these reasons, the present recommendation for GEOSAT is that the sea surface heights should be increased by 2% of the significant wave height (Cheney et al., 1987). A recent GEOSAT error budget (Lybanon and Crout, 1987) ascribes an RMS uncertainty of 2.2 cm to this correction, assuming a SWH of 2 m and a wave skewness of 0.1. The relatively short wavelength (200-1000 km) that they ascribe to this error indicates that bias and tilt removal would not reduce it by much when the correction is applied to sea surface heights in the area.

Printouts of the GDR SWH channel for early repeats along arc 82 show quite a bit of variability, both along and between passes. Differences between the repeats are on the order of 7 meters for the northern part of the arc; and there are a respectable number of SWH values of greater than 2 meters (meteorological causes of SWH behavior are examined in a later section). This variability would equate to EM bias correction variability on the order of 10+ cm, but more importantly perhaps, some questions must be raised as to the applicability of a 3.5 cm instrument precision in regions of high SWH. This, too, will

be addressed later. Figure 1.7 shows a plot of SWH along arc 82 during the fourth repeat cycle.

Solid Tide

The GDR solid tide (STIDE)* correction, like the remaining correction channels, is given in mm and is to be subtracted from the H values as the user sees fit. This correction is based on the solid earth response to the tide generating potentials of Cartwright and Taylor (1971) with subsequent modification by Cartwright and Edden (1973). The solid tide height is extrapolated at the GDR 1/second interval from calculations of the tide generating potential and gradient at 30 second intervals along the ground track (Cheney et al., 1987).

The amplitude of this phenomena is about 20 cm (Tapley et al., 1982), with printout values on arc 82 varying smoothly within this range. Of more interest, however, is the low error of this correction, given by Cheney et al. (1987) as 1 cm (RMS). Additionally, as can be seen by its plot for the fourth repeat on arc 82 (figure 1.8), the Solid Tide correction is of very long wavelength, and so any errors in it should be further reduced via bias and tilt removal, as was discussed earlier.

Ocean Tide

This channel gives the surface ocean tide (OTIDE) correction to H and is based on the work of Schwiderski (1980). The correction is interpolated along the ground track at the GDR 1/second interval from a 1 degree global grid of 11 tidal components. The ocean tide reaches amplitudes over 100 cm in the open ocean and 200 cm in coastal areas (Schwiderski, 1980). Printouts of the GDR OTIDE channel show the data to be consistent with these bounds. Unfortunately, the accuracy of this correction is much worse than that of the solid tide correction. This is due not only to the larger amplitude of the ocean tide, but to the more complex nature of the oceanic response to tidal forcing. As opposed to the

* The various GDR corrections will often be referred to by acronym in this work. The appropriate acronyms are defined at the beginning of each correction's subsection.

solid tide, which is largely static, the ocean tide also includes dynamic response to tidal forcing, in the form of long waves which are affected by the Coriolis force and the inherent resonances of the ocean basins (see Hendershott [1981]). Uncertainties in modelling these waves leads to the rather large figure of 10 cm (RMS) error in an OTIDE correction to sea surface heights (Schwiderski, 1980).

Figure 1.9 profiles the OTIDE correction for repeat 4 on arc 82. It is apparent that this correction has a richer spectrum at short wavelengths than the STIDE correction, indicating that the error introduced by applying an OTIDE correction might not be significantly reduced by bias and tilt removal.

As will be seen later, the magnitude and variability of the ocean tide necessitates a correction be made to the sea surface heights before investigating mesoscale features. This result emphasizes the importance of testing the zero-order accuracy of the GDR product. While this check may be done by statistical or spectral methods (and will be in Chapter 2), a quick comparison with actual tidal station predictions is a useful exercise. To this end, three arcs were chosen that passed the closest to the tidal reference stations at Honolulu, San Diego, and Sweeper Cove, Alaska. For each arc, GDR OTIDE values for the closest point of approach to the tide station were obtained for 3 different repeat cycles. The GDR tidal values were then compared with tabulated predictions from the U.S. Dept. of Commerce Tide Tables for the stations at the appropriate times. The results may be seen in table 1.1 and indicate that the GDR channel is appropriate in sign and amplitude. Of note is the column entitled R, which is the ratio of the GDR tidal amplitude to the station amplitude. This turns out in nearly all cases to be <1.0 , which is proper, since the GDR data is for open ocean, whereas the station values are taken in more enclosed waters, where the tidal amplitude normally will be greater.

Wet Troposphere

The remaining three corrections account for the lengthening of the radar travel time caused by delay of the signal as it propagates through the troposphere and ionosphere.

Since any delay in travel time will depress the measured sea surface below its actual state, these corrections should wind up raising that surface. As previously mentioned, the GDR corrections are to be subtracted from the H channel, so their negative values as seen on arc 82 printouts do in fact increase the sea surface heights as desired.*

The wet troposphere correction channels compensate for the travel time delay caused by water vapor in the troposphere. One GDR channel is termed wet FNOC (WFNOC) and is computed as follows: Surface values of air temperature and water vapor pressure are interpolated along the satellite track from the Fleet Numerical Oceanographic Center (FNOC) model output, which appears in a 2.5 degree grid at 12 hr intervals. These values are then used to compute the wet troposphere correction based on the Saastamoinen (1972) model. The other channel is termed wet SMMR and is based on Prabhakara et al. (1985) and Tapley et al. (1982b). Values for the vertically integrated atmospheric water vapor are interpolated along the ground track at the GDR interval from a climatic monthly mean data set from the NIMBUS 7 SMMR prepared by C. Prabhakara. This data appears in a 3° latitude by 5° longitude grid of monthly averages between 1979-1981 (Cheney et al., 1987). The water vapor values are then converted to a height correction using a simple formula due to Tapley et al. (1982b). It may be noted that these modelled corrections are necessary because GEOSAT, unlike SEASAT, does not possess the means of determining its own wet troposphere correction (i.e., a Scanning Multichannel Microwave Radiometer, or SMMR, which SEASAT carried).

Tapley et al. (1982b) indicate the amplitude of the wet tropospheric correction as being up to 50 cm, and GDR printouts are consistent with this range. Unfortunately for the determination of mesoscale phenomena, however, this correction is spatially highly variable. Figures 1.10 and 1.11 show typical profiles of the wet correction - one the

* The GDR delay corrections are referenced to a vacuum, and so their sign is always negative (see figures 1.10 to 1.13). Note that bias and tilt removal will eliminate the mean effect of the delay corrections, however, allowing their fluctuations to both raise and lower the apparent sea surface.

FNOC channel and the other the SMMR. Qualitatively, the two look similar, but differences on the order of several centimeters are evident and Cheney et al. (1987) report discrepancies of 10 cm as not uncommon. The obvious question arises as to which (if any) of these corrections should be applied.

During SEASAT's geophysical evaluation, Tapley et al. (1982b) compared FNOC-derived wet troposphere corrections of the same sort as GEOSAT'S, with corrections obtained from coincident radiosonde data. The RMS difference was found to be 5.73 cm. Cheney et al. (1987) estimate the accuracy of the GDR WSMR correction as about 5 cm (RMS) over the observation period of the NIMBUS-7 SMMR. The very variability of the wet tropospheric phenomenon argues against the use of this climatic correction, however, so the FNOC correction would seem to be the one of choice. A quantitative comparison between the GEOSAT WSMR and WFNOC corrections is undertaken in the next chapter.

Lybanon and Crout (1987) present an error wavelength of only 200 km for the wet tropospheric correction, which would preclude much error reduction from bias and tilt removal.

Dry Troposphere

The dry troposphere (DFNOC) correction compensates for the radar travel time delay caused by air molecules in the troposphere, and like the preferred wet tropospheric correction, is derived from FNOC data. Values of surface atmospheric pressure are interpolated at the GDR rate from the FNOC model output and are used to calculate the height correction, again based on Saastamoinen (1972). This correction is given by the simple expression $DFNOC = -.2277 P (1 + (0.0026 \times \cos(2 \times LATITUDE)))$ where p = surface atmospheric pressure in mbar and the correction is in cm.

The dry troposphere correction is much better known for GEOSAT than the wet correction, because it is much less variable than the latter. Figure 1.12 displays the DFNOC correction for arc 82 on the fourth repeat cycle and agrees with the known fact that

this correction is always about 2.3 m with an additional long wavelength variation of about 10 cm. This was also observed on printouts of given areas for different repeats on arc 82.

Assuming a 3 mbar surface pressure uncertainty, one can estimate the uncertainty in the Dry Tropospheric correction to be $.2277 \times 3 = .7$ cm. Lybanon and Crout (1987) list the wavelength of this very small error as 1000 km.

An additional phenomenon that affects the sea surface heights is related to the DFNOG correction; and while it is not explicitly included on the GDR, it may be calculated from that correction. This phenomenon is the inverse barometer (IB) effect, where sea level rises and falls with changes in the atmospheric pressure. In essence, one may think of HIGH pressure zones pushing the water away so that it piles up under areas of LOW pressure. A standard rule of thumb is that there is a 1.01 cm rise (fall) in sea level for every 1 mb drop (rise) in pressure below (above) the standard value of 1013.3 mb. This can result in a significant effect of up to ~50 cm.*

Wunsch (1972) has shown that the Rossby radius of deformation is the upper wavelength limit of an expected static IB response (at longer wavelengths, the pressure gradients may be supported by geostrophic currents). What is less clear, however, is the time scale within which the ocean responds to pressure changes. Wunsch (1972), for example, determined that an IB effect exists at mid-ocean islands at periods of greater than 1 day. The inability of subsequent studies to determine more rigorous bounds on the IB effect was the reason for its non-inclusion in the GDR. This interesting problem is explored in the next chapter.

Ionosphere

The ionospheric (IONO) correction to H found in the GDR accounts for the altimeter signal travel time delay caused by free electrons in the ionosphere. Since

* It is important to note that the IB and DFNOG corrections arise from the same source - the atmospheric pressure. This indicates probable correlation between the two, so one must be careful when determining how they affect the sea surface heights. This topic will be treated in more detail in Chapter 2.

GEOSAT does not have a dual frequency altimeter, it cannot measure the delay directly. Instead, the correction is based on the Global Positioning System (GPS) climatic ionosphere model, which is driven by daily values of the solar flux (Cheney et al., 1987).

The amplitude of this correction could be on the order of several decimeters (Lorell et al., 1982), but effects of this magnitude would only be seen during periods of peak solar activity. The next such period will be around 1991, so GEOSAT is gradually experiencing ionospheric error of increasing size. In early 1987, Cheney et al. (1987) reported that the GEOSAT GDR ionospheric correction rarely exceeds 5 cm, which agrees with printouts of arc 82 at that time. They put its accuracy at the 50% level, which is slightly lower than Lybanon and Crout's (1987) estimate of a 4 cm (RMS) uncertainty. An RMS uncertainty of 3 cm is a reasonable choice, and Lybanon and Crout's (1987) error wavelength estimate is >1000 km. Figure 1.13 indicates the long wavelength nature of the ionospheric correction. This behavior is naturally a result of the GPS model containing only long wavelength effects, but these are in fact the dominant ones (Cheney et al., 1987).

1.5 SUMMARY

A zero-order look at the GDR for arc 82 revealed no obvious discrepancies - what is actually seen on GDR printouts and plots agrees with what one expects to find. This simple, but vital step in the verification of the GEOSAT data set has also been useful in providing some insight into the actual physical processes which the GDR attempts to measure and/or model. A result of this insight is an error budget for GEOSAT, which was presented piecemeal in the preceding subsections. The values cited were obtained from a number of sources. When possible, correction errors and their wavelengths were obtained from the original papers of the models used by GEOSAT. In addition, three previously published satellite error budgets provided useful information: Lybanon and Crout's (1987) GEOSAT error budget, Tapley et al.'s (1982) SEASAT error budget, and the budgets of the TOPEX SCIENCE WORKING GROUP (1981). The Lybanon and Crout budget was most applicable, though it did not include tidal errors (other than long wavelength tidal

perturbations of the orbit), and it cited orbit errors appropriate to a different orbital processing scheme than the one currently used in producing the GDR. A summary of the present error budget appears in table 1.2. Note that some of the sources (such as altimeter and orbit) are not broken down into separate components. Such detail is unnecessary for current purposes.

The range resolution of GEOSAT may be determined from table 1.2 by taking the square root of the sum of the squares of the individual correction errors (excepting the orbit error). This results in an overall range resolution of about 13 cm - promising some hope in detecting oceanographic features.

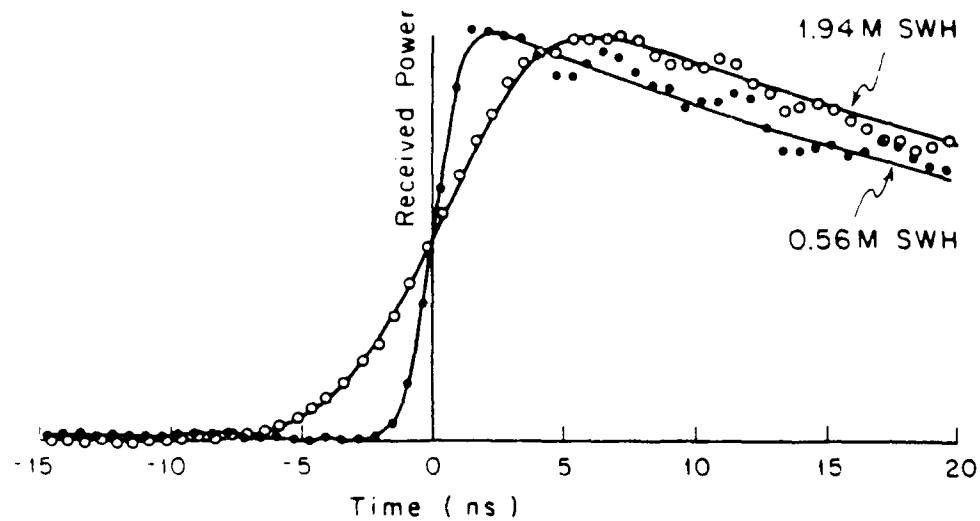


Fig. 1.1a Altimeter return waveform curves. Formed by averaging together many consecutive radar pulses (from Stewart [1985]).

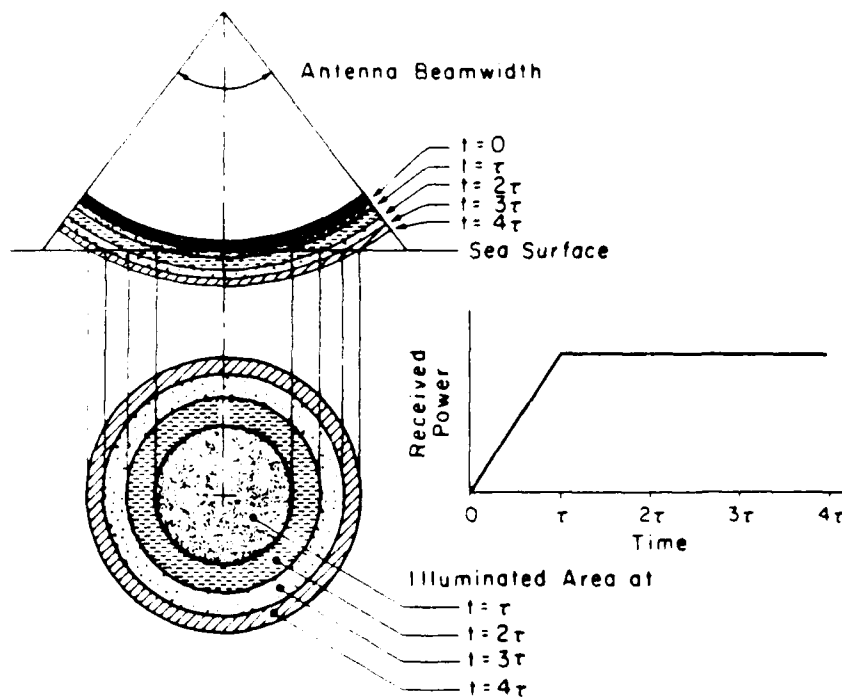


Fig. 1.1b Pulse-limiting in an altimeter. The received power rises linearly with time until the trailing edge of the pulse reaches the surface (from Stewart [1985]).

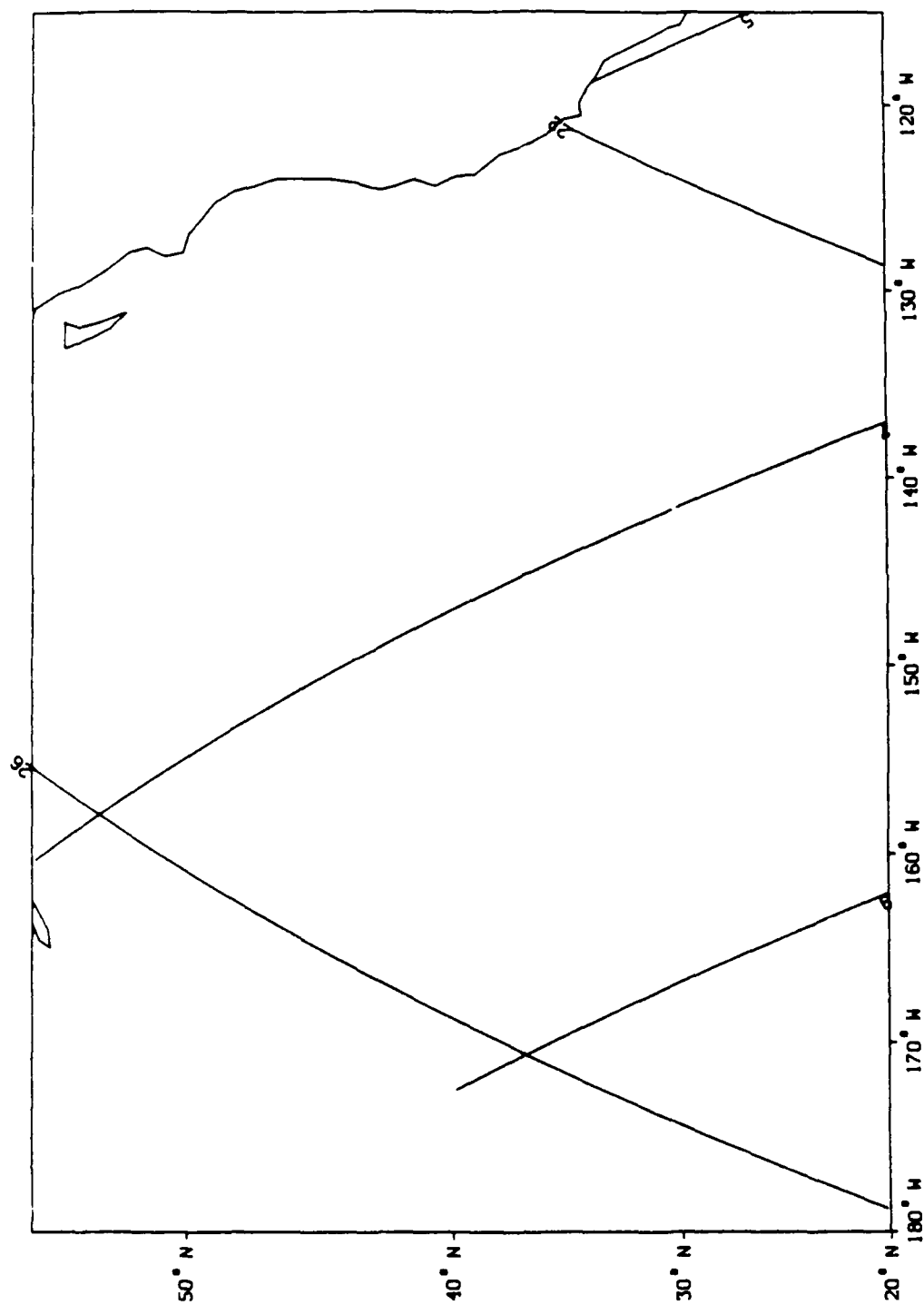


Fig. 1.2 The area under study and GEOSAT groundtracks for day one of the Exact Repeat Mission. Arc numbers are shown where the satellite enters the area.

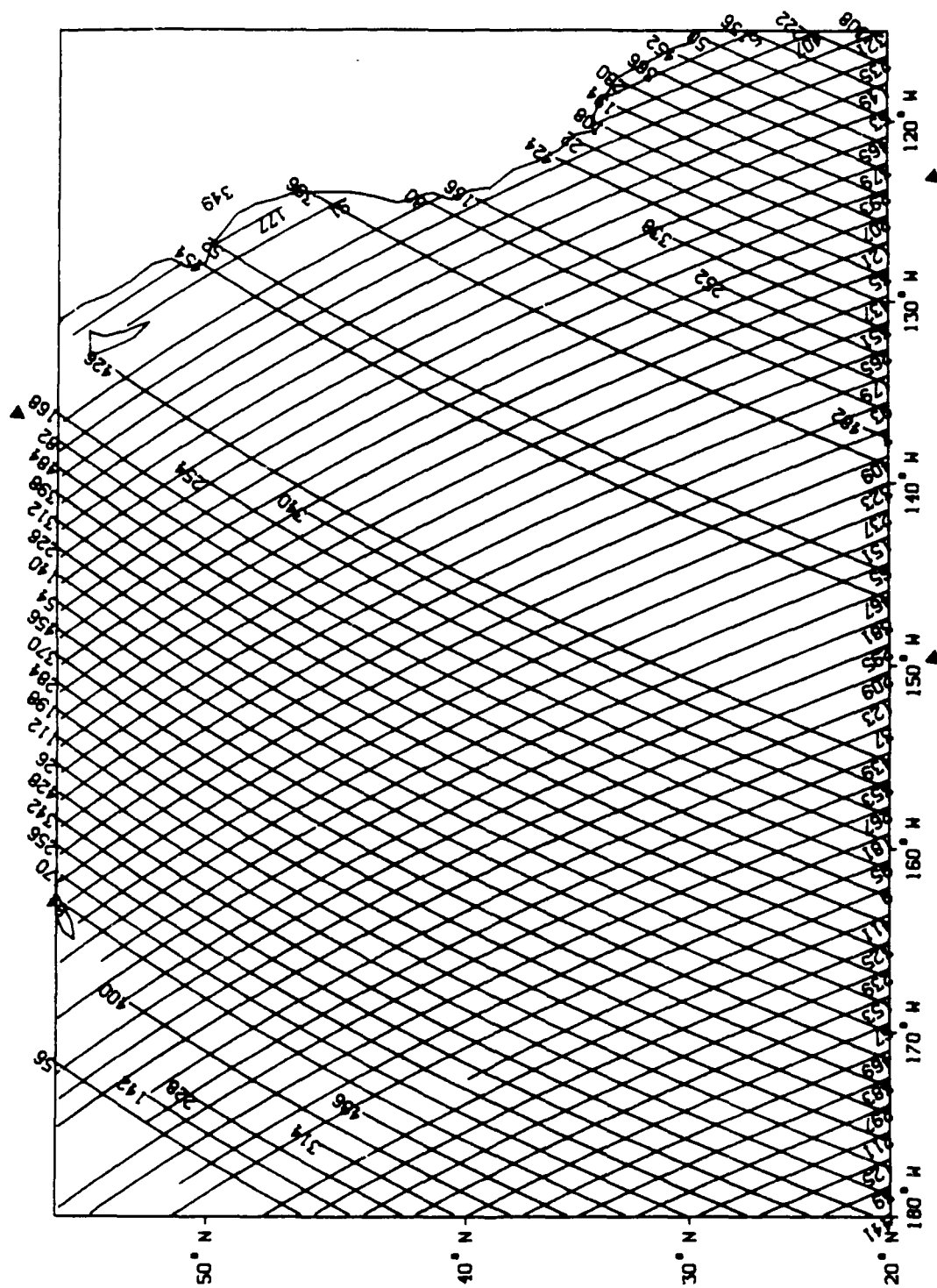


Fig. 1.3 GEOSAT groundtracks for the first repeat cycle. The gaps are due to missing data.

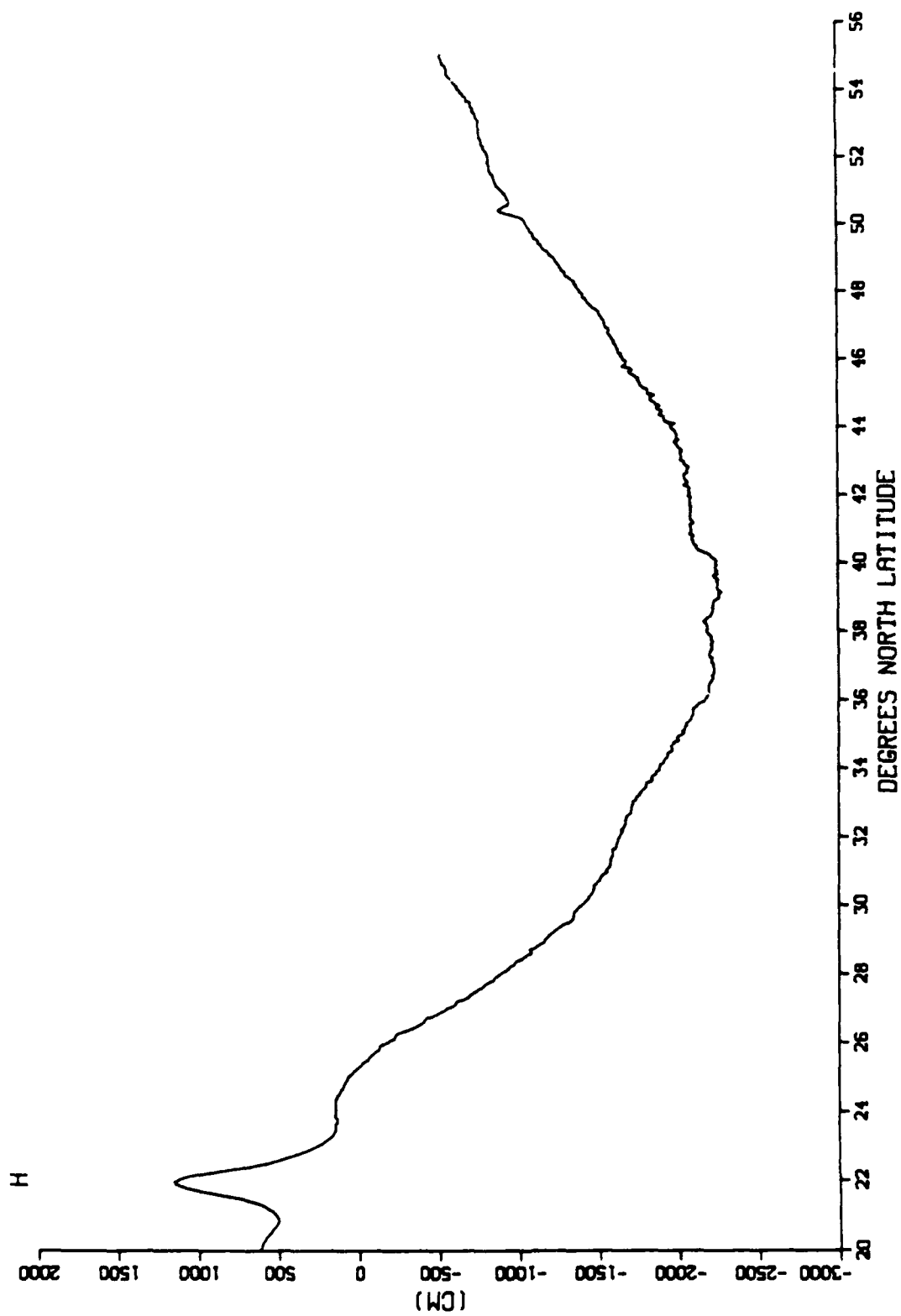


Fig. 1.4 Sea surface height along repeat 4 on arc 82.

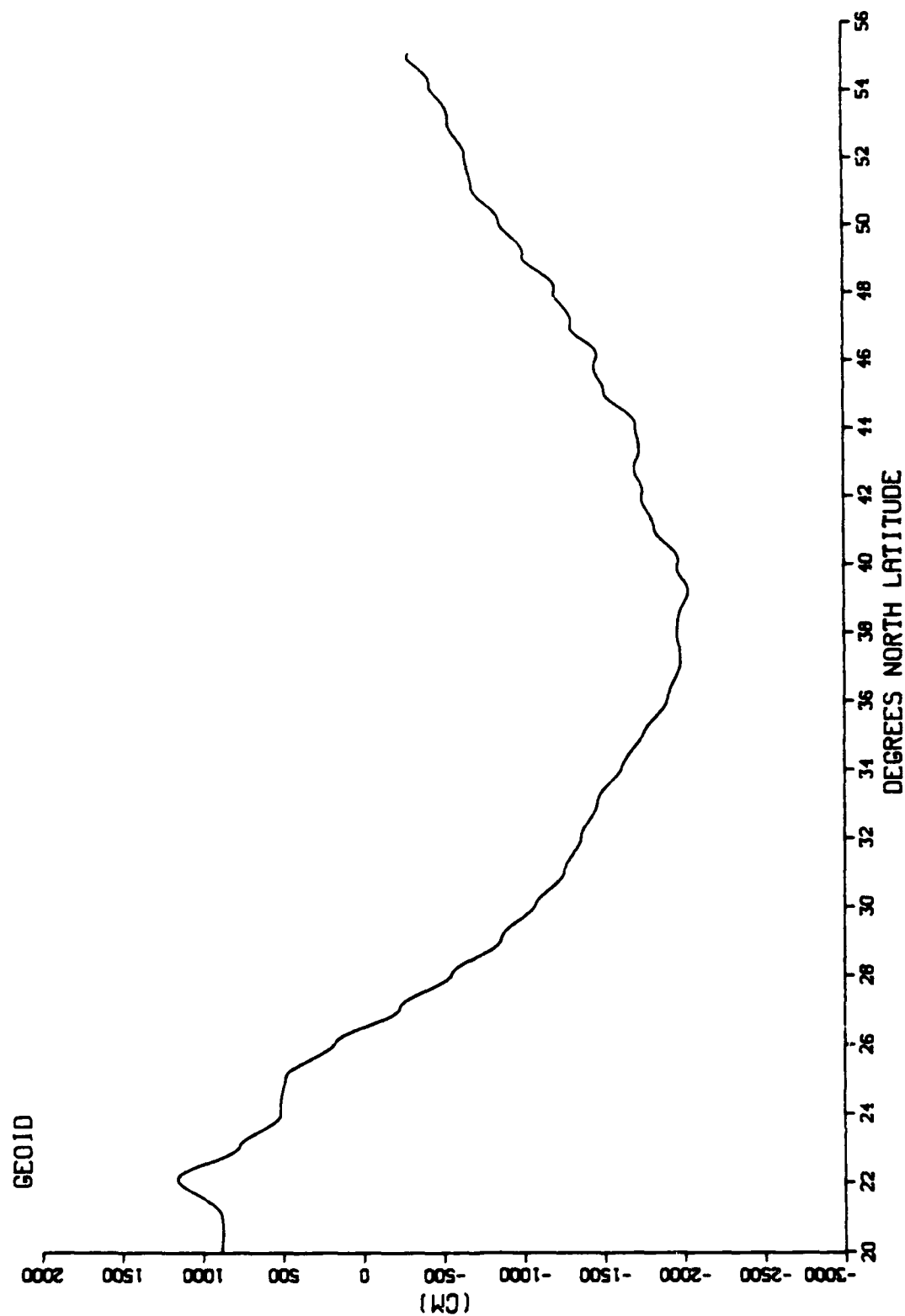


Fig. 1.5 Geoid height along repeat 4 on arc 82. Note the similarity with figure 1.4.

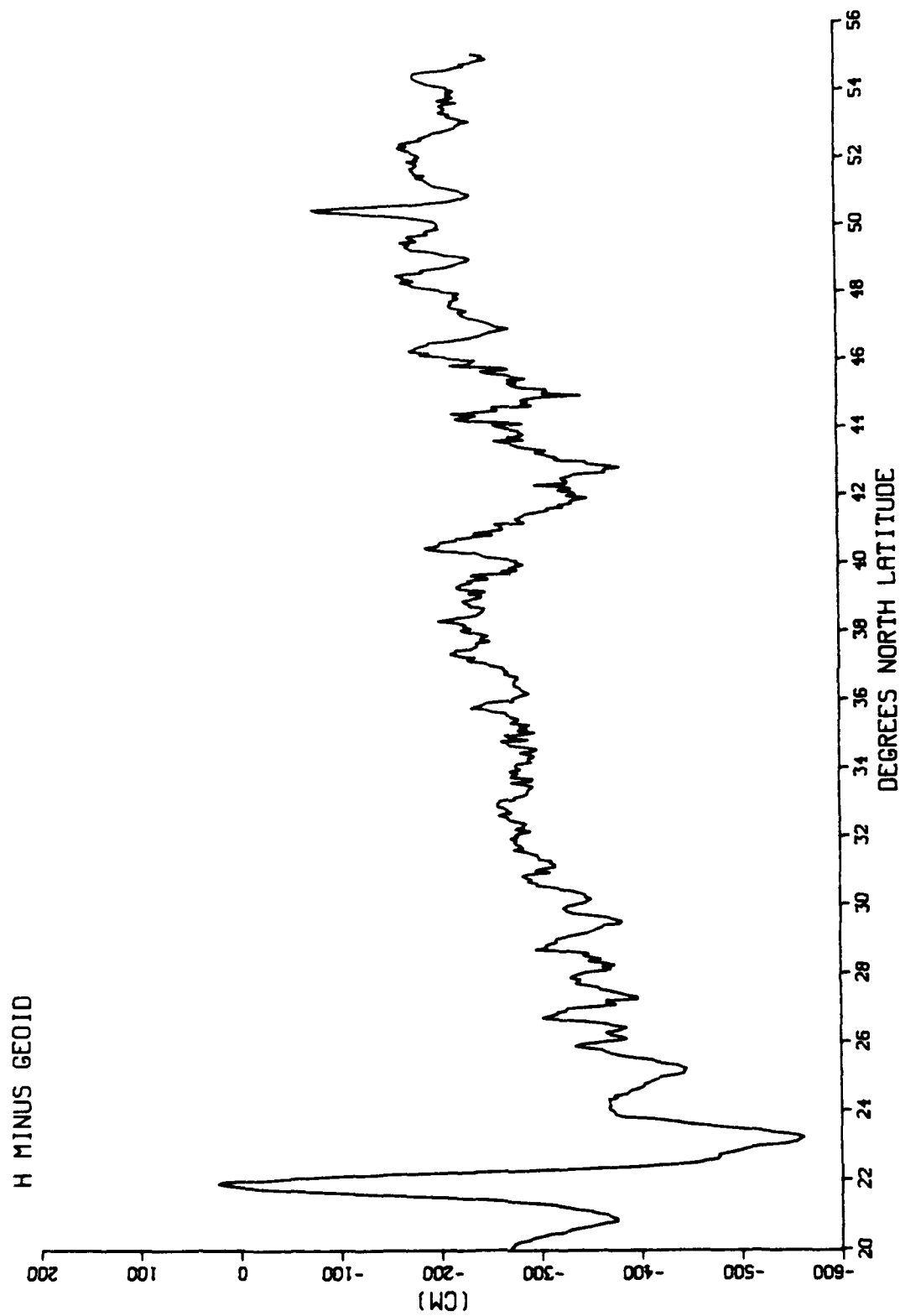


Fig. 1.6 Sea surface height minus geoid along repeat 4 on arc 82. The mid-to-large amplitude features are primarily due to geoid model errors.

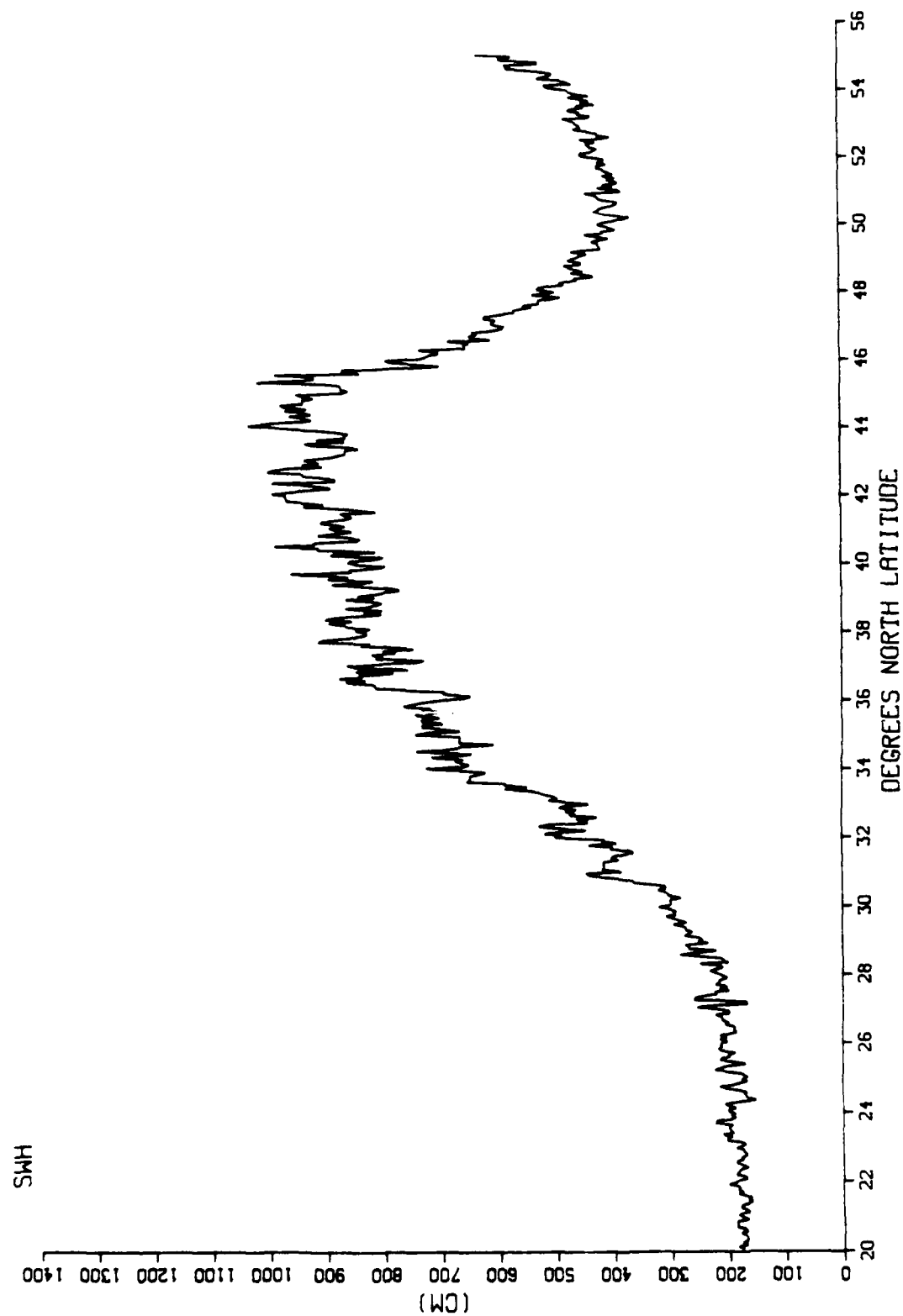


Fig. 1.7 Significant wave height along repeat 4 on arc 82. The electromagnetic bias correction is 2% of the SWH.

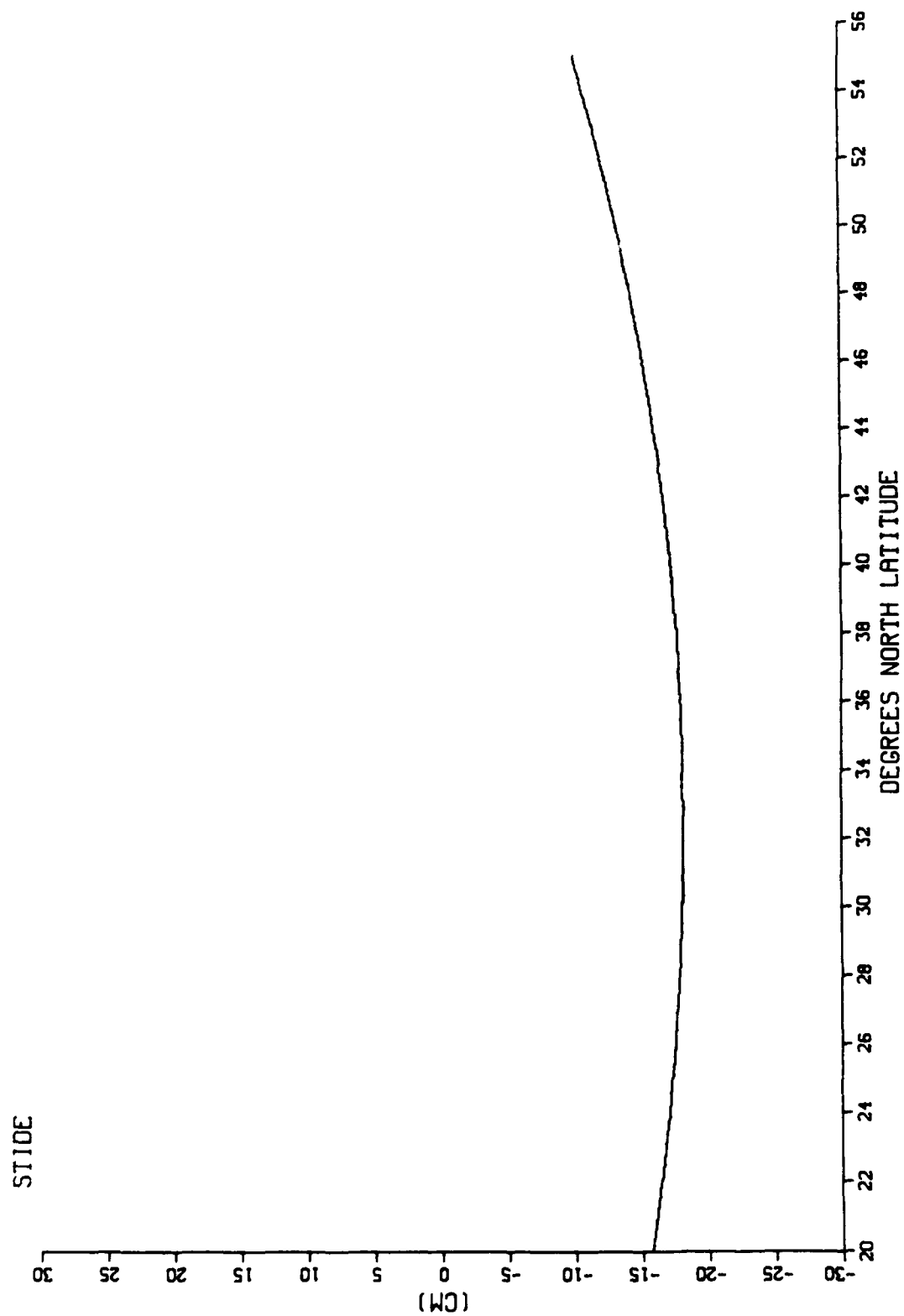


Fig. 1.8 Solid tide correction along repeat 4 on arc 82.

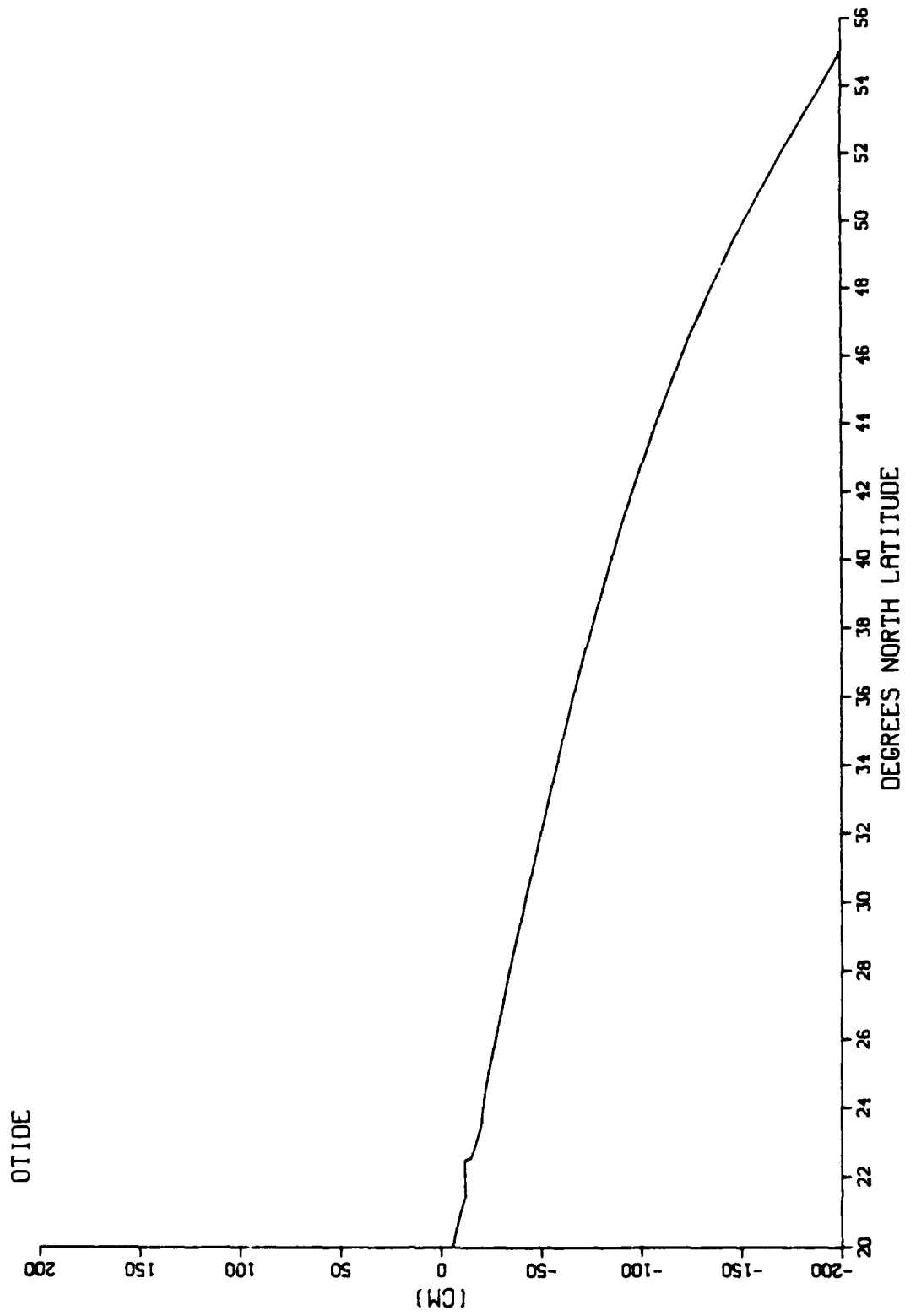


Fig. 1.9 Ocean tide correction along repeat 4 on arc 82.

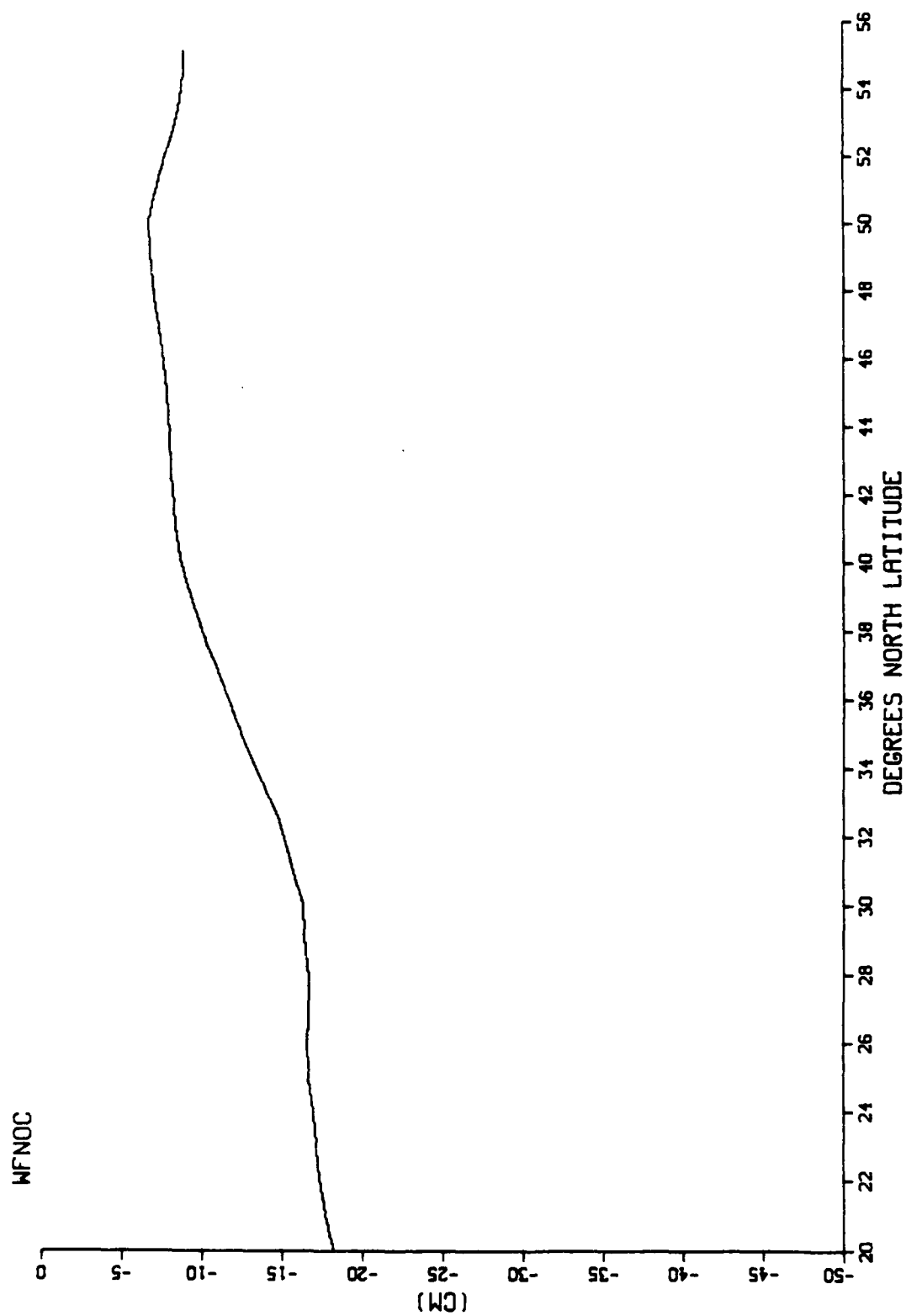


Fig. 1.10 Wet FNOc correction along repeat 4 on arc 82.

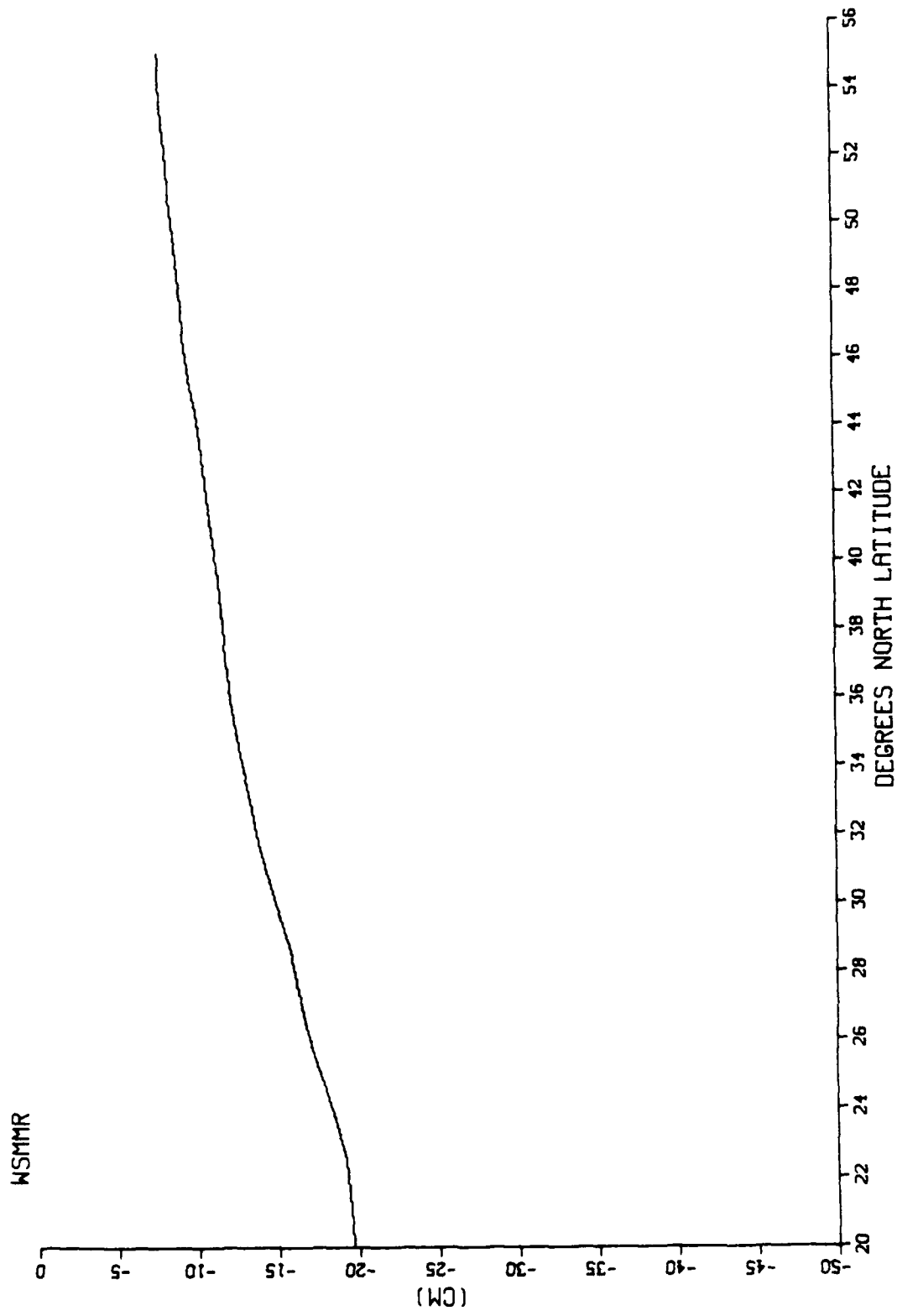


Fig. 1.11 Wet SMMR correction along repeat 4 on arc 82.

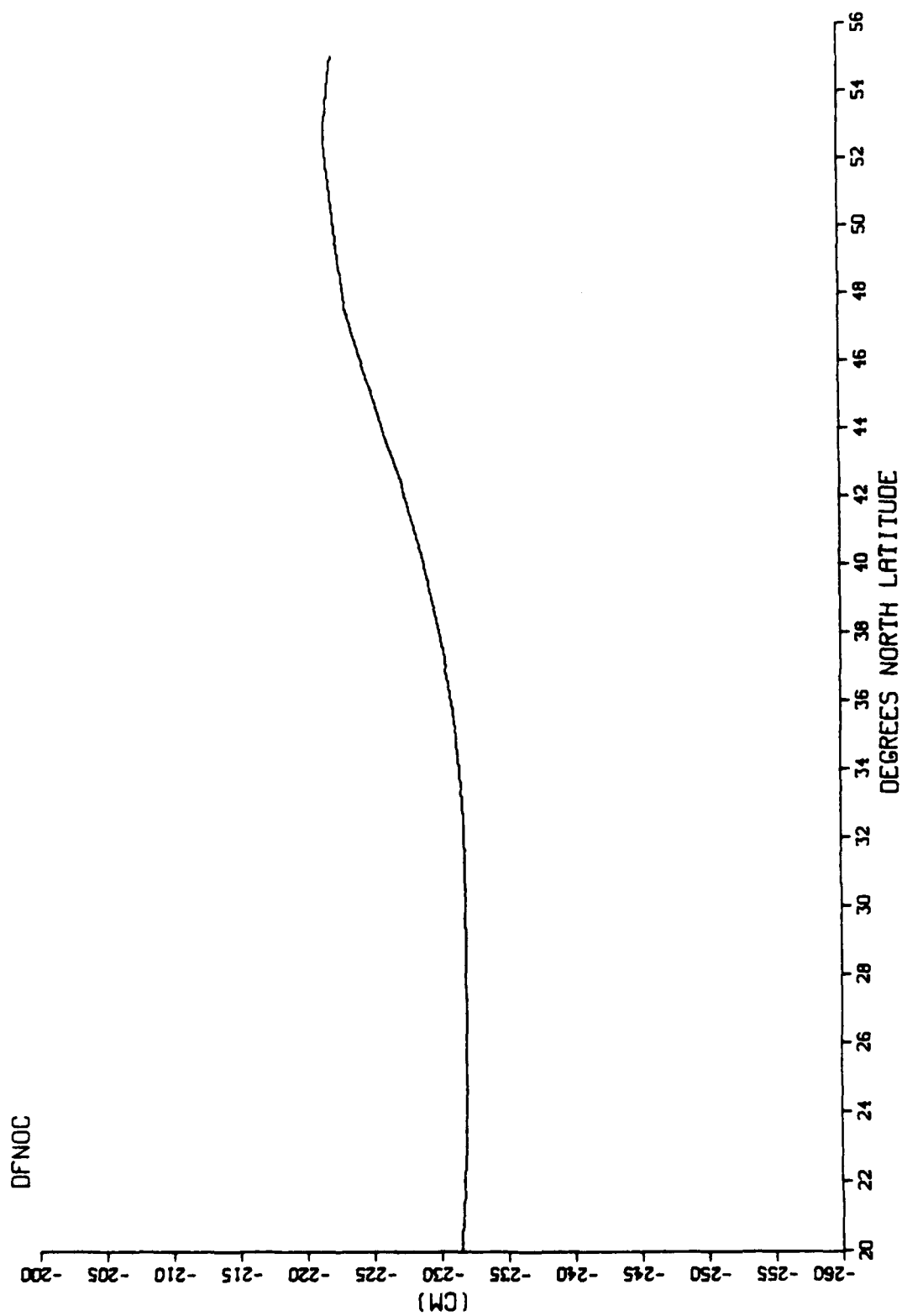


Fig. 1.12 Dry FNO correction along repeat 4 on arc 82.

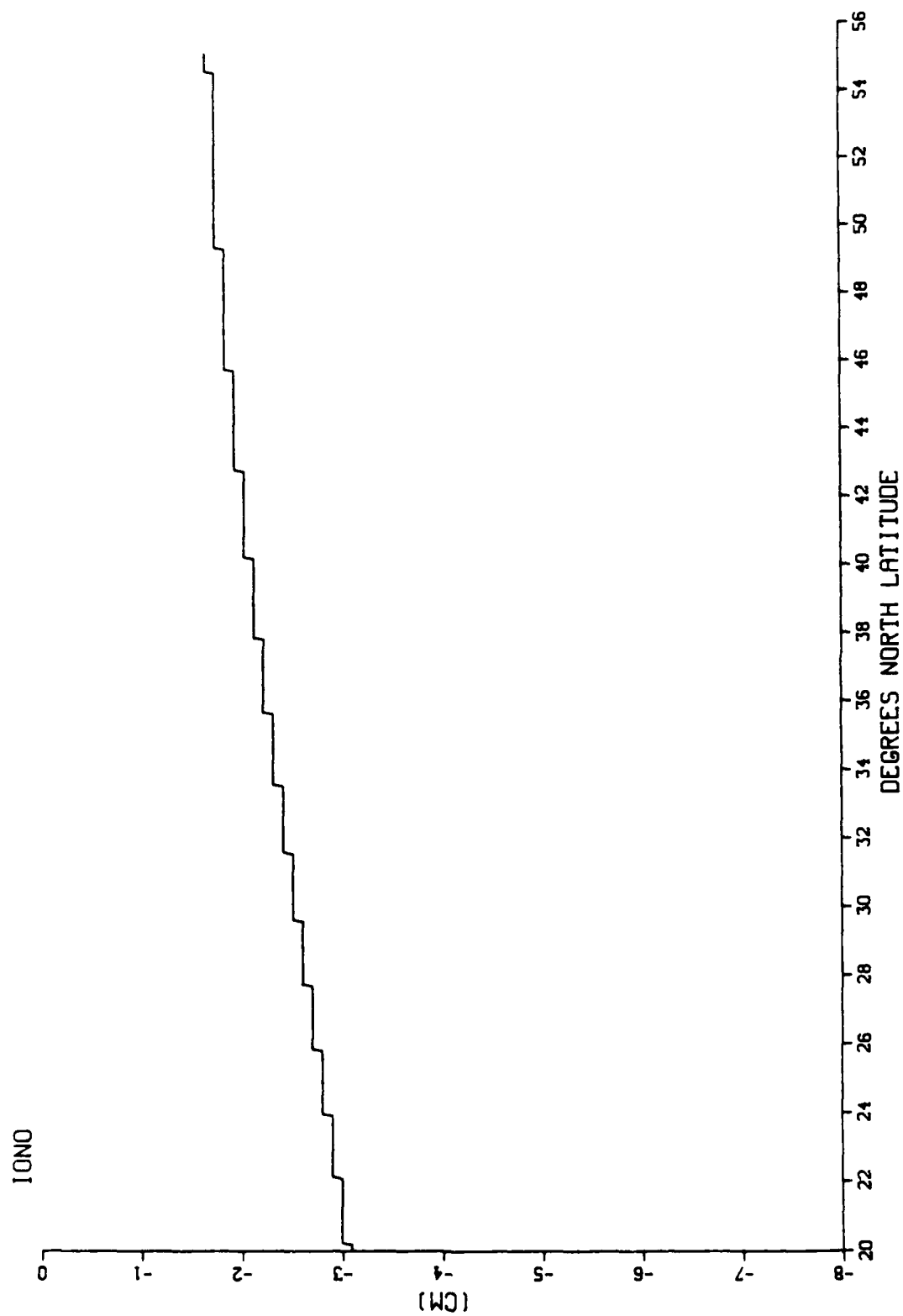


Fig. 1.13 Ionosphere correction along repeat 4 on arc 82.

Station	Rep/Arc	Position	UTC	Local Time	Geosat OTIDE	Tide from Tables (Ref. MSL)	R
Honolulu, HI (21.4°N 158.0°W)	1/267	21.43°N 158.35°W	Nov. 17, 1986 1052	0052	4.3 cm	6 cm	.72
	2/267	21.43°N 158.35°W	Dec. 4, 1986 1205	0205	6.3 cm	6 cm	1.05
	6/267	21.44°N 158.36°W	Feb. 10, 1987 1656	0656	5.1 cm	6 cm	.85
San Diego, CA (32.8°N 117.2°W)	1/5	32.83°N 118.20°W	Nov. 8, 1986 0714	(Nov. 7) 2314	-36.6 cm	-61 cm	.60
	2/5	32.84°N 118.22°W	Nov. 25, 1986 0826	0026	-16.6 cm	-34 cm	.49
	6/5	32.82°N 118.22°W	Feb. 1, 1987 1317	0517	-32.8 cm	-52 cm	.43
Sweeper Cove, Alaska (51.8°N 176.6°W)	1/353	51.86°N 176.24°W	Nov. 20, 1986 1109	0109	-69.3 cm	-76 cm	.91
	3/353	51.87°N 176.24°W	Dec. 24, 1986 1334	0334	-26.5 cm	-28 cm	.95
	5/353	51.92°N 176.31°W	Jan. 27, 1987 1600	0600	23.0 cm	30 cm	.77

Table 1.1 GEOSAT ocean tide due to Schwiderski (1980) compared with tide station values from the U.S. Dept. of Commerce Tide Tables. The column labelled R is the ratio of the GEOSAT tide to the station tide.

ERROR SOURCE	1. ERROR AFTER			2. WAVELENGTH (KM)	COMMENTS
	AMPLITUDE (CM)	CORRECTION (CM 1 σ)			
ALTIMETER	-	3.5	-		1. MacArthur et al. (1987)
MEDIA -EM BIAS	2% of SWH	2.2	200-1000		1.2. Lybanon and Crout (1987) Includes their "EM BIAS" and "WAVE SKEWNESS"
-TROPOSPHERE (WET)	50	5.7	200		1. Tapley et al. (1982b) 2. Lybanon and Crout (1987)
-TROPOSPHERE (DRY)	230	0.7	1000		1.2. Lybanon and Crout (1987)
-IONOSPHERE	5	3.0	>1000		1. Cheney et al. (1987) 2. Lybanon and Crout (1987)
ORBIT	-	300	10000-40000		1. Born (1988) 2. Tapley et al. (1982)
OCEAN TIDE	100	10.0	500-1000		1. Schwiderski (1980) 2. Tapley et al. (1982)
SOLID TIDE	20	1.0	20000		1. Cheney et al. (1987) 2. Tapley et al. (1982)

NOTES:

SWH = 2 m, wave skewness = 0.1
 ± 3 mb surface pressure

Table 1.2 GEOSAT error budget. Comments refer to sources of data in the numbered columns.

CHAPTER TWO - EVALUATING THE DATA

2.1 COLLINEAR PROCESSING SCHEMES

The purpose of this chapter is to determine which of the GDR corrections should be made to the GEOSAT sea surface heights and if any successive-point averaging is possible. To this end, I used an algorithm designed to investigate oceanic variability while minimizing the effects of unknowns. Various collinear schemes fit these criteria, and their methodology is as follows (equations 1 through 3 are due to Calman [1987]).

For each repeat pass, one seeks the time varying component of the dynamic ocean topography $\eta'(x,t)$, where the total dynamic topography $\eta(x,t)$ is the sum of $\eta'(x,t)$ and the mean dynamic topography $\bar{\eta}(x)$. But the total dynamic topography for a repeat is also given by

$$\eta(x,t) = h(x,t) - G(x) \quad (1)$$

where $h(x,t)$ is the measured sea surface height profile for the repeat (i.e., the H channel in the GDR), and $G(x)$ is the geoid height. By the collinear scheme, one averages together an ensemble of repeat passes on a given arc to form a mean height profile $\bar{h}(x)$, where

$$\bar{h}(x) = \bar{\eta}(x) + G(x) \quad (2)$$

That is, the mean profile is the combination of the mean dynamic topography experienced by all repeats, and the geoid - which is the same for all repeat passes on a given arc (not quite, but that will be seen shortly). Adding (1) and (2) and simplifying, one finds that

$$\eta'(x,t) = h(x,t) - \bar{h}(x) \quad (3)$$

This result shows that for a given pass, the dynamic topography (also known as a difference profile) may be found by subtracting the mean sea surface height profile for the arc from the sea surface height profile for the pass. Note that no explicit knowledge of the geoid is needed with this method.

There are three drawbacks to collinear schemes. The first is that knowledge of the mean circulation is lost because the mean dynamic topography has been used to form the mean sea surface. I accept this limitation in view of the aims of this work. The second is more troublesome and is residual geoid contamination. This effect is due to the fact that the

data points for the successive repeat passes do not exactly coincide, either along or cross track (the cross-track spread is less than ± 1 km and the alongtrack spread can be limited to $\pm \Delta/2$, where Δ is the distance between successive data points). Wherever there is a significant geoid gradient, the resultant will be that the ensemble of passes will not all see the same geoid, and the mean profile $\bar{h}(x)$ will be contaminated by an extra geoid term $G'(x)$. When difference profiles are created by subtracting out the mean, this contamination will remain and may be mistaken for oceanographic signals. Fortunately, residual geoid contamination is usually easy to spot as it habitually occurs in those areas where the geoid is changing rapidly. Unfortunately, though, these same regions often contain ocean currents of interest which may not be visible over the contamination. These areas may be found by looking at arc mean profiles, as will be seen presently. The third drawback to collinear schemes is the possibility of temporal aliasing. Since these techniques rely on repeated sampling of the same arcs, any phenomena having periods at or near integral multiples of the repeat period will appear invariant. Similarly, those processes which change very slowly over the length of time needed to form a mean profile may add unwanted energy to that mean and substantially alter the difference profiles. The latter occurrence is explored later in this chapter.

2.2 A COLLINEAR ALGORITHM

The algorithm which created the difference profiles used to determine GEOSAT correction applicability is as follows:

- 1) Delete data points not over water, or flagged bad in the H channel
- 2) Remove the low order Rapp geoid from the H values on a pass
- 3) Apply a chosen GDR correction (if any) to the resultant values
- 4) Remove any spikes from the corrected profile
- 5) Detrend the profile (i.e. - remove bias and tilt)

6) Average a collinear ensemble of such profiles together to form a mean sea surface height profile for that arc. Figures 2.1-2.3 show such a profile for arcs 82, 209, and 293.

7) Subtract this mean profile from each pass in the ensemble (where each pass is always edited with steps 1) thru 5)) to create the set of difference profiles (i.e. - $\eta'(x,t)$). Such a set for arc 82 may be seen in figures 2.4 and 2.5.

From these difference profiles, quantities such as RMS alongtrack variability and wavenumber spectra may be calculated, in order to evaluate the efficacy of the chosen correction. Prior to passing such judgement, however, a number of checks on the algorithm were performed. These are now summarized as some of them illuminate the finer points of the subsequent analysis:

Subtraction of the Rapp geoid was done to make plotting and inspection of the height profiles easier. Since this geoid is of low order, it is nearly unchanged from repeat to repeat (even with cross and along-track offset), and so removing it from the sea surface heights has negligible effect on the difference profiles.

The proper application of the correction channels was verified by comparing non-detrended profiles before and after correction with plots of the correction channels themselves. That is, if a plot of the OTIDE correction for a repeat pass showed that the sea surface height should be decreased by 50 cm at 40°N, for example, profiles of that repeat before and after OTIDE correcting were inspected to ensure exactly that happened. No problems were found in this regard.

The spike editor is based on a simple first difference scheme of each point on a corrected height profile with its predecessor. If the difference exceeds a set value (30 cm was found to be a good criterion), then the spike value is replaced by the average of its neighbors to either side. This technique was found to work well on isolated spikes, but not in areas with sustained large first differences (such as regions of high geoid variability). This limitation was not a problem in practice as such areas were deleted anyway to avoid

geoid contamination. The editor was checked visually on a number of spikes and ensured that any spikes which did appear in the final difference profiles were less than 40 cm in magnitude. As shown in Appendix 1, such residual spikes have only a small effect on variability calculations, and the amount may be quickly estimated, if necessary.

The detrender was checked numerically to ensure it removed bias and tilt from the corrected height profiles; and also visually, to ensure it did not change the "look" of the profiles. An additional benefit of this process was a printout of the bias removed from each pass, where the bias is mostly the orbit error. The RMS bias over 10 passes on arc 82 was around 1.5 m, which is comparable with the known orbit error.

The averaging method used is a point-to-point match up of corresponding data points on the various repeat passes along the chosen arc. Alongtrack offsets are minimized by sliding the passes so that all starting latitudes are as closely packed as possible around some reference latitude. The sliding results in the data points of the various passes being within a range of $\pm\Delta/2$ where Δ is the interval between successive data points (~ 6.7 km). As mentioned in the last section, geoid contamination is a problem in regions of large geoid variability, which are identified and excluded from the analysis. To check the sensitivity of the difference profiles and variability calculations to the sliding scheme, the algorithm was performed several times on a collinear ensemble, with slight perturbations in the sliding. It was found that variability calculations and the difference profiles were affected only very slightly by such changes except in areas of large geoid gradient.

The difference profiles were compared with variability calculations and wavenumber spectra to ensure that all were corroborative. For example, a difference profile which showed a significant long wavelength variation would be found to have a large RMS alongtrack variability and high power density at long wavelengths. As a quantitative check, the area under several power density spectra was determined for comparison with the calculated alongtrack variance (RMS variability squared). No discrepancies were noted.

2.3 THE TEST ARCS

Once the proper operation of the collinear algorithm was assured, three arcs within the area were chosen to investigate the efficacy of the correction channels when applied to the sea surface heights. These were arcs 82, 209, and 293. They were chosen for length, good coverage through a number of repeat cycles, and to sample different portions of the area. They are specially marked in figure 1.3.

Arc 82 is a descending arc, and its mean profile was formed from 10 repeat passes (numbers 1-6,8-10,13). Eighteen repeat cycles were available at the time, and the eight not used were rejected due to numerous data dropouts. Arc 209 is an ascending arc whose passes during a given repeat cycle occur some 4 1/2 days later than those along arc 82. This arc experienced fewer dropouts, enabling 14 repeat passes to be used in creating the arc 209 mean (numbers 1-6,8-14,17). Arc 293 is an ascending arc, whose passes are about 3 days later than those of arc 209. Arc 293 experienced no major dropouts throughout the 18 repeat cycles and so all passes were used in forming its mean. The mean sea surface height profiles along these three arcs, with no correction channels applied, are shown in figures 2.1 through 2.3.

For each arc, the effects of making the various corrections were investigated in the following way: First, the mean profile was examined to spot those areas where the mean sea surface changed rapidly. This examination was done even though the Rapp geoid was already removed, because the features on the mean were still largely a result of the real geoid (because the Rapp model is of too low an order to accurately reflect shorter wavelength geoidal variations). Thus, those areas where the mean sea surface was highly variable with horizontal distance were the same areas where possible geoid contamination of the difference profiles could be expected. A simple look at the mean profile often sufficed here, though a first difference plot of the profile was also useful. Those areas where geoid contamination was suspected were then examined on a set of non-corrected difference profiles. If strong signals habitually appeared there, that particular latitude band

was eliminated from the arc (the test arcs were chosen to minimize this possibility). This elimination was done in the southern region of arc 82 (Hawaiian islands) and the northernmost part of arc 209 (Aleutian chain). While some oceanographic features may have been lost in the process, that was considered acceptable since the corrections, and not the oceanography, were the focus at this point.

With geoidal contamination largely removed, the algorithm was first used to create a set of difference profiles (one for each pass that helped form the arc's mean profile), with no correction applied in step 3. For each difference profile, the RMS alongtrack variability (σ) was calculated. The set of σ were then averaged together to determine the mean alongtrack variability of the difference profiles on the arc ($\bar{\sigma}$). This mean variability was used in evaluating the effect a particular GDR correction had on the ensemble of difference profiles for the test arc. An additional statistic computed was the sample standard deviation of the individual σ about $\bar{\sigma}$ (SSD). The SSD was essentially a measure of how different the alongtrack variabilities of the individual difference profiles were from each other. This statistic was of some use in evaluating random corrections, but was most helpful when used in conjunction with $\bar{\sigma}$, in cases where the mean profile was aliased. The statistics for the no-correction case comprised the standard against which analogous statistics were compared after rerunning the algorithm separately for each possible correction. The results of these runs for the three test arcs are listed in tables 2.1 through 2.3, and are discussed individually.

Note that this work uses RMS variability (or standard deviation) instead of variance. This choice was made because much of the GEOSAT literature does likewise, and the altimeter errors under investigation have uncertainties typically given as RMS values.

2.4 ARC 82

As previously mentioned, the mean profile for arc 82 is shown in figure 2.1. The difference profiles for the 10 passes used to make the mean are shown in figures 2.4 and

2.5, with no GDR corrections applied. Note how the region of high geoid variability to the south has been deleted. I refrain from looking for mesoscale features at this point and focus on the GDR corrections.

Table 2.1 lists the statistical results for the various corrections applied to the sea surface heights of the repeat passes along arc 82. As an example of how to use this table, note the row corresponding to repeat 4. With no corrections applied to any passes, the difference profile for this repeat had an alongtrack RMS variability of 9.58 cm. When the EM BIAS correction was applied throughout, the RMS variability for the repeat 4 difference profile increased to 11.43 cm. Now observe the last two rows denoting all repeats. With no corrections applied, the mean of the ten difference pass variabilities was 7.28 cm with an SSD of 1.91 cm. When the EM BIAS correction was applied, $\bar{\sigma}$ rose to 7.34 cm, and the SSD rose to 2.21 cm. The significance of these numbers will be explained shortly.

For a random phenomenon, alongtrack variability should almost always decrease upon the application of a well-modelled correction, as the correction will reduce an apparent perturbation to the sea surface. Accurate corrections are desirable in that they can remove non-oceanographic features from the difference profiles and so make it easier to spot the oceanographic ones. If the phenomenon is poorly modelled, variability will tend to increase upon correcting, and oceanographic signatures may be obscured. The behavior of the variability can best be stated in terms of the coherent and incoherent power as follows:

Assume that the sea surface observed by the altimeter (o), is the desired surface (d), plus some phenomenon (x), which may be modelled. We wish to remove x from o, in order to study d. Thus

$$d = o - x$$

Fourier transforming and taking the complex conjugate of both sides gives

$$\hat{d} \hat{d}^* = (\hat{o} - \hat{x})(\hat{o} - \hat{x})^*$$

Expanding the right hand side and taking expected values throughout produces

$$\langle \hat{dd}^* \rangle = \langle \hat{oo}^* \rangle - \langle \hat{ox}^* \rangle - \langle \hat{o}^* \hat{x} \rangle + \langle \hat{xx}^* \rangle$$

The terms within the brackets may be replaced by the appropriate spectra, giving

$$\Phi_{dd} = \Phi_{oo} - 2\text{Re}[\Phi_{ox}] + \Phi_{xx} \quad (4)$$

where Φ_{dd} is the power spectrum of the desired sea surface profile, Φ_{oo} is the power spectrum of the observed (difference) profile, Φ_{xx} is the power spectrum of the modelled correction for the particular profile, and Φ_{ox} is the cross power spectrum between the observed profile and the modelled correction. It is assumed that the observed profile is incoherent with any modelling error. If the model of the phenomenon accurately reflects its true effect on the sea surface, then $\Phi_{ox} \simeq \Phi_{xx}$ and (4) becomes

$$\Phi_{dd} \simeq \Phi_{oo} - \Phi_{xx} \quad (5)$$

Thus, the variance (and hence the alongtrack variability) of the corrected profile (d) will tend, on the average, to be less than that of the uncorrected profile (o) when the correction is very accurate. On the other hand, if the model of the phenomenon is a poor one, its profile will bear little resemblance to the observed sea surface profile, meaning that $\Phi_{ox} \simeq 0$. In that case, (4) becomes

$$\Phi_{dd} \simeq \Phi_{oo} + \Phi_{xx} \quad (6)$$

Alongtrack variability in general increases when the model of the phenomenon is inaccurate.

This discussion has implicitly assumed that the mean surface from which the observed difference profiles are created has not had the phenomenon aliased into itself. When this occurs, additional terms appear on the right hand side of (4). The short time scale and aperiodic nature of all the non-tidal corrections suggests that they do not cause this difficulty, however; and aliasing of the tides is treated separately in this chapter.

The results of (5) and (6) indicate how the statistics mentioned earlier may be used to judge the effectiveness of a particular GDR correction. If the correction accurately models the phenomenon in question on a particular repeat, then that repeat's difference profile should have a lower σ than without the correction. If the correction does well over

the ensemble of repeats, then $\bar{\sigma}$ will be lower than for the no-correction case. In addition, if one uses the a priori knowledge that the test arcs are in a fairly quiet region of the Pacific, then removing non-oceanographic signals with an accurate correction will make the difference passes look more alike. This will result in similar variabilities between the repeats, and a smaller SSD after correcting. Of course, if the phenomenon has very small variability to start with, then Φ_{xx} will be very small, and correcting for it will have little effect on the difference profiles. In that case, there is no need to bother making the correction.

Referring back to the statistics on EM BIAS mentioned earlier, one can conclude that this correction was not well modelled for the repeats on arc 82.

The first step taken in examining the correction channels as they affected arc 82 was to identify those which made no difference. To this end, a simple criterion was used: If the effect of a correction on the variability of a difference profile did not exceed an assumed instrument noise of 3 cm (RMS) the correction was deemed to have made no difference. 3 cm was used instead of the published 3.5 cm in order to reject fewer values. To illustrate this, again consider repeat 4 in table 2.1, with an RMS variability of 9.58 cm. Adding and subtracting noise of 3 cm (RMS) produces upper and lower bounds of 10.04 cm and 9.10 cm respectively (combining RMS values entails taking the square root of the sum or difference of the squares of the values). The only corrections which caused the difference profile variability of repeat 4 to exceed these bounds were EM BIAS and WFNOC, which were thereby judged to be 'significant' corrections.

By the stated criteria, the STIDE, WSMR, and IONO corrections made no difference for arc 82. This judgement, based on the statistics of table 2.1, was also corroborated with difference profile printouts. In no instance was there any discernable difference between the profiles before and after making the indicated corrections. Figures 2.6a and 2.6b compare spectra of a typical difference profile (rep 9 in this case), with the spectra of its STIDE and WSMR correction channels (the IONO channel variability was

very slight and produced a power spectrum orders of magnitude lower than those of the STIDE and WSMMR channels). Note how, even at long wavelengths, the variance of the correction channels is some two orders of magnitude less than the variance of the difference profile. The low power of the corrections indicates that they do not vary much over the arc, and as mentioned, this is why they had no significant effect when applied. As an aside, note the red spectrum for the difference profile, which is characteristic of oceanic processes.

Using table 2.1, the remaining corrections were examined by finding those repeats where the corrections had the most significant effect on variability, in comparison to the noise bounds. For each correction, four repeats were chosen - the two with the most significant variability reduction upon application of the correction, and the two with the most significant variability increase. The appropriate repeats for each correction appear in figures 2.7 through 2.10. On each figure, the corrections for the individual repeats are plotted with the correction causing the most significant variability reduction on the top, down to the correction causing the most significant variability increase on the bottom. These figures were used to try and determine what factors are involved in whether or not a given correction will cause a variability increase or decrease.

Electromagnetic Bias

Note that figure 2.7 is a plot of significant wave height for the listed repeats, which is the source of the EM BIAS correction (the latter being 2% of SWH). Two observations may be made from these plots: First, the EM BIAS correction appears to do very poorly when the SWH is large. Repeat 4 has much higher SWH than the other 3 repeats pictured in figure 2.7, and also had the most significant variability increase upon application of the EM BIAS correction. Figure 2.11a is a spectral plot comparing repeat 4's difference profile before and after correcting for electromagnetic bias, and shows that the variability increase occurred mainly in the long wavelengths (>400 km), though the confidence limits prevent one from stating this with conviction. A better indicator of which difference profile

wavelengths would be most affected by the EM BIAS correction may be seen in figure 2.11b, which compares the spectra of repeat 4's difference profile and its EM BIAS correction. Here it is very evident that only at wavelengths around 400 km and longer, does the EM BIAS variability approach that of the difference profile. Before proceeding, it must be pointed out that the converse of the first observation on electromagnetic bias is not true. That is, a small SWH does not guarantee variability reduction upon correcting for EM BIAS. See repeat 13 for an example of this. A plausible reason for the variability increase when SWH is large is presented in the section on arc 209.

The second observation made from figure 2.7 is that when SWH is large, the short wavelength noise of the difference profile is increased. From figure 2.7, compare repeat 13, having small SWH alongtrack (~ 2 m); with repeat 4, that has peak SWH values around 10 m. From figures 2.4 and 2.5, note how much quieter repeat 13's difference profile is at the shortest wavelengths compared to repeat 4's. This effect can be seen more quantitatively in figure 2.12, where, through most of the short wavelengths, repeat 13's power density is around an order of magnitude less than repeat 4's. As a final example, one may even note that the latitude where repeat 4 has its largest SWH ($\sim 33^\circ$ - 46° N) is the area with the largest spikes on its difference profile. The most obvious reason for this phenomenon is that high SWH worsens the point-to-point precision of the altimeter itself. Refer back to figure 2.12; if one considers the generally white portion of both spectra ($\lambda \leq 40$ km) as system noise, one can graphically integrate under each spectrum from $\lambda = 40$ km to 14 km (the Nyquist limit) and obtain the following estimated noise-induced variances: for repeat 13, 4.6 cm^2 , and for repeat 4, 19.5 cm^2 . These variances correspond to altimeter precisions of 2.1 cm and 4.4 cm (RMS), respectively. Repeat 13 does better than the rated noise floor of 3.5 cm and repeat 4 does worse, due to the high significant wave height. A useful pursuit in future studies would be to empirically find the altimeter noise floor as a function of SWH, especially for the larger wave heights.

Electromagnetic Bias is a rich enough subject to warrant further discussion in this work, though based on the ensemble statistics thus far, it is not recommended for application to the sea surface heights.

Ocean Tide

Figure 2.8 shows the repeat cycles whose OTIDE corrections had the most significant effect on variability. It is plain that this effect is due to the long wavelength curvature of the ocean tide profiles along arc 82. Of all the correction channels, OTIDE caused the largest changes in difference profile variability upon application. Figure 2.13a shows the spectrum of the repeat 10 difference profile before and after OTIDE correcting, and indicates that the wavelengths affected are the longer ones (≥ 200 km). As with EM BIAS, the confidence limits make the results in the 200-400 km wavelength band somewhat ambiguous, and so figure 2.13b compares the difference profile spectrum with the OTIDE channel spectrum. Here, the confidence limits are less of a problem, and one sees that the OTIDE power density is much too small compared to the difference profile power density at 200 km wavelength to have any significant effect. The actual wavelengths affected by the OTIDE correction are thus more likely 300-400 km and longer, as one would expect due to the long wavelength nature of this phenomenon. The OTIDE profiles in figure 2.8 indicate that the tide is probably being time aliased. This can be seen in the similarity of the tidal profiles between repeats near to each other in time.

Examining the ensemble statistics in table 2.1, the OTIDE results at first appear confusing. On one hand, $\bar{\sigma}$ rises when the OTIDE correction is made, which is not desirable. In contrast, however, the SSD falls after the data is corrected for ocean tide, indicating that the repeats tend to look more alike in terms of variability. As mentioned before, if one accepts that this is a quiet portion of the Pacific, then this similarity is desirable. A clear example of how the OTIDE correction makes the difference profiles more alike may be seen in figure 2.14. Figure 2.14a shows spectra of the two difference profiles with the most difference in variability before OTIDE correcting (repeats 3 and 10).

Figure 2.14b shows them after OTIDE correcting. Note how the long wavelength variability of repeat 10 has been reduced to the point where the two repeats, within the confidence limits, have essentially the same power spectrum.

As will be shown later, the ambiguous ensemble statistics are a characteristic of aliasing, which will be examined in more detail in the arc 293 section.

Wet FNOC

Table 2.1 shows that, while some repeats had a significant change in variability upon application of the WFNOG correction, the change was not large, and was just as likely to be a variability increase as a decrease. Figure 2.9 does not indicate any special criterion for determining whether the WFNOG correction will increase or decrease the variability, and the ensemble statistics indicate that the correction really did not make much difference anyway. This result is supported by figure 2.15, which indicates that the power density of the WFNOG correction is small compared to even a relatively quiet difference profile (repeat 9). For these reasons, the GDR WFNOG correction is deemed unnecessary, pending investigation of the remaining test arcs.

Of note at this point is the distinction between the modelled WFNOG correction and the true wet troposphere delay correction. The former had little effect on the difference profiles, while the latter is often much more robust. That is, true wet tropospheric effects of short wavelength and large amplitude may easily be mistaken for oceanographic signals. Until coincident measurements of this phenomena are available from radiometers, it appears wisest to avoid making the inherently smooth model-derived corrections.

Dry FNOC

As opposed to WFNOG, where variability increased or decreased with near equal regularity, table 2.1 indicates that the DFNOG correction yielded a consistent, albeit small, variability decrease. Figures 2.16a and 2.16b indicate the affected wavelengths as being around 400 km and greater, which is to be expected from the gentle undulations observed in the repeats plotted in figure 2.10. With the exception of repeat 10 however, none of the

variability decreases even approach the noise level, and difference profiles made before and after DFNOC correction showed only the most minor differences - none of which could be mistaken for oceanographic signals. For this reason, unless the subsequent test arcs show otherwise, making the DFNOC correction is deemed not to be worth the effort.

Arc 82 Summary

Based upon statistical and spectral methods, the Solid Tide, Wet FNOC, Wet SMMR, Dry FNOC, and Ionospheric GDR corrections were determined to be unnecessary over the length of the arc. Over a longer arc, such might not be the case, although the methodology presented herein would still be applicable. These judgements were fully corroborated by the difference profiles which showed that the phenomena (at least as modelled for the GDR) could not be mistaken for oceanographic signals.

The Ocean Tide correction had the greatest effect on difference profile variabilities, though the results were not always favorable. Aliasing was suspected and will be treated in more detail later.

The Electromagnetic Bias correction also showed some significant effects on the variability, though the ensemble results indicated the danger of indiscriminantly correcting the data. I examine this in some detail as the next test arc is discussed.

2.5 ARC 209

The mean sea surface height profile along arc 209 is shown in figure 2.2. Representative difference profiles of 5 of the 14 passes used to make this mean are shown in figure 2.17. Again, no corrections (other than spike editing and detrending), were performed to the sea surface heights of these profiles, and a region of high geoid variability was deleted. In passing, note the short-to mid-wavelength features in the southern region of profiles 5, 8, 9, and 10. This region is that of the Musician Seamounts north of Hawaii, and the features were not eradicated by any corrections. Residual geoid contamination may be ruled out because the features are seen to move some 100 km between repeats 8 and 10,

leaving oceanographic signals as a promising source. I refrain from further discussion of oceanography for the present.

Table 2.2 shows the effects of the corrections on the difference profile variabilities for arc 209, and like table 2.1, indicates that the STIDE, WSMMR, and IONO corrections make no real difference (repeat 17 experienced a variability decrease just outside the noise bound after being WSMMR corrected, but this was the only instance of this, and the ensemble statistics are nearly identical with those of no correction). As before, the WFNOC and DFNOC corrections occasionally cause a significant change in variability on a difference profile, but their ensemble statistics continue to differ only slightly from those of the no correction case. Note that the 7.78 cm mean variability after WFNOC correcting is only about a 3% decrease from the no correction figure of 8.04 cm, while the DFNOC correction decreases $\bar{\sigma}$ by less than 1%. Spectral plots and difference profiles concur that none of the above corrections need to be made.

The two corrections which bear further study are OTIDE and EM BIAS. As was seen for arc 82, the former correction has the most significant effect on individual difference profiles; either by increasing or decreasing variability. Spectral plots for arc 209 concur with earlier results showing the OTIDE correction as affecting wavelengths around 300 km and longer. In contrast to earlier, however, observe from table 2.2 how the mean variability is decreased upon OTIDE correcting, now that more repeats are used to form the mean profile. This behavior continues to indicate that the ocean tide is aliased by the 17 day sampling period, which is no surprise. (As a further check, an arc 209 mean was formed by only using 10 repeat cycles. In this case, the mean variability increased by 4% upon OTIDE correcting). These results will be explained in detail in the arc 293 section.

Electromagnetic Bias

Figure 2.18 shows SWH for five representative repeats along arc 209. Repeats 9 and 5 both experienced a significant increase in variability when the EM BIAS correction was made, whereas repeats 10, 3, and 2 had their variability reduced. This figure supports

the same two observations made previously - repeats that have the greatest SWH fare the worst after the EM bias correction, and the areas where SWH is largest also show the greatest noise on the difference profiles. The wavelengths affected most by the EM BIAS correction continue to be around 400 km and longer.

Since the EM BIAS correction can have a significant effect on the alongtrack variability for a given repeat, a better understanding of it is essential. I begin by looking more closely at those repeats where correcting for EM BIAS increased the variability. Note on the difference profiles of repeats 5 and 9 (figure 2.17) that the sea surface height is higher than the mean profile in those areas where SWH is largest. If EM BIAS was the major effect here, one would expect just the opposite. That is, large waves should depress the non-corrected difference profiles below the mean surface. I suspect that the EM BIAS correction failed because the sea surface was actually responding to the larger inverted barometer (IB) effect. To test this assertion, a closer look was taken at the situation in the area at the time of repeat 5, since its SWH plot shows such a prominent feature.

Figure 2.19 is the meteorological surface analysis in the area at 12Z, 22 January 1987; 3 hours prior to repeat 5 on arc 209. The dominant feature is the strong LOW pressure system centered at 50°N, 166°W.* The small triangles indicate its position and strength at 12 and 18 hrs prior to 12Z. The large values of SWH on repeat 5 from around 38°-49°N seen on figure 2.18 may be corroborated by the isobaric spacing along the arc. Observe how the isobars are closest together in the same latitude range, indicating the highest winds which would give rise to the largest waves. If the SWH profile for repeat 5 thus looks appropriate, then why didn't the EM BIAS correction work? The answer lies in the pressure field. As one approaches the center of the LOW while travelling on the arc, the sea surface will rise according to the IB effect. From the surface analysis, this effect

* The LOW can also be seen in a plot (not pictured) of the DFNOG correction, which reduced the RMS variability of the repeat 5 difference profile by 7.4%, when applied (see table 2.2).

should be a maximum at around 49°N , which is what the difference profile indicates. If one considered only EM BIAS, one would expect the uncorrected sea surface to be at its lowest where SWH is highest - near 47°N in this case. The fact that this is not seen is because the IB effect is of opposite sign and greater magnitude than EM bias. Thus the sea surface, to lowest order, follows the IB effect and EM BIAS is not appropriate. (In this case, the maximum IB effect is $1013 \text{ mb} - 972 \text{ mb} = 41 \text{ cm}$ to be subtracted, and the maximum EM BIAS is $1200 \text{ cm} \times .02 = 24 \text{ cm}$ to be added. I do not recommend making the two corrections jointly, as will be discussed shortly).

A point by point inverted barometer correction was calculated by first recovering sea level pressure from the GDR DFNOG correction and then using the 1.01 cm/mbar relation mentioned earlier. The results of this correction, as applied to arc 209, appear in the rightmost column of table 2.2. Prior to examining the results in this column, it is important to recall a point made in Chapter 1; namely, that care must be taken in investigating the IB effect due to its close connection with the Dry Troposphere correction. This can be seen in the following way: if the Dry Troposphere correction is made to the sea surface heights before making the IB correction, and the Dry Troposphere correction is not perfect; it will introduce a false pressure signal into the sea surface heights. Since this same pressure signal is used to compute the IB correction, there will be a false coherence between the observed profile and the modelled IB correction - manifested by a change in the Φ_{0x} term in equation (4). This may invalidate the results of (5) and (6), making determination of the success of the IB correction very difficult. To avoid this problem here and throughout, all corrections were investigated individually.

In the case of repeat 5, the IB correction significantly decreased variability, by some 26%. One can see from the plot of the repeat 5 difference profile after correcting for IB (top of figure 2.20), that this variability decrease was indeed a result of taking out the gentle rise in the sea surface due to the LOW. Such a simple correction does not always bring success, however. In the case of repeat 10, variability was increased by 40% after

IB correcting. From the repeat 10 difference profile after correcting for IB (middle of figure 2.20), note that the IB correction added a convex signature centered around 36°N. Figure 2.21, a diagram of surface analysis 3 hours prior to overflight, shows this to be a consequence of the HIGH pressure system located there. The problem is that the uncorrected difference profile for repeat 10 shown in figure 2.17 is basically flat in this region - indicating that the sea surface did not respond in an IB sense to the HIGH, and that a correction is therefore inappropriate. Why the difference between repeats 5 and 10?

As alluded to earlier, the IB effect is a function of the time and space scales of the forcing from the surface pressure field. Looking at the spatial scales of the LOW and HIGH, it is apparent that the HIGH has a much larger spatial scale than the LOW. I assert that the LOW is small enough for long gravity waves to quickly communicate its presence throughout the affected ocean area, resulting in a largely static IB response. This communication is not possible over the much larger HIGH, and so oceanic response is more dynamic in nature in this case. This prevents the simple IB correction from working well for repeat 10. This can be quantified using the result of Wunsch (1972) that the Rossby radius of deformation is the upper spatial limit of an expected static IB response. The Rossby radius of deformation is defined by the ratio of the wave speed to the Coriolis parameter, and may be thought of in this context as the shortest spatial scale at which the geostrophic balance may occur. Long deep water waves travel at an approximate speed of $(gh)^{1/2}$, where g is the gravitational acceleration and h is the water depth (about 5500 m under arc 209). The Coriolis parameter at mid latitudes is about 10^{-4} s^{-1} , giving an approximate barotropic Rossby radius of 2300 km for the region in question. Spatial scales for the LOW and HIGH may be estimated from the diameter of the largest closed (and reasonably symmetric) isobar, giving 1100 km and 2500 km respectively. The LOW forces the sea surface on a scale less than the Rossby radius, and so an inverted barometer response is possible. The forcing scale of the HIGH exceeds the Rossby radius and so the

pressure gradients tend to be supported by geostrophic currents - preventing a static IB response.

Another scenario which may be envisioned relates to the time scale of the IB response. Suppose that a pressure system with a spatial scale otherwise conducive to a static IB response rapidly approaches a groundtrack in the hours/days preceding overflight, being quite close to that arc at the time of overflight. The pressure field at overflight from which the IB correction is calculated will thus result in a large calculated correction, whereas the true IB response will be small, since the ocean hasn't yet had time to respond to the changing surface pressure. A similar outcome may result from a system which rapidly strengthens prior to overflight. I believe a combination of these effects accounts for the variability increase upon IB correcting repeat 8. As can be seen in figure 2.22, a strengthening LOW approached from the Southwest prior to the repeat. The IB correction assumed that the sea surface had statically responded to the alongtrack pressure profile at the time of overflight and thus depressed the sea surface in the northern region to compensate for the LOW (compare figures 2.17 and 2.20). In reality, though, figure 2.17 shows that the sea surface had not risen in response to the LOW, and thus the IB correction was inappropriate. (Note that the surface analysis for repeat 5 in figure 2.19 was for 3 hours prior to overflight, giving the ocean more time to respond in that instance and resulting in a smaller calculated IB correction, since the LOW's center would have been further from the arc. These factors, in addition to the relatively constant strength of the LOW in that case could explain why the IB correction worked well for repeat 5 and not for repeat 8).

Overall, the application of the pressure-derived IB correction to arc 209 resulted in a mean variability increase of about 4%. As just alluded to, the inefficacy of this correction over the ensemble of passes is due to the fact that the ocean's response to surface forcing is a complicated function of the forcing scales and not just a simple reflection of the alongtrack pressure profile at overflight. For this reason, I recommend not making the

inverted barometer correction, at least in its simplest form, to the GEOSAT sea surface heights. A better approach would be to determine a frequency/wavenumber dependent correction.

Returning to EM BIAS, note that its "failure" in regions where SWH was greatest has been shown, in the instances studied, to have been the result of being overpowered by the IB effect (other cases like repeat 9, and repeat 4 of arc 82, were also investigated, with similar results). Because the latter effect is so difficult to predict in a simple fashion, neither can one say, a priori, when the EM BIAS correction will be desirable. Since the indiscriminate application of this correction, as showed by table 2.2, can result in a mean variability increase, it is also recommended that the EM BIAS correction not be made.

Arc 209 Summary

Based on the first two test arcs, all corrections except OTIDE are deemed unnecessary or undesirable. The OTIDE correction is examined in detail in the following section, wherein final judgement on all corrections is also made.

2.6 ARC 293

The mean profile for arc 293 is shown in figure 2.3. The first five difference profiles of the 18 repeats used to form that mean are shown in figure 2.23. Geoid contamination was not enough of a problem to warrant the deletion of any areas.

Table 2.3 presents the results of applying the various corrections to arc 293. It is immediately apparent that the IONO correction is again insignificant, both from individual repeats and ensemble results. Four other corrections are also seen to be unnecessary, based on ensemble results. These are STIDE, WFNOG, WSMMR, and DFNOG. While these corrections did affect some individual difference profiles beyond the noise bounds; it was never by much, was often harmful to the variability, and always involved repeats that had a large variability before correcting. Such repeats have narrower noise bounds than those which have small variability before correcting, meaning that more correction results will be tagged as being significant purely as a matter of course. The EM BIAS correction is

not listed because it was compared to a mean profile formed from only 14 repeats (due to data problems in the SWH channel). It continued to behave as before, however, having significant effect on several difference profiles; but doing poorly over the ensemble. Such was also the case with the IB correction, as shown by table 2.3.

Thus far, the results of arc 293 completely support the earlier assertions that all corrections except OTIDE are either unnecessary or undesirable. Though not included as figures, numerous spectra and difference profiles before and after correcting corroborate these findings.

Ocean Tide

Table 2.3 shows that the OTIDE correction significantly reduced the ensemble mean variability and standard deviation, as well as having a good deal of effect on the individual difference profiles. Note from figure 2.23 how the first five difference profiles look before OTIDE correcting. Significant long wavelength variations are evident in repeats 1, 2, and 3, which account for the high variability seen in table 2.3. Now observe figure 2.24 and note how these variations largely match the ocean tide signals alongtrack. After the OTIDE correction was made, figure 2.25 shows the long wavelength signals were greatly reduced, as was the variability in table 2.3. Spectral analysis concurred with earlier estimates of wavelengths ≥ 300 km being affected by the correction.

From the results of this arc, the OTIDE correction looks like a desirable one. Before making a final judgement though, I seek an understanding of why the OTIDE correction increases variability in some repeats, and why the ensemble results for arcs 82 and 209 were not nearly so positive. The answer is due to the aliasing of the ocean tide introduced by the way GEOSAT samples the ocean.

GEOSAT passes over a given arc every 17.05 days, so employing the collinear method to produce an arc mean profile entails using snapshots of the ocean surface at widely spaced time intervals. If some non-random signal affects the surface and does not change appreciably from one repeat to the next, it will be aliased into the mean profile. To

understand exactly how this aliasing affects the ocean tide, it is necessary to take a closer look at GEOSAT's orbit.

Following Parke et al. (1987), the earth's equatorial bulge causes GEOSAT's orbital plane to precess at a relatively slow rate Ω , given by

$$\Omega = -\frac{3}{2} J_2 \left(\frac{\mu_E}{a^3} \right)^{1/2} \left[\frac{R_E}{a(1-e^2)} \right]^2 \cos i \quad (\text{s}^{-1}) \quad (7)$$

where i is satellite inclination, \bar{a} is the mean semimajor orbit axis, \bar{e} is the mean orbital eccentricity, μ_E is the gravitational constant times the earth's mass, J_2 is the second zonal harmonic of the earth's gravity field, and R_E is the earth's equatorial radius. The sign convention is that Ω is positive for a retrograde orbit such as GEOSAT's. As mentioned in the previous chapter, \bar{e} for GEOSAT is only 0.0008, allowing (7) to be simplified as

$$\Omega = -4.17 \times 10^{-7} \bar{a}^{-7/2} \cos i \quad (\text{s}^{-1}) \quad (8)$$

where \bar{a} is in km. For GEOSAT, with $i \simeq 108.04$ (varying periodically), and $\bar{a} = 7167.4$ km, (8) gives $\Omega = 4.144 \times 10^{-7} \text{ s}^{-1}$ as the precession rate of the GEOSAT ascending node (GEOSAT orbital values from Born et al., 1987).

GEOSAT completes 244 revolutions in 17 days, where in this context, a day is the time it takes the earth to rotate 360° with respect to the GEOSAT ascending node. The conversion between this nodal time and actual clock time is given by

$$t_{\text{clock}} = \frac{2\pi}{\omega - \Omega} t_{\text{nodal}} \quad (9)$$

where ω is the earth's sidereal rotation rate of $7.292115 \times 10^{-5} \text{ s}^{-1}$. Thus, the actual repeat period P is slightly longer than 17 days by the conversion factor, giving $P = 1,473,162.2$ sec (= 17.05 days or 409.211722 hrs).

The principal alias period of any tidal component may be obtained from the change of phase of that component over the repeat period. The phase change of a tidal component of period T over the repeat period is just

$$\Delta\phi = \frac{2\pi P}{T} \quad (-\pi \text{ to } \pi) \quad (10)$$

and the resulting principal alias period τ is

$$\tau = \text{abs}\left(\frac{2\pi P}{\Delta\phi}\right) \quad (11)$$

again, following Parke et al. (1987).

A sample calculation for the M2 tidal component's principal alias period will illustrate the use of (10) and (11): The M2 tide has a period of $T = 12.420601$ hrs, and using $P = 409.211722$ hrs, equation (10) gives $\Delta\phi = 207.0071392$. This $\Delta\phi$ actually includes a number of complete cycles, so to find the $-\pi$ to π phase change, one subtracts from it the nearest integral multiple of 2π (in this case, $2\pi \times 33 = 207.3451152$). This gives $\Delta\phi_{M2} = -0.337976$ and indicates that between any two "snapshots" of an arc, taken 17.05 days apart; the M2 tide will have cycled nearly 33 times. In fact, it will have cycled so close to 33 times exactly, that its apparent phase change $\Delta\phi_{M2}$ will be extremely small. Plugging the value of $\Delta\phi_{M2}$ into (11) gives an alias period of $\tau_{M2} = 7607.5$ hrs or 316.98 days. Thus, the small apparent change in the M2 tide over a repeat period means that the satellite must sample the arc more than 18 such periods to see the M2 tide complete one apparent cycle. This is a serious alias, especially since M2 is by far the largest tidal constituent. Table 2.4 lists the results of alias calculations for M2 and the next three largest constituents.

The aliasing of the ocean tide is readily seen in figure 2.24, as the OTIDE profiles vary slowly from one repeat to the next. Aliasing is not a problem for arc 293 however, as its mean profile was formed over a 306 day span (18 repeats), and so sampled nearly all possible tidal profiles. Contrast this with the arc 82 and arc 209 means - formed from 10

and 14 repeats, respectively. I would expect arc 82 to be the most seriously aliased, followed by arc 209 with minor aliasing. This assertion is supported by the results shown previously. The ensemble mean variability suffered the most upon OTIDE correction on arc 82, rising some 5%. It fared better on arc 209, falling by 1%; and did best on the non-aliased arc 293, falling by 32%. A discussion of the mechanisms by which this happened follows.

Equation (4) showed the relationship in the Fourier domain between the observed difference profile, a modelled phenomenon, and the desired profile after the phenomenon was removed. It is written again here for reference:

$$\Phi_{dd} = \Phi_{oo} - 2\text{Re}[\Phi_{ox}] + \Phi_{xx} \quad (4)$$

Now the observed profile is actually computed from each observed repeat profile r , minus the mean profile m . Thus $o=r-m$, and the first two terms on the right hand side expand to

$$\begin{aligned} \Phi_{oo} &= \langle (\hat{r} - \hat{m})(\hat{r} - \hat{m})^* \rangle \\ &= \Phi_{rr} - 2\text{Re}[\Phi_{rm}] + \Phi_{mm} \end{aligned} \quad (12)$$

and

$$\begin{aligned} \Phi_{ox} &= \langle (\hat{r} - \hat{m})\hat{x}^* \rangle \\ &= \Phi_{rx} - \Phi_{mx} \end{aligned} \quad (13)$$

allowing (4) to be rewritten as

$$\Phi_{dd} = \Phi_{rr} + \Phi_{mm} + \Phi_{xx} - 2\text{Re}[\Phi_{rm} + \Phi_{rx} - \Phi_{mx}] \quad (14)$$

where the subscripts d, r, m , and x respectively denote the desired difference profile after correcting for the phenomenon, the observed repeat profile, the mean profile, and the modelled correction for the repeat. The Φ with repeated subscripts are power spectra and Φ with different subscripts are cross power spectra.

If the phenomenon being modelled is essentially random over the length of time used to form the mean profile, then that mean will be uncorrelated with the phenomenon on

any given repeat, meaning that $\Phi_{mx} \approx 0$. Similarly, the mean will also be uncorrelated with each repeat profile, giving $\Phi_{rm} \approx 0$.^{*} From (12) and (13), one sees in this case that $\Phi_{rr} + \Phi_{mm} \approx \Phi_{oo}$ and $\Phi_{rx} \approx \Phi_{ox}$. Thus, when the phenomenon is random, the full expression (14) reduces back to (4), which was the special case derived earlier.

The full form of (14) is the key to understanding the statistical behavior of the ocean tide correction over the three test arcs. Arc 293's mean was formed from repeats which represented a full set of ocean tide phases (summing to 2π), and so would be uncorrelated with any repeat profile or its modelled tide. Thus $\Phi_{rm} \approx 0$ and $\Phi_{mx} \approx 0$, allowing this arc to be described by the random phenomenon equation (4). As derived before, the accuracy of the phenomenon model may be easily evaluated in this case by observing the effect that the correction has on the RMS variability of each repeat's difference profile. Since the mean variability $\bar{\sigma}$ fell substantially after applying the OTIDE correction to the passes on arc 293, it can be concluded that the tidal model is a good one, at least in the vicinity of that arc.

The other two arcs had means formed from partial sets of possible tidal phases, with the most common phase thus aliasing into the mean profile. From (14), it is apparent that the RMS variability calculations are now a function of the aliasing as well as the model accuracy, and several options are possible. The simplest is the utilization of a near-perfect tidal model. In this case, the model completely removes the tide from each repeat used to form the mean profile, and so the mean will be uncorrelated with any observed repeat profile or its modelled tide. That is, $\Phi_{rm} \approx 0$ and $\Phi_{mx} \approx 0$. The observed repeat profiles will be highly correlated with the modelled phenomenon, and so $\Phi_{rx} \approx \Phi_{xx}$. Using these results, and the relations in (12) and (13), equation (14) reduces to $\Phi_{dd} \approx \Phi_{oo} - \Phi_{xx}$; the

^{*} Actually, the mean is always correlated with each repeat to some extent, due to the mean sea surface topography. This natural correlation is ignored here, since it is independent of the phenomenon being investigated.

random case with excellent modelling, derived before. This result indicates that, if the tide model is good enough, aliasing is not a factor.

The statistical results from arc 293 indicate that, while the ocean tide model is a good one, it is not nearly perfect (as seen in the variability increases of some repeats after correcting for OTIDE). Considering (14) with this knowledge, two limiting cases apply in the study of the statistical behavior of arcs 82 and 209. The first is for a repeat having a tidal phase similar to the one aliased into the mean. In this case, the repeat profile and its modelled tide will both be positively correlated with the mean; $\Phi_{rm} > 0$ and $\Phi_{mx} > 0$. Since the model is a good one, once again $\Phi_{rx} \approx \Phi_{xx}$. Thus (14) may be rewritten as

$$\Phi_{dd} \approx \Phi_{rr} + \Phi_{mm} - 2\text{Re}[\Phi_{rm}] - \Phi_{xx} + 2\text{Re}[\Phi_{mx}] \quad (15)$$

where all Φ are positive. The power spectrum of the observed (i.e., non-corrected) difference profile, as shown in (12), is just the first three terms on the right hand side of (15), where the amount of aliasing determines Φ_{rm} . If the repeat has a tide very similar to the one aliased into the mean, Φ_{rm} will approach Φ_{mm} , giving $\Phi_{oo} \approx \Phi_{rr} - \Phi_{mm}$ and the uncorrected difference profile will have low power and variability. This explains what happened with repeats 1-3 on arc 82, for example, as that arc's mean was formed from a number of early repeats with tidal phases similar to theirs. Note in table 2.1 the low RMS variability of these repeats before correcting for ocean tide, as expected. This behavior is more difficult to spot in the arc 209 repeats, as that mean was aliased to a lesser extent than arc 82's. Nevertheless table 2.2 indicates that repeats 8, 10, and 13 on arc 209 may have had their tides aliased into the mean.

The effect of the modelled correction in the first limiting case is described by the last two terms in (15). The familiar Φ_{xx} term indicates the usual tendency of a well-modelled correction to reduce the variance. The new Φ_{mx} term, however, indicates that even a well modelled correction will increase the variance of the difference profile to which it is applied, if it has been aliased into the mean profile. The balance between Φ_{xx} and $2\text{Re}[\Phi_{mx}]$ determines whether there will be a variability increase or decrease upon making

the correction. If the repeat tide highly resembles the one aliased into the mean, then Φ_{mx} will approach Φ_{xx} , and the variability will increase. The highly aliased first three repeats on arc 82 again illustrate this result, as may be seen in table 2.1. When the OTIDE correction is made to them, their RMS variability increases. Repeats 8, 10, and 13 on arc 209 also show this behavior, as indicated in table 2.2.

The second limiting case to (14) is for a repeat having a tidal phase very dissimilar to the one aliased into the mean. In this case (assuming the model is good), the repeat profile and its modelled tide will be highly correlated with each other but not with the mean; or $\Phi_{rx} \approx \Phi_{xx}$, $\Phi_{rm} \approx 0$, and $\Phi_{mx} \approx 0$. Then (14) becomes

$$\Phi_{dd} \approx \Phi_{rr} + \Phi_{mm} - \Phi_{xx} \quad (16)$$

where from (12) the first two terms on the right hand side describe the power spectrum of the non-corrected difference profile (Φ_{oo}), and the last term indicates the effect of making the correction. As opposed to the case where the repeat tide was highly aliased and $\Phi_{oo} \approx \Phi_{rr} - \Phi_{mm}$; here the power of the uncorrected difference profile is given by $\Phi_{oo} \approx \Phi_{rr} + \Phi_{mm}$. Thus the RMS variability of a non-aliased repeat will tend to be larger than that of an aliased repeat before correcting for ocean tide. Note also from (16) how, in this case, there is no aliasing term involving the correction. This indicates that for a repeat whose tidal phase has not been aliased into the mean, variability will tend to decrease upon making the correction.

These results are clearly demonstrated by repeat 10 on arc 82. Note from figure 2.8 how the tidal phase of this repeat is clearly different from the phase of the early repeats which was aliased into the arc 82 mean. One would thus expect from (16) that this repeat should have high RMS variability before making the OTIDE correction, which will be reduced upon making the correction. The results listed in table 2.1 verify this. Such

behavior is also seen in repeat 17 on arc 209, which has the unique tidal phase of all the repeats used to form the arc 209 mean.*

When the mean profile of an arc is highly aliased; by definition a majority of its repeats will have tidal phases similar to the one aliased into it. Thus, most repeats will also experience a variability increase upon making the OTIDE correction, and the mean variability over the ensemble of repeats ($\bar{\sigma}$) will rise. This explains the behavior of $\bar{\sigma}$ for arc 82. The mean of arc 293 was not aliased, and so the accuracy of the tidal model caused $\bar{\sigma}$ to drop substantially when the OTIDE correction was performed. Arc 209 falls in between the two extremes, as does the behavior of its $\bar{\sigma}$.

The behavior of the sample standard deviation (SSD) can also be explained from the results of this subsection. In the case of a non-aliased mean, the OTIDE correction is merely reducing a major source of oceanic variability. The difference profiles with the tide removed will thus look more alike, and so the standard deviation of the individual repeat variabilities about $\bar{\sigma}$ will be less. With the aliased means, SSD will still tend to drop for a well modelled correction. This drop occurs because the aliased repeats with initially low variability will experience a variability rise upon correcting for OTIDE; and the non-aliased repeats with initially high variability will tend to experience a variability decrease upon OTIDE correction. The spread in variabilities between repeats is thus lessened, and so is the SSD. The data for arcs 82 and 293 behave in just this way, as seen in tables 2.1 and 2.3. Arc 209 experiences a slight rise in SSD after making the OTIDE correction, which may indicate that the tidal model is not quite as good along arc 209 as it is for the other

* There is a simple way of estimating which repeats will be the most (and least) aliased into the mean: Draw a circle and divide it into 18 equal slices. The slices represent the full set of tidal phases sampled over the M2 alias period. Then, for each repeat used to form the mean profile, color in its appropriate slice. From the resultant picture; those colored repeats which appear in bunches are the most likely to be aliased into the mean. Those colored slices which are isolated on the phase circle indicate repeats having tidal phases which are probably different from the aliased phase. Estimates of the behavior of the repeats on the aliased test arcs using this method correspond fairly well with the actual results.

arcs. This result is not surprising as arc 209 passes through the Aleutian Island chain; which is a difficult area to model.

Test Arc Summary

The results of applying the GEOSAT GDR corrections to the three test arcs may be summarized as follows: Of all the phenomena which are modelled in the GDR, only the ocean tide, electromagnetic bias and inverted barometer corrections vary enough over the length of the arcs to have a significant effect on the difference profiles when applied (actual effects such as the true wet troposphere correction may also be significant, but are not currently modelled well enough to reflect it). Out of these three effects, only the ocean tide is modelled accurately enough to allow consistent reduction in the variability which it produces in the sea surface. The ocean tide, however, may be significantly aliased into the mean profiles formed by the collinear method; resulting in erroneous variability in the difference profiles.* The following recommendations are therefore made for editing GEOSAT data in the test region:

- 1) Apply only the GDR OTIDE correction to the sea surface heights.
- 2) For each arc, use an ensemble of OTIDE-corrected repeats that will prevent the ocean tide from aliasing into the mean sea surface height profile..

When only a limited number of repeats are available (due to data dropouts, for example), the latter recommendation may be achieved by ensuring that the repeats used are evenly spaced around the phase circle discussed earlier. If data dropouts are not an issue, the best mean profiles will be formed from repeat cycles spanning some integral multiple of the M2 alias period (~18 repeat cycles); though as more repeats are used, aliasing will become less of a problem as a matter of course.

* There is nothing to prevent the other corrections from aliasing into the means either, though their random nature would result in more broadband contamination of the mean profiles. In any case, the generally low variability of most of the non-OTIDE corrections would preclude their possible aliasing from being much of a problem.

2.7 SUCCESSIVE POINT AVERAGING

The final evaluation of the GDR concerned the possibility of successive - point averaging the sea surface heights to reduce noise and computer storage space. The benefits of the latter are obvious, and the former was deemed desirable due to the short wavelength jitter seen in most of the difference profiles. The algorithm of choice was a three point block (e.g. - not running) average of the sea surface heights on each pass. This algorithm was chosen mainly for ease of computation, as the average sea surface height of three consecutive data points could be assigned in time and space to the central point.

Before including the block average in the collinear algorithm (between spike removal and detrending), spectral methods were employed to determine its effect on the difference profiles. The power spectra of the eighteen OTIDE corrected difference profiles on arc 293 were averaged together to form an arc spectrum with 144 degrees of freedom. This spectrum is shown in figure 2.26. Aside from the peak at a wavelength of 130 km, note how the power falls off between k^{-1} and k^{-2} (where k is the wavenumber) down to wavelengths of about 100 km, and then levels off. Now, the three point block average results in an increased sampling interval of 3Δ or 20 km; meaning that signals of $\lambda \leq 40$ km will be unresolvable and possibly aliased. Remembering that the power is plotted on a logarithmic scale, however, figure 2.26 shows that there is minimal variance in the wavelengths shorter than 40 km. Thus, little information about ocean variability is missed at these scales, and the averaging is acceptable. Additionally, the mesoscale features of interest have typical spatial scales of 100+ km, which the block average will not obscure. The spectral peak at 130 km is due to geoid contamination, as will be shown in Section 3.2.

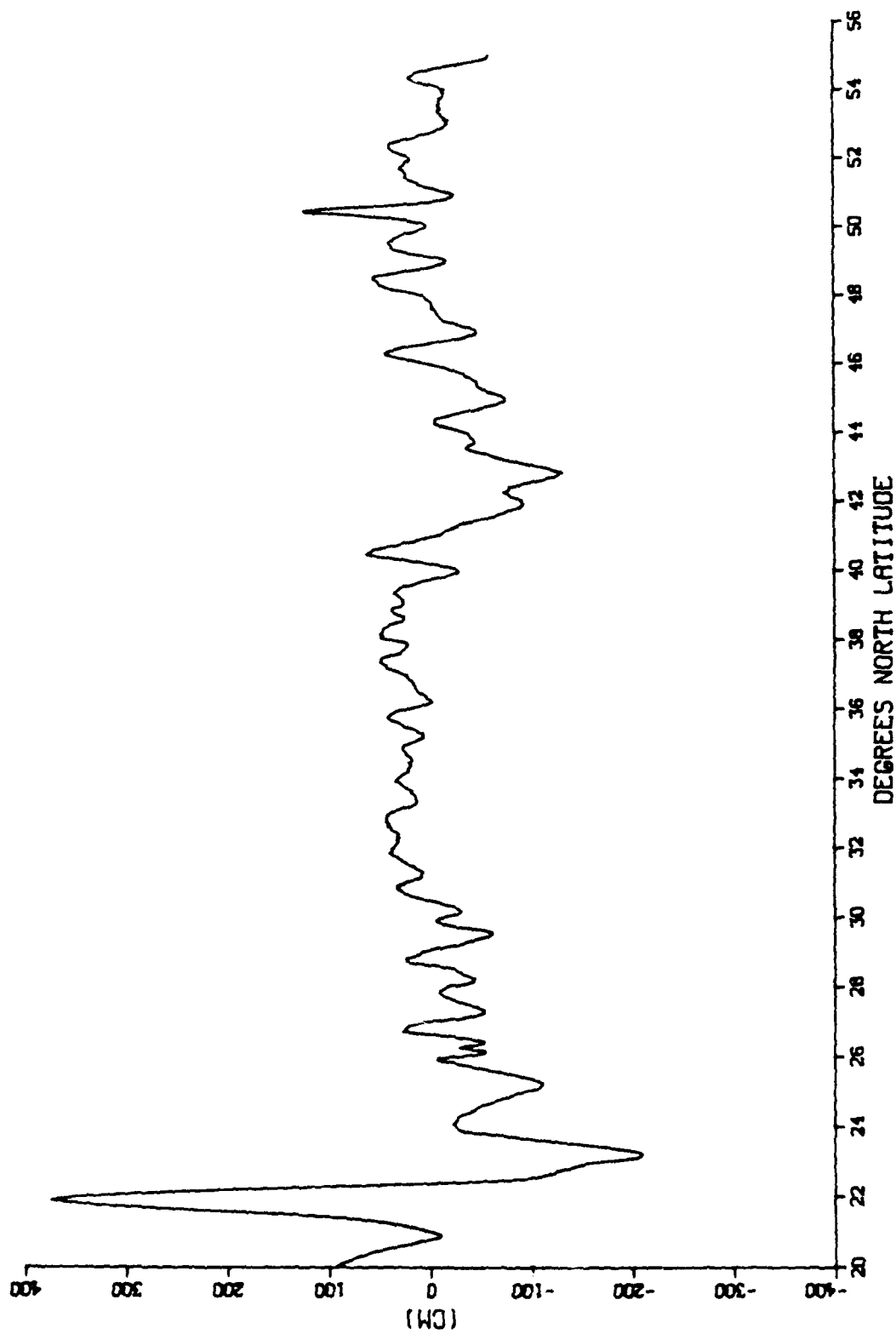


Fig. 2.1 Mean sea surface height profile along arc 82. No corrections applied. The large features near 22°N are due to the high spatial variability of the geoid near Hawaii.

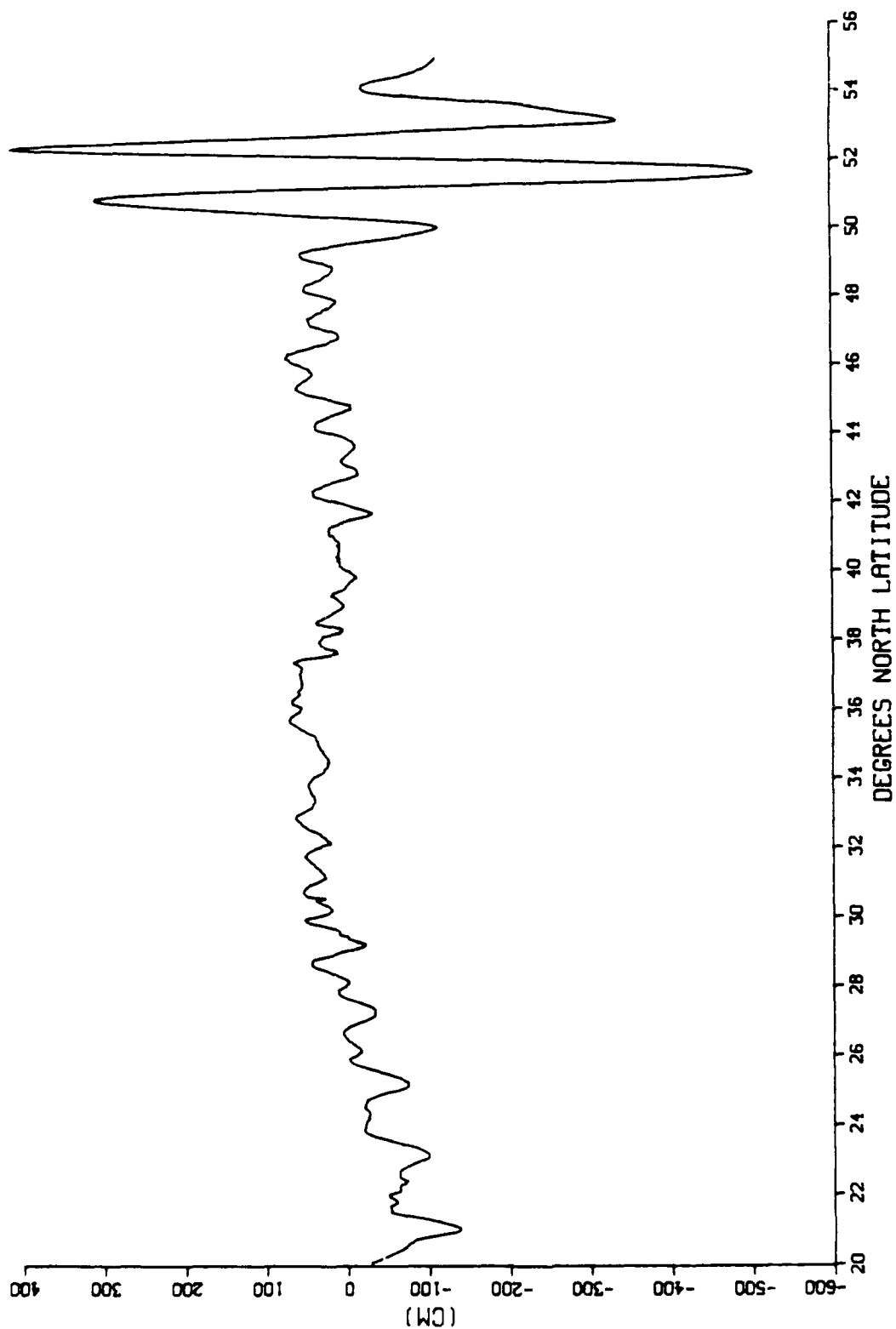


Fig. 2.2 Mean sea surface height profile along arc 209. No corrections applied. The large features north of 49°N are due to the high spatial variability of the geoid through the Aleutian arc.

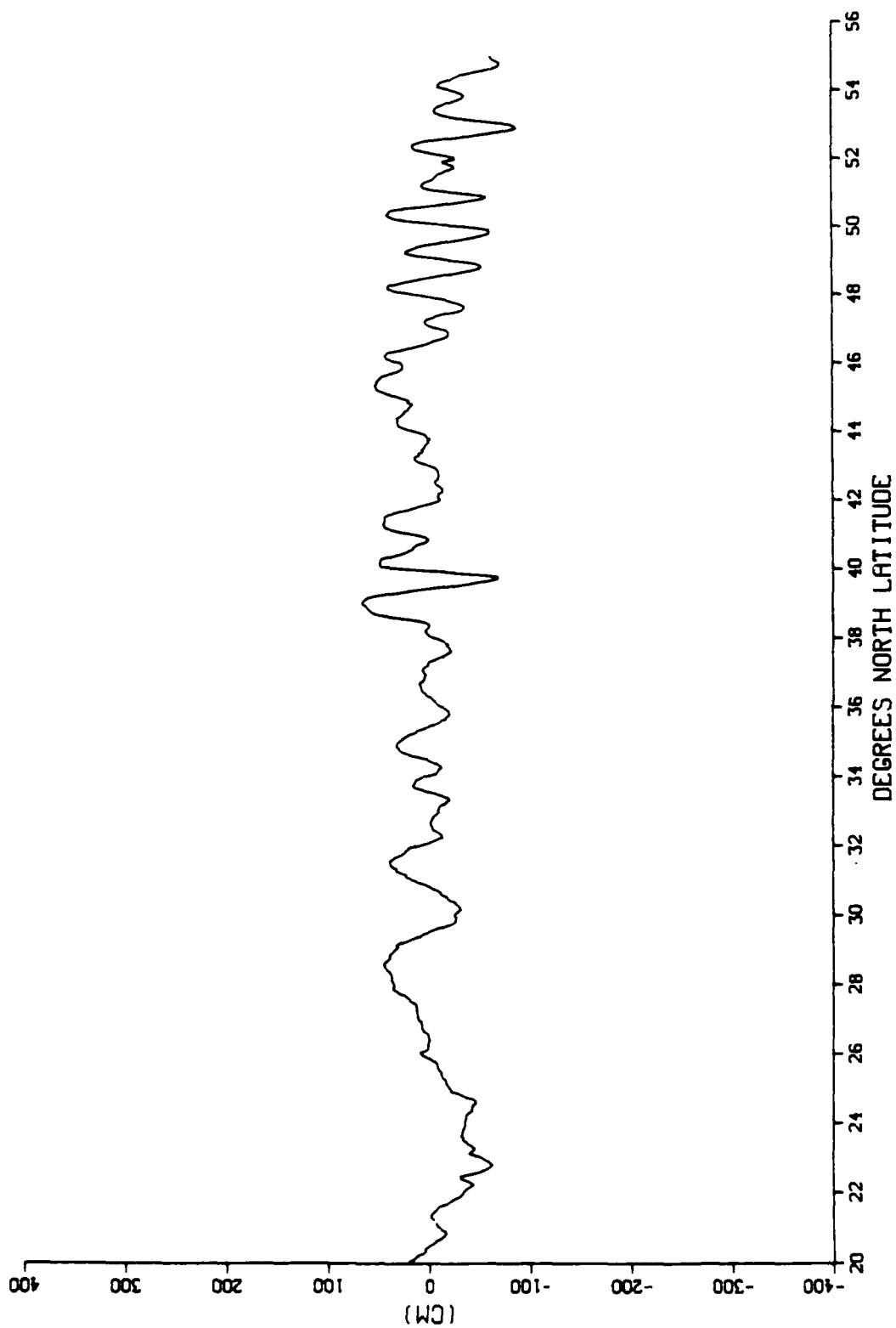


Fig. 2.3 Mean sea surface height profile along arc 293. No corrections applied.

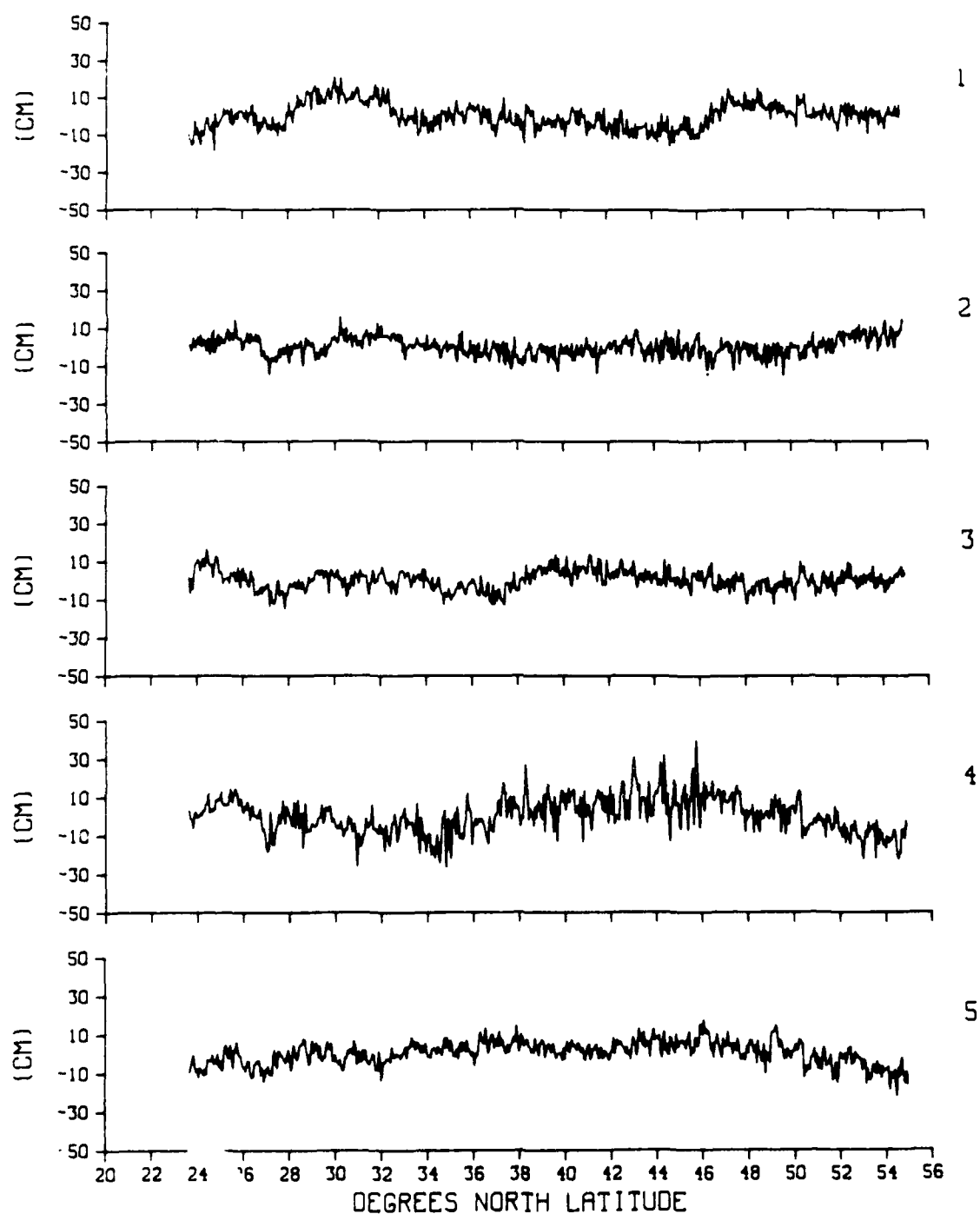


Fig. 2.4 Difference profiles along arc 82. No corrections applied. The repeat numbers appear at the right of each profile.

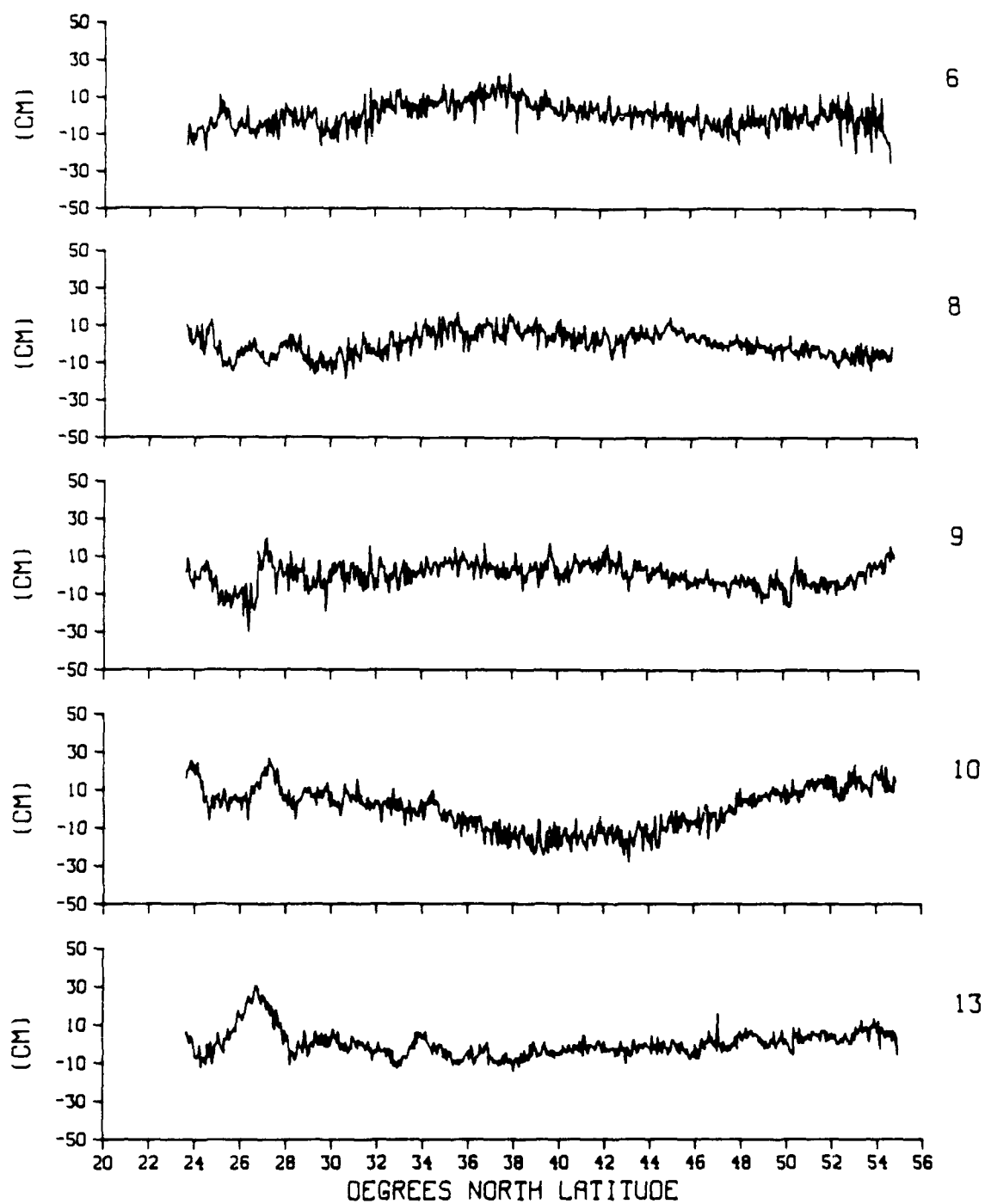


Fig. 2.5 Difference profiles along arc 82. No corrections applied.

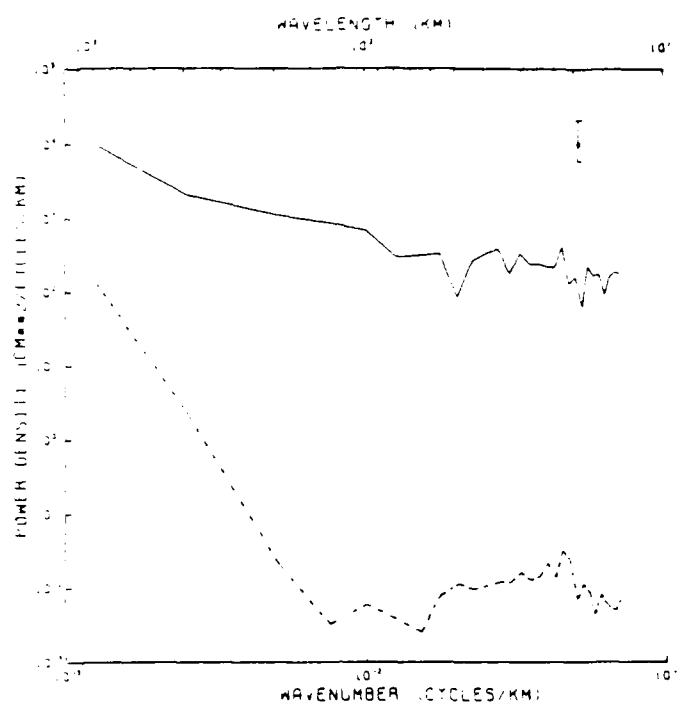


Fig. 2.6a Power spectra of the difference profile (solid line) and solid tide correction (dashed line) for repeat 9 on arc 82. The 95% confidence limits appear at the upper right.

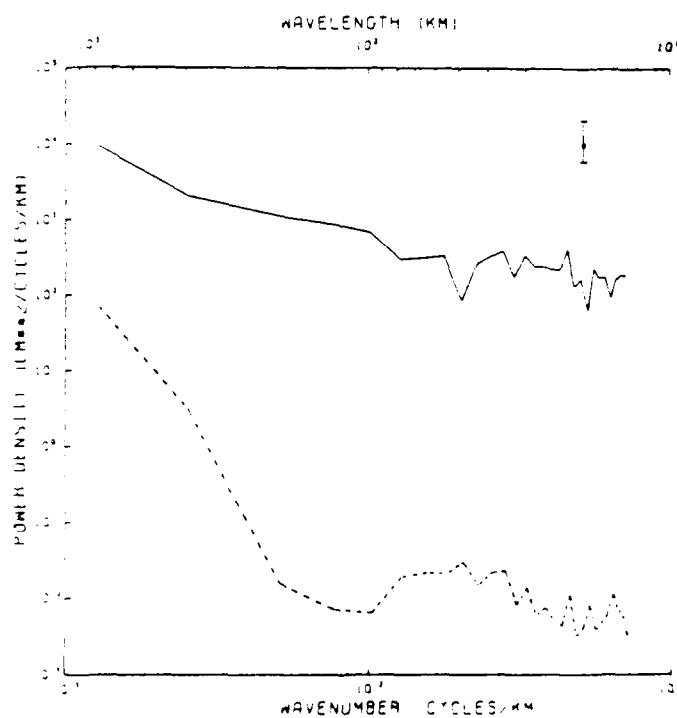


Fig. 2.6b Power spectra of the difference profile (solid line) and wet SMMR correction (dashed line) for repeat 9 on arc 82.

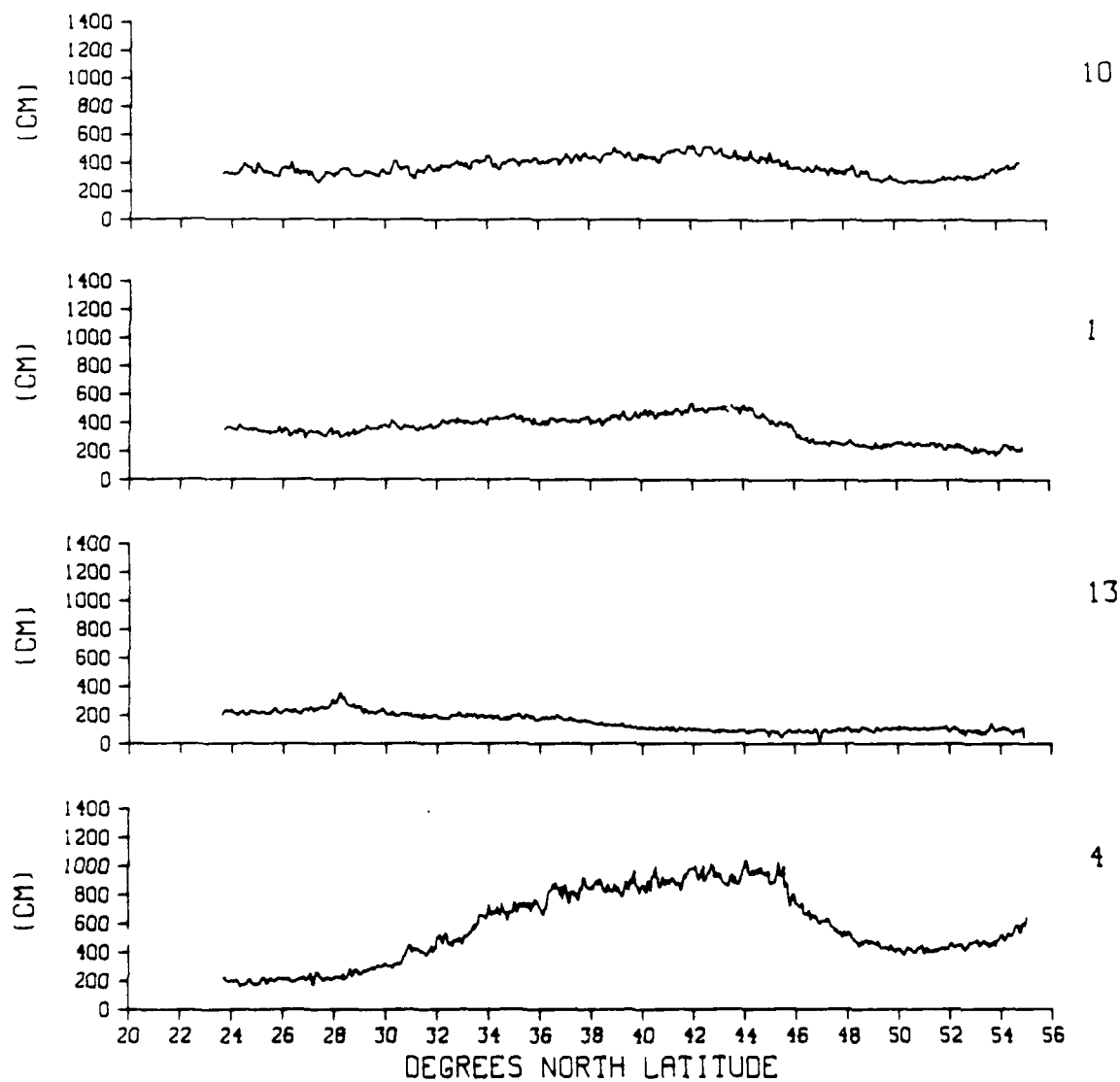


Fig. 2.7 Significant wave height along arc 82. Repeats whose difference profiles experienced a significant variability decrease upon making the SWH-derived EM BIAS correction appear at the top. Repeats which experienced a significant variability increase appear at the bottom.

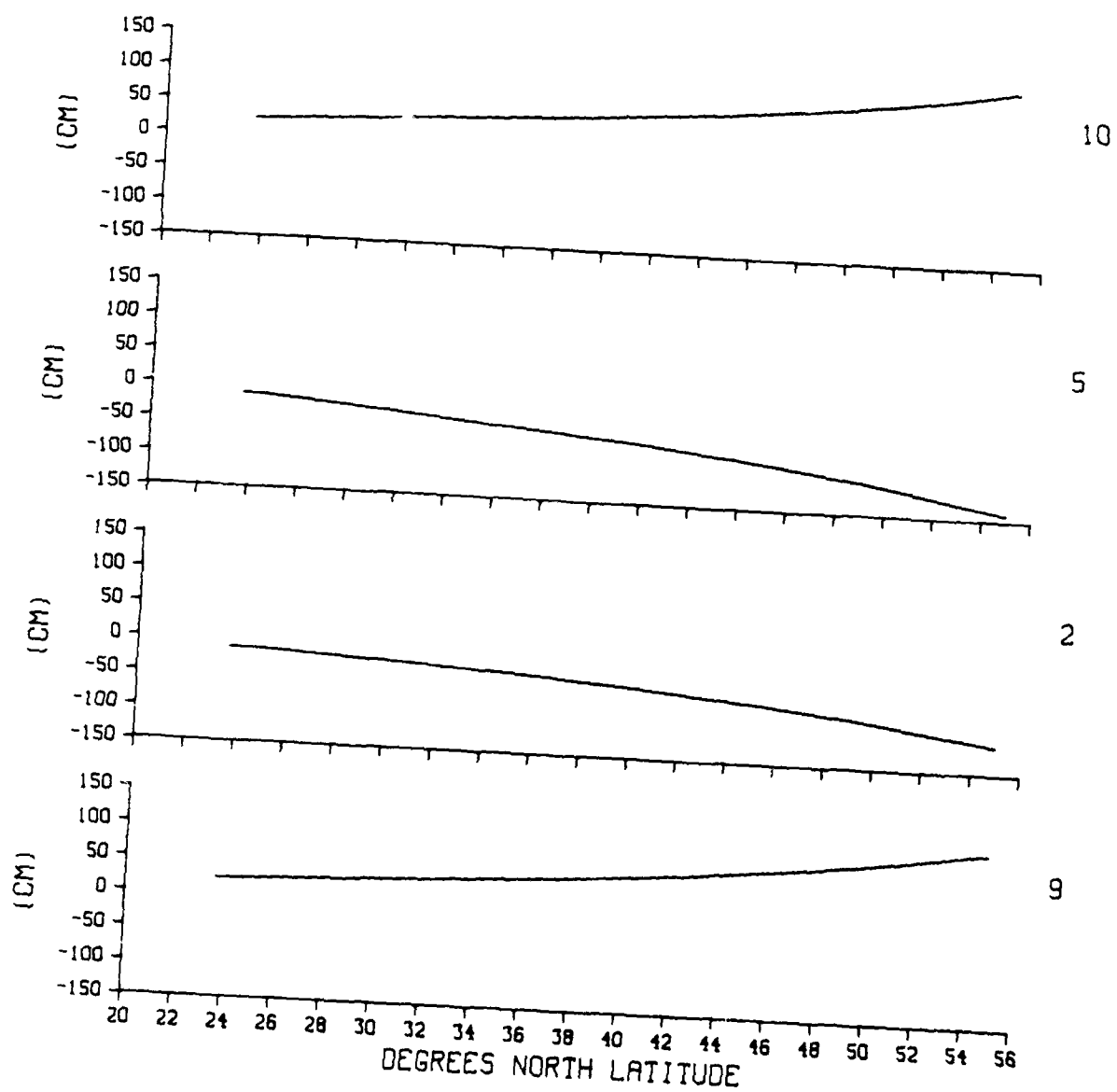


Fig. 2.8 Ocean tide correction along arc 82.

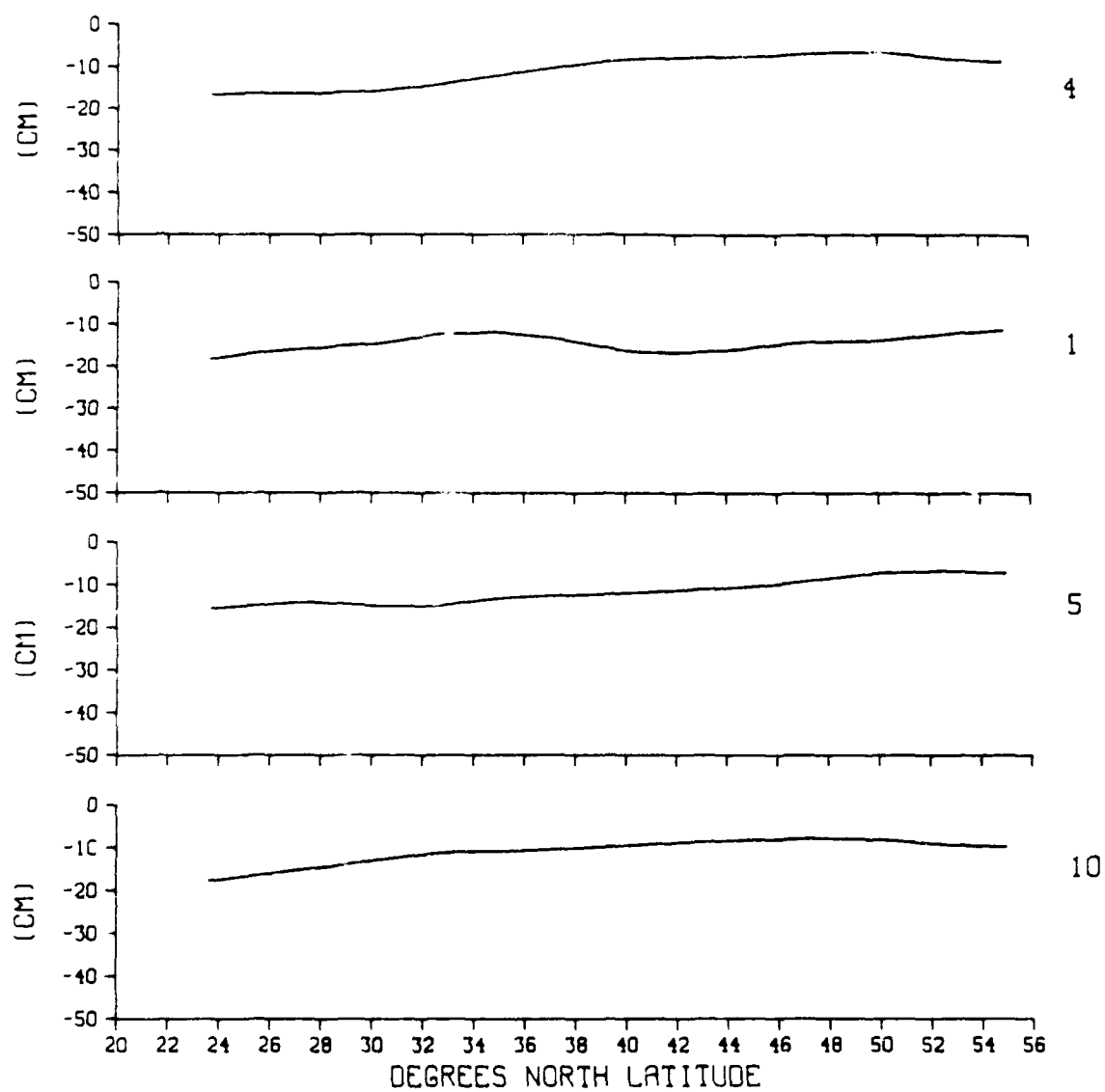


Fig. 2.9 Wet FNOC correction along arc 82.

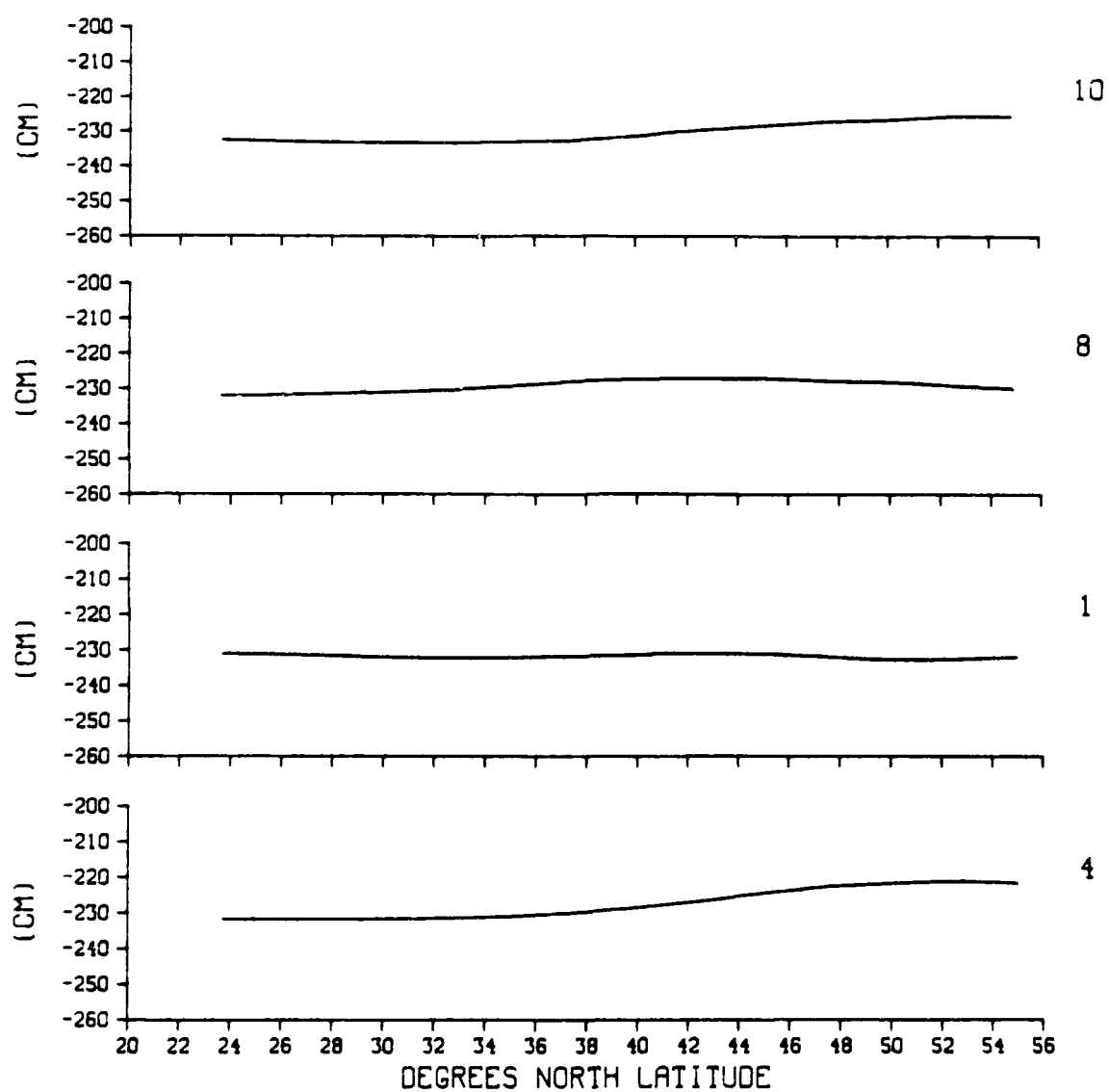


Fig. 2.10 Dry FNOC correction along arc 82.



Fig. 2.11a Power spectra of the difference profile for repeat 4 on arc 82 before (solid line) and after (dashed line) correcting for electromagnetic bias.

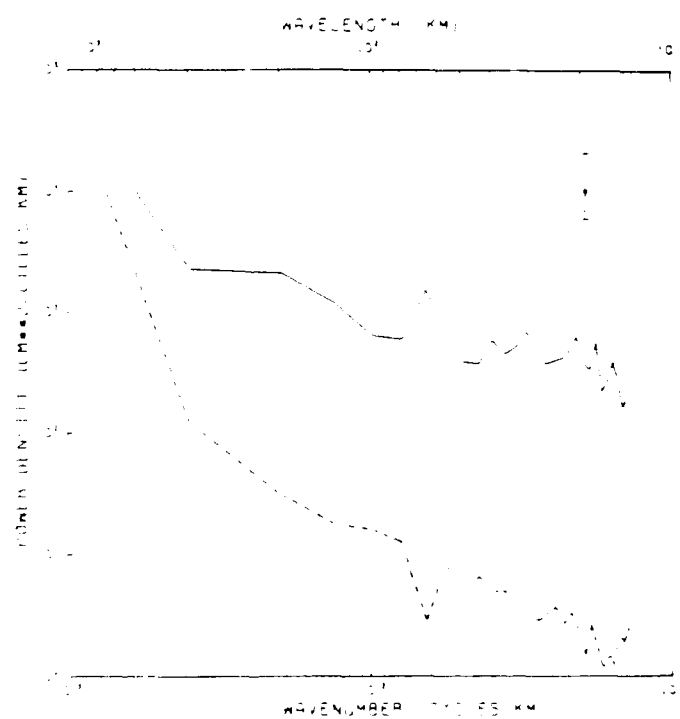


Fig. 2.11b Power spectra of the difference profile (solid line) and EM BIAS correction (dashed line) for repeat 4 on arc 82.

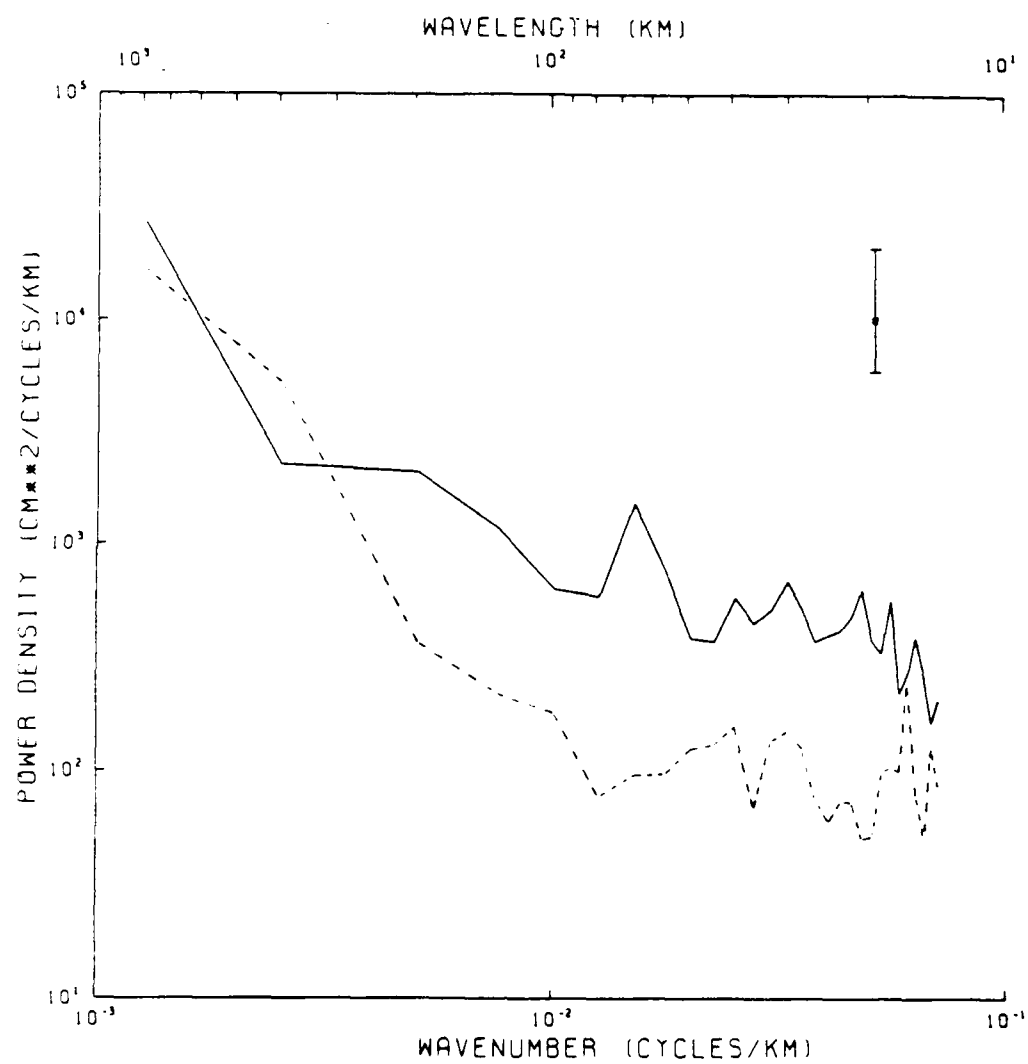


Fig. 2.12 Power spectra of the difference profiles for repeat 4 (solid line) and repeat 13 (dashed line) on arc 32. No corrections applied.

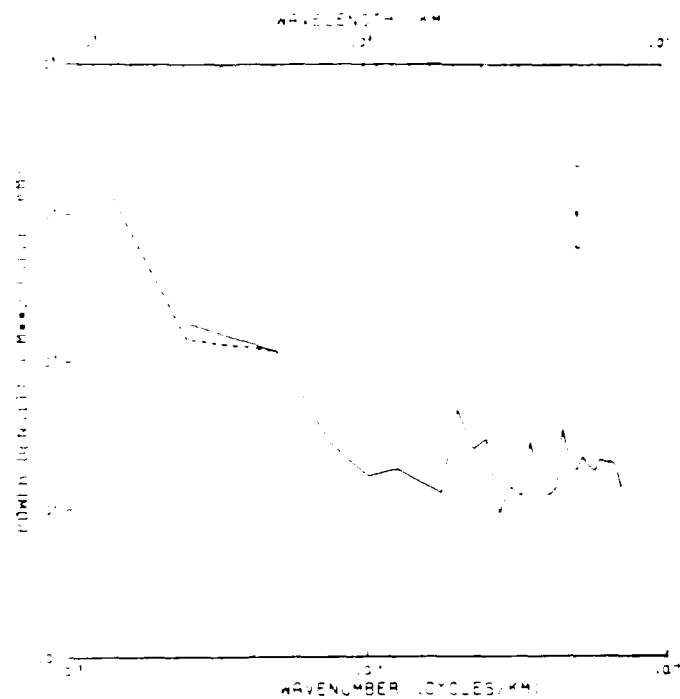


Fig. 2.13a Power spectra of the difference profile for repeat 10 on arc 82 before (solid line) and after (dashed line) correcting for ocean tide.

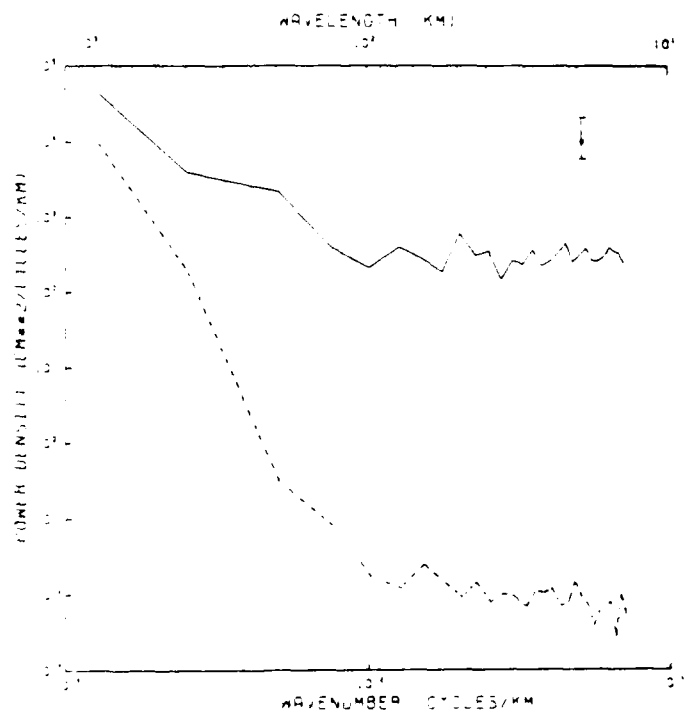


Fig. 2.13b Power spectra of the difference profile (solid line) and ocean tide correction (dashed line) for repeat 10 on arc 82.

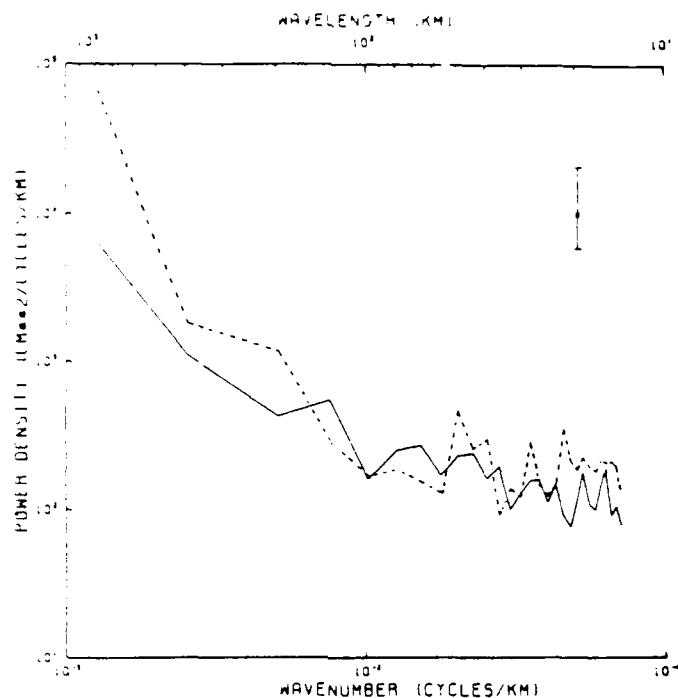


Fig. 2.14a Power spectra of the difference profiles for repeat 3 (solid line) and repeat 10 (dashed line) on arc 82, before correcting for ocean tide.

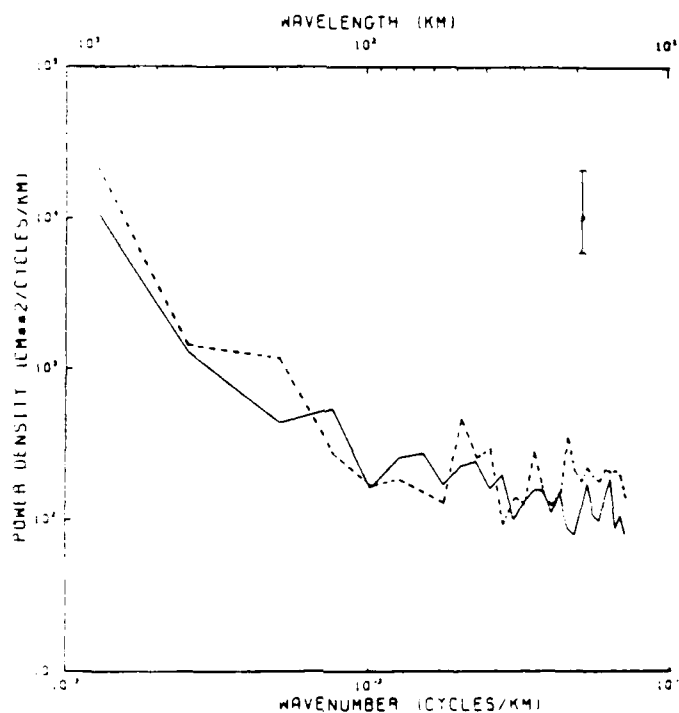


Fig. 2.14b Power spectra of the difference profiles for repeat 3 (solid line) and repeat 10 (dashed line) on arc 82, after correcting for ocean tide.

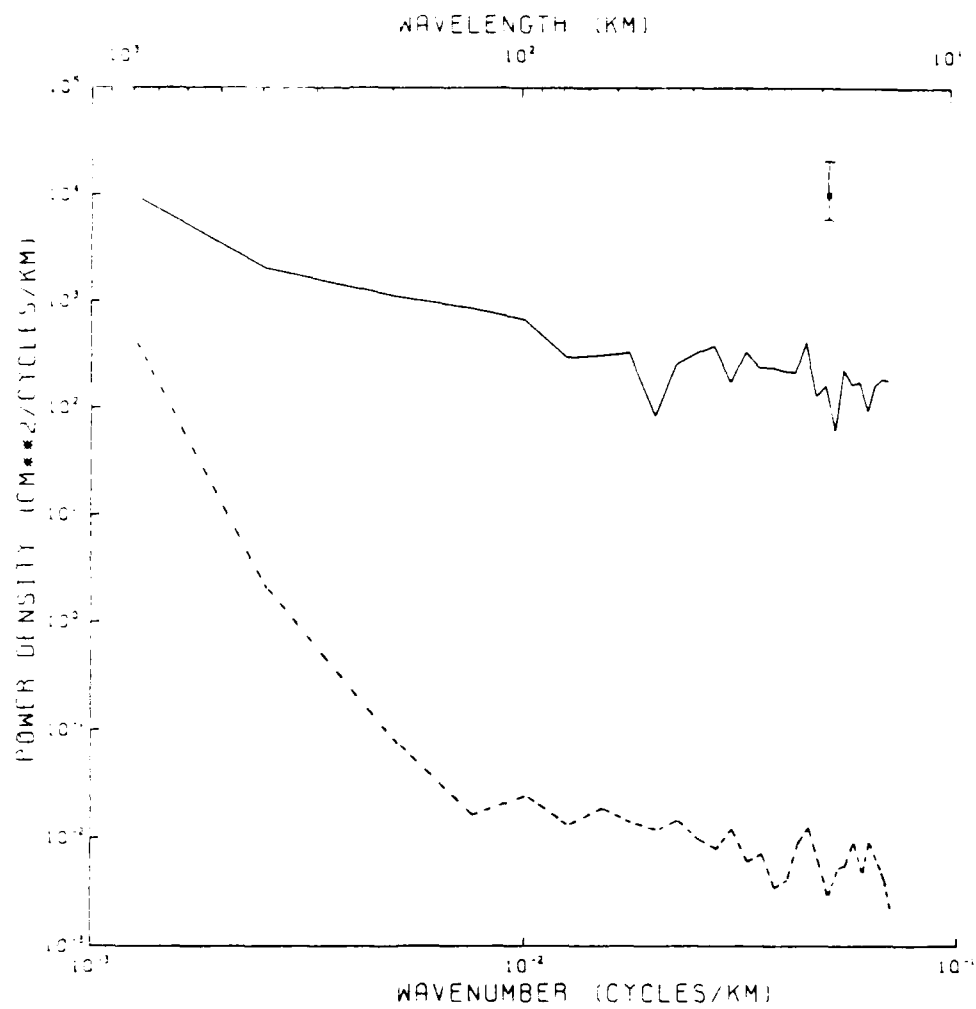


Fig. 2.15 Power spectra of the difference profile (solid line) and wet FNOc correction (dashed line) for repeat 9 on arc 82.

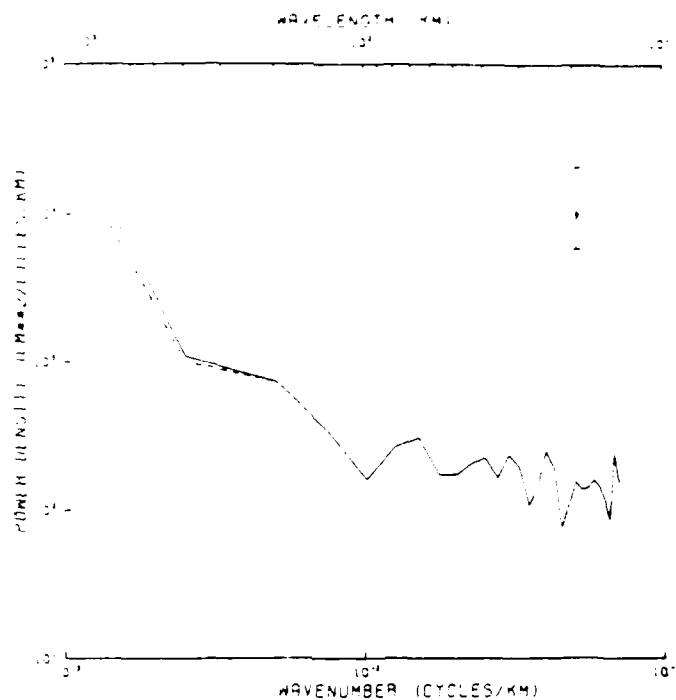


Fig. 2.16a Power spectra of the difference profile for repeat 8 on arc 82 before (solid line) and after (dashed line) correcting for dry FNOC.

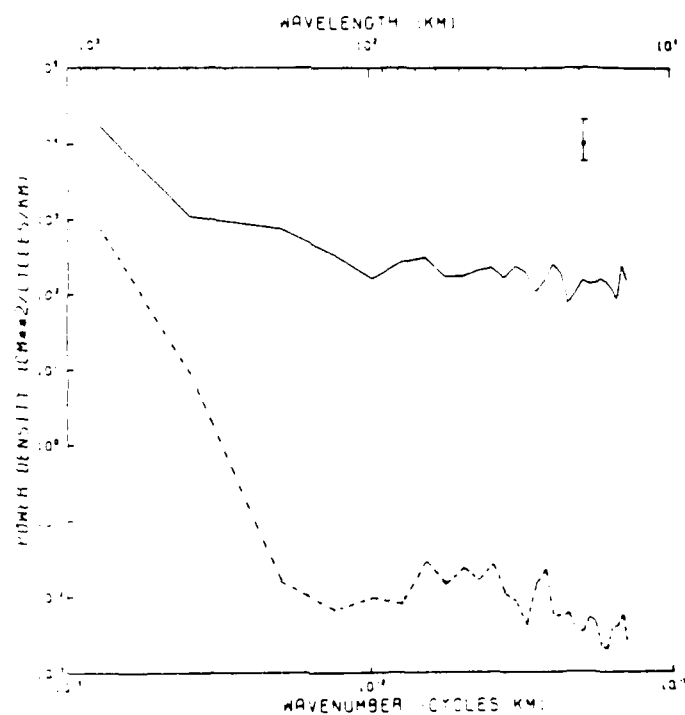


Fig. 2.16b Power spectra of the difference profile (solid line) and dry FNOC correction (dashed line) for repeat 8 on arc 82.

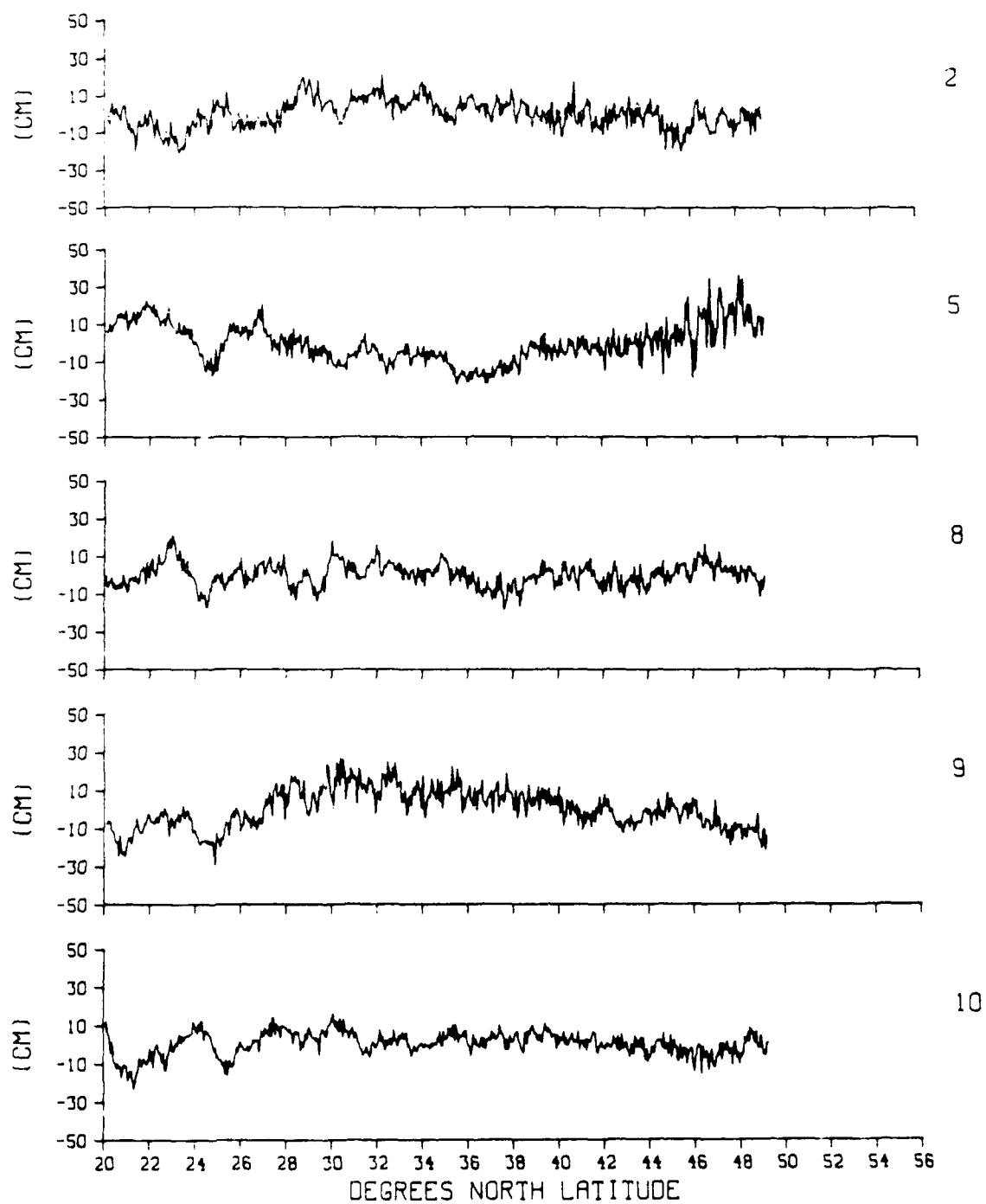


Fig. 2.17 Difference profiles along arc 209. No corrections applied.

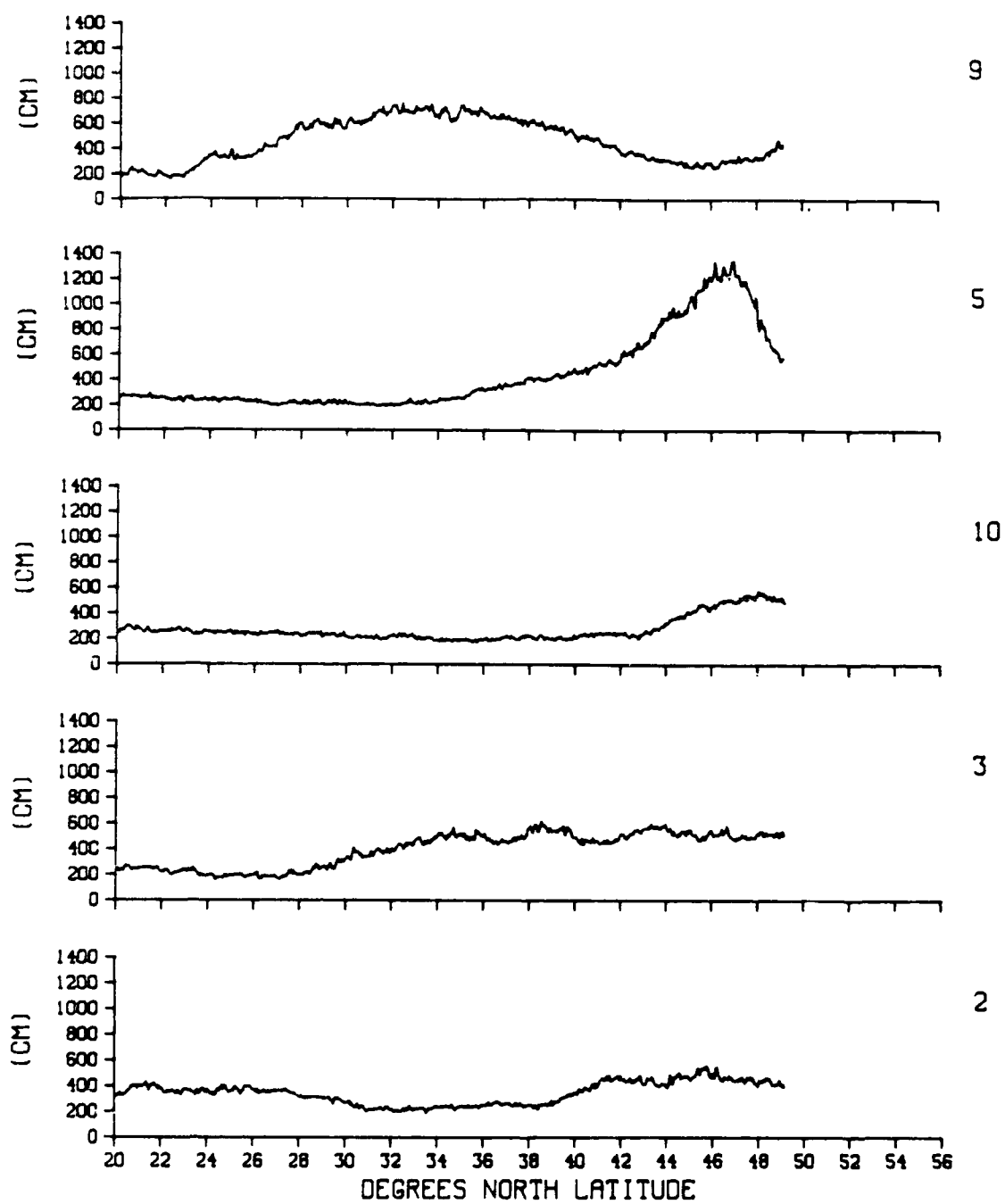


Fig. 2.18 Significant wave height along arc 209.

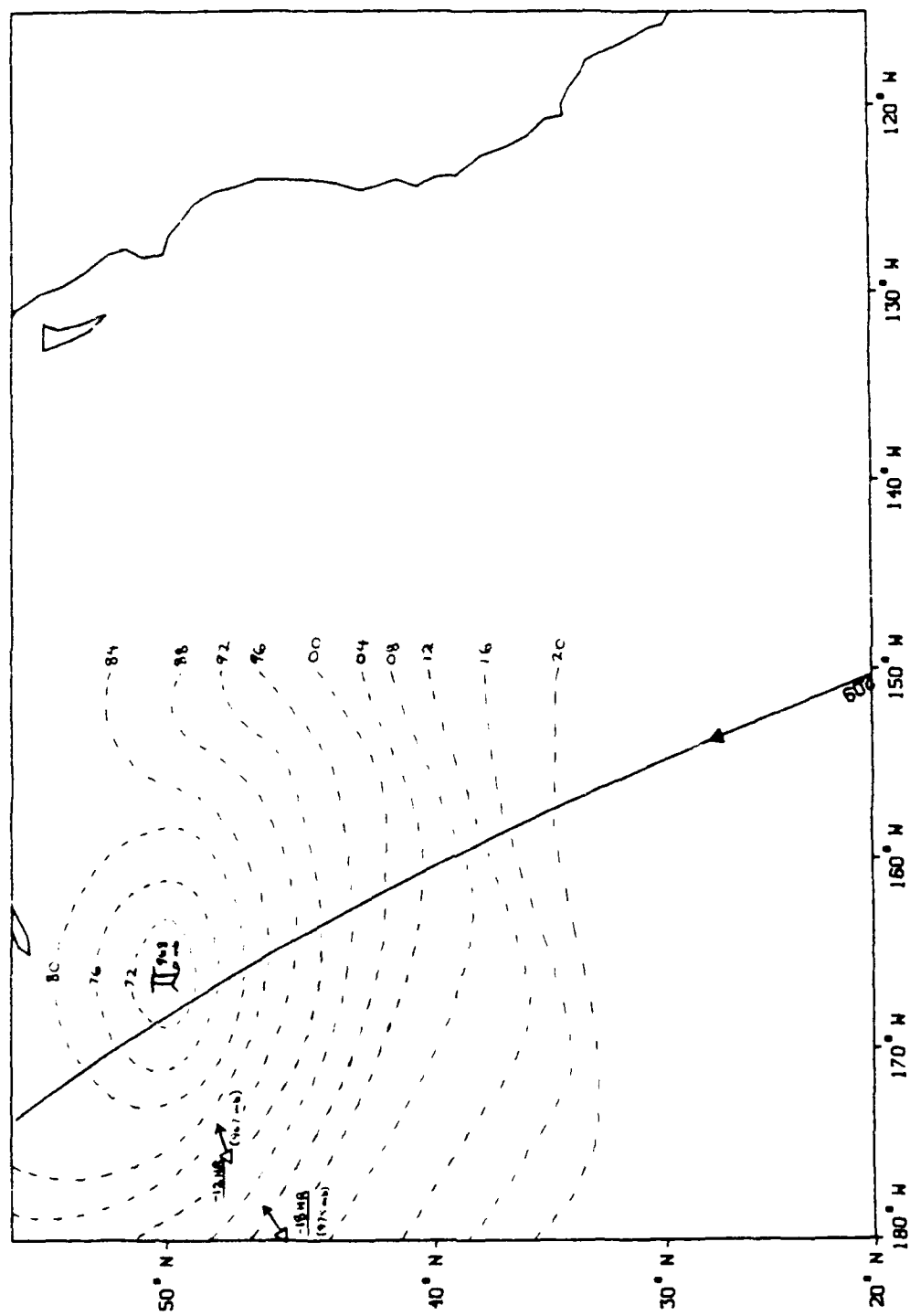


Fig. 2.19 Meteorological surface analysis for 22 January 1987 at 1200z. Repeat 5 on arc 209 occurs 3 hours later.

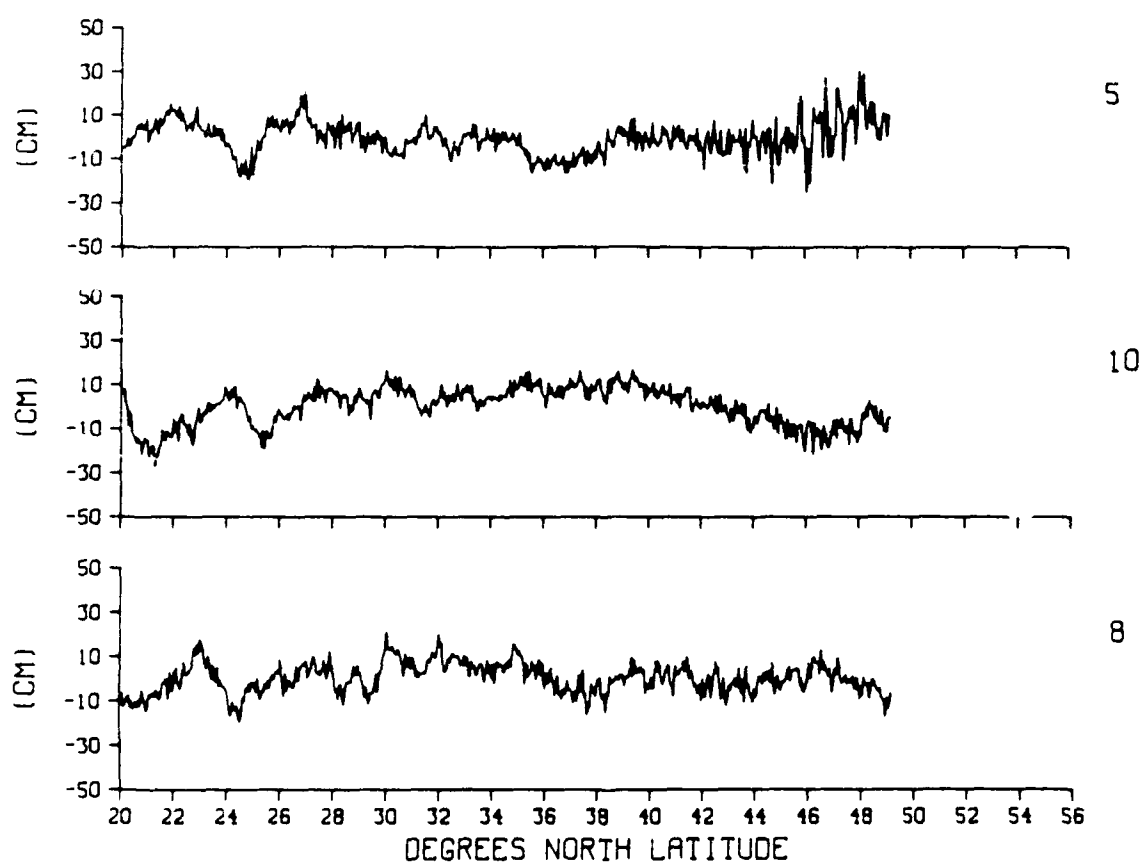


Fig. 2.20 Difference profiles along arc 209. Simple inverted barometer correction applied.

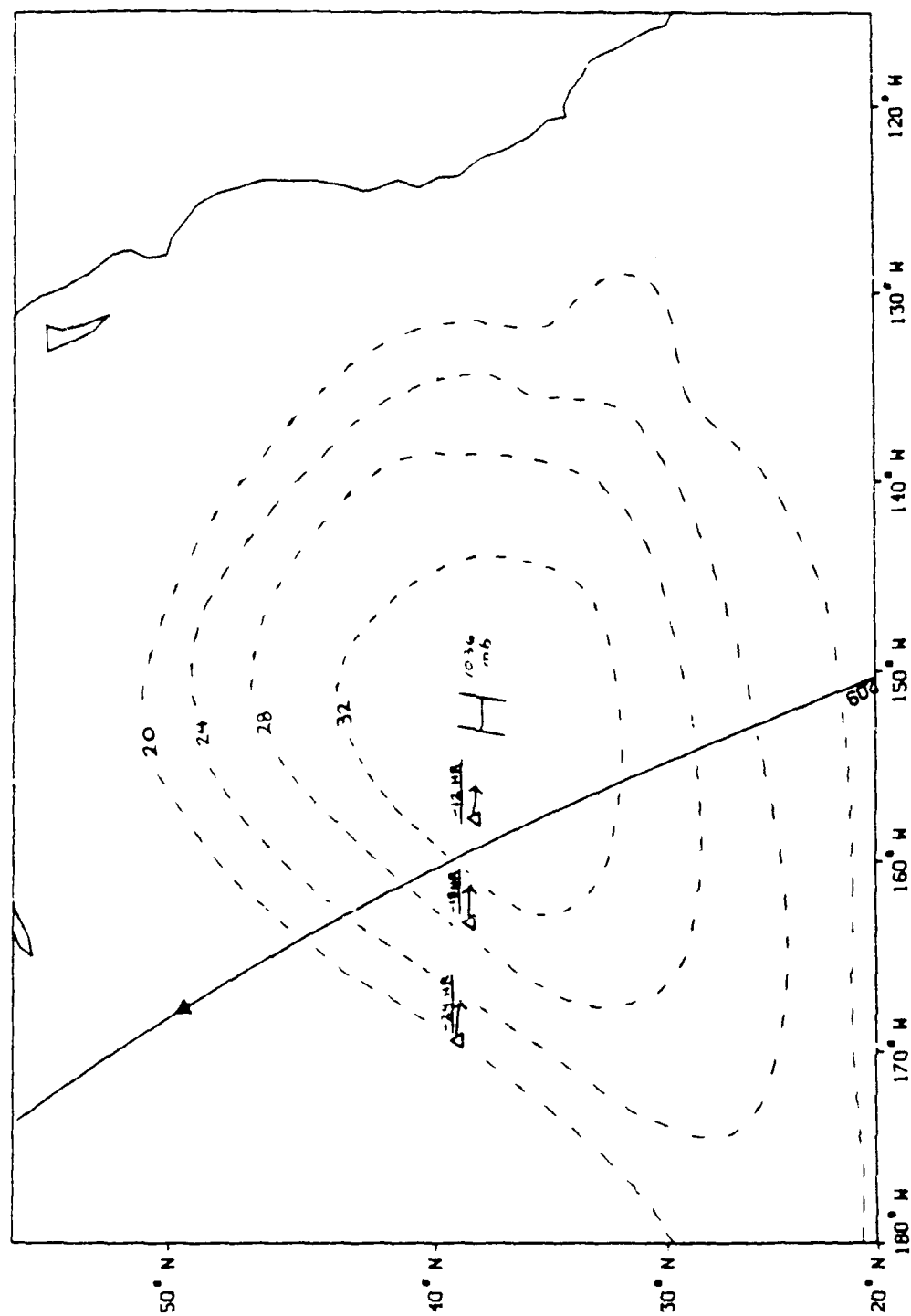


Fig. 2.21 Meteorological surface analysis for 17 April 1987 at 1800z. Repeat 10 on arc 209 occurs 3 hours later.

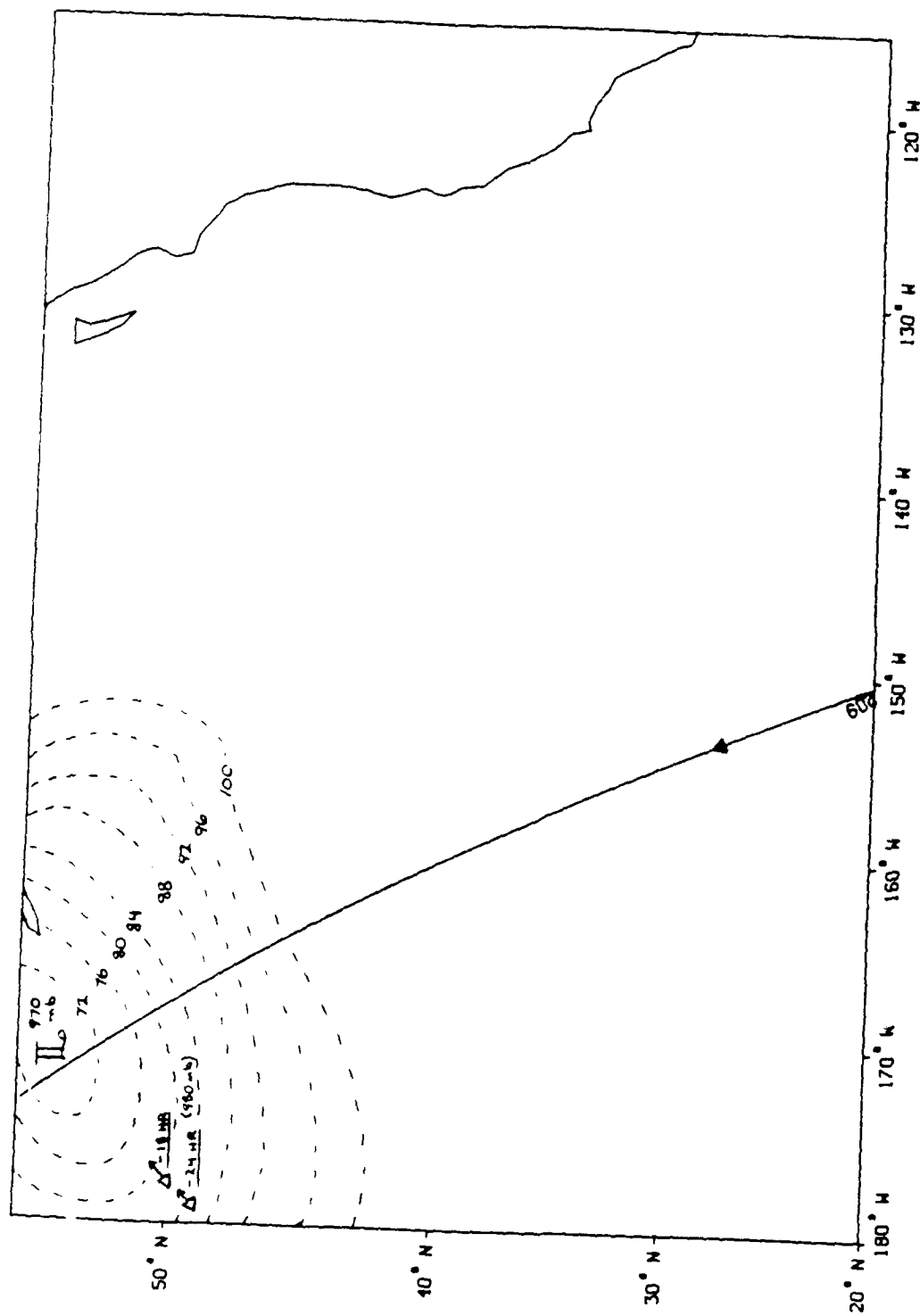


Fig. 2.22 Meteorological surface analysis for 14 March 1987 at 1800z. Repeat 8 on arc 209 occurs at this time.

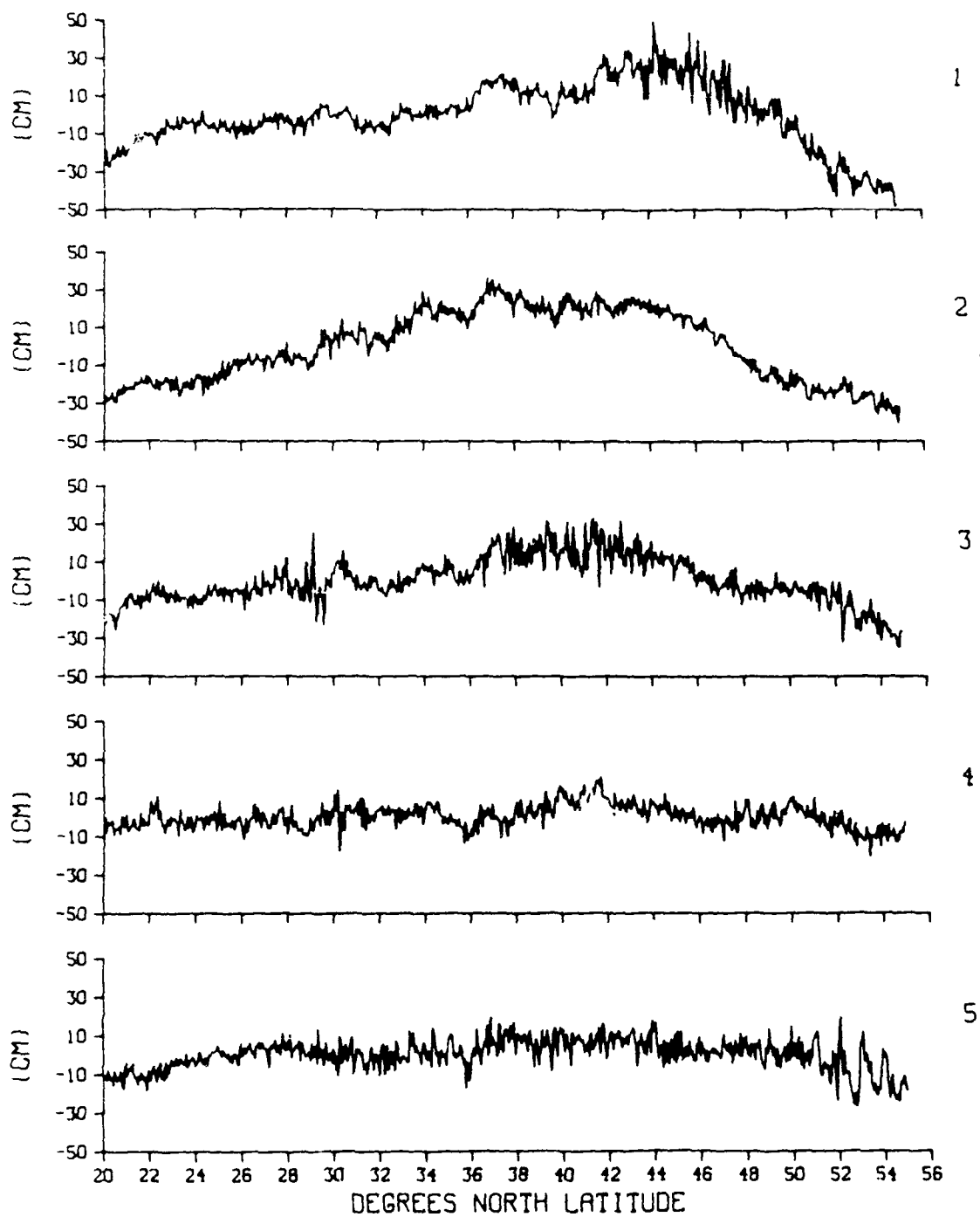


Fig. 2.23 Difference profiles along arc 293. No corrections applied.

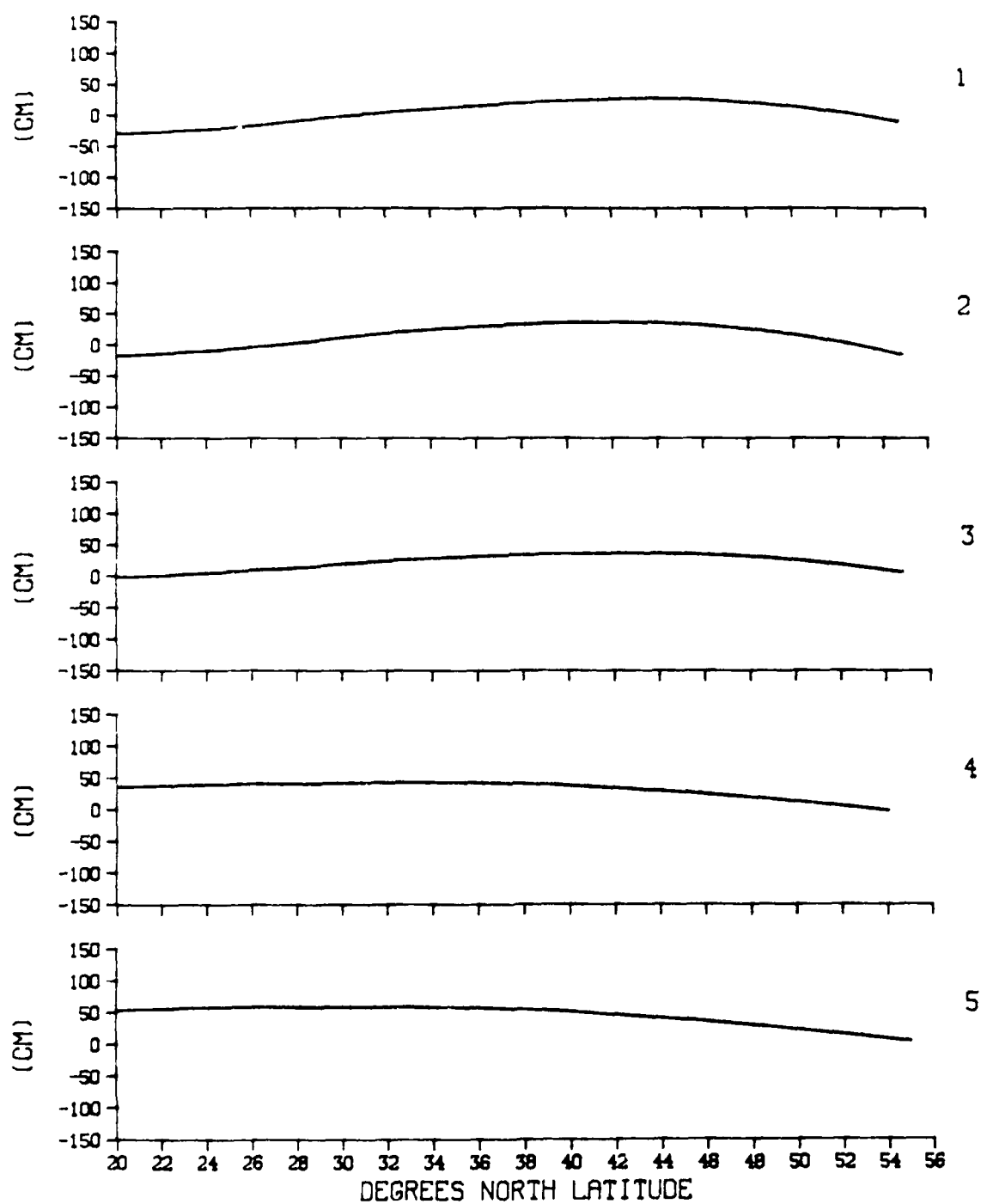


Fig. 2.24 Ocean tide correction along arc 293.

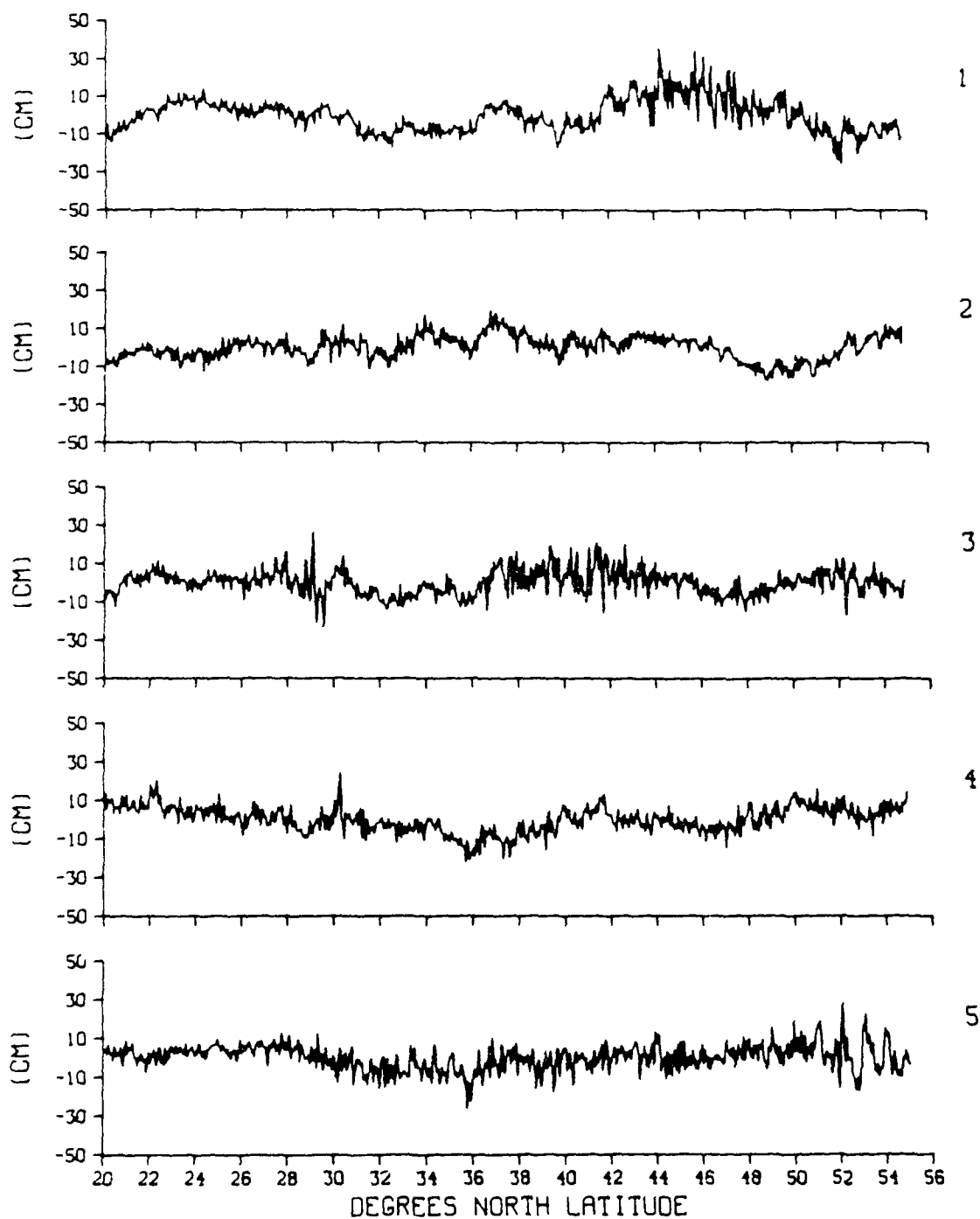


Fig. 2.25 Difference profiles along arc 293. Ocean tide correction applied.

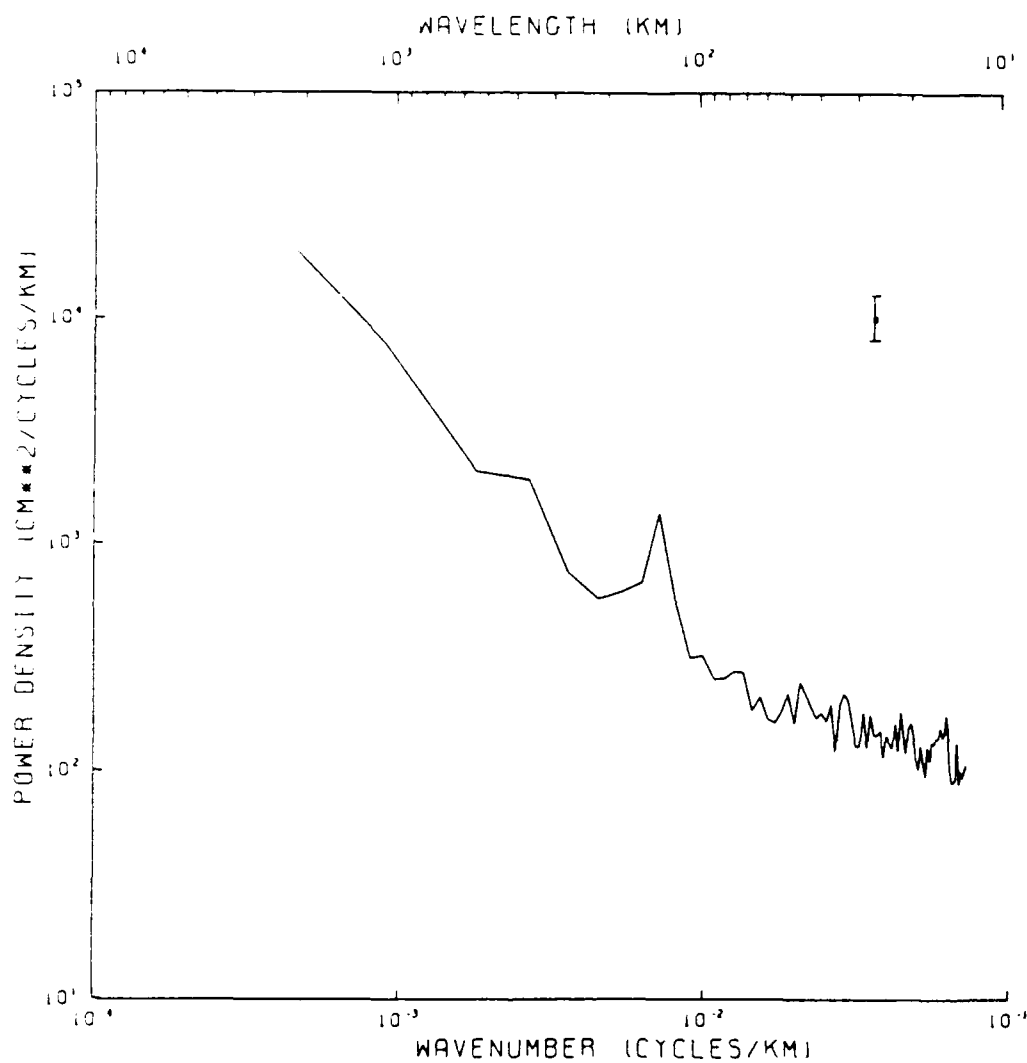


Fig. 2.26 Mean power spectrum of the 18 difference profiles along arc 293, corrected for ocean tide. The peak at 130 km is due to geoid contamination.

REPEAT	NO CORRECTION	EM BIAS CORRECTED	STIDE CORRECTED	OTIDE CORRECTED	WFNOC CORRECTED	WSMMR CORRECTED	DFNOC CORRECTED	IONOC CORRECTED
1	6.84	6.42	6.83	7.39	6.36	7.15	6.95	6.83
2	5.28	5.16	5.19	7.18*	5.35	5.41	4.94	5.27
3	5.26	5.33	5.27	6.92*	5.23	5.37	5.24	5.26
4	9.58	11.43*	9.85	9.24	8.95*	9.67	9.69	9.56
5	6.17	5.71	6.40	4.66*	6.86*	6.01	5.69	6.14
6	7.49	7.25	7.30	7.38	7.50	7.29	7.15	7.45
8	6.76	6.87	6.29	9.04*	6.32	6.92	6.19	6.77
9	6.86	6.50	6.66	10.52*	6.82	6.88	6.63	6.86
10	11.46	11.06*	11.54	7.31*	11.93*	11.31	10.68*	11.45
13	7.13	7.71	7.08	6.50	7.14	6.90	6.63	7.12
$\bar{\sigma}$	7.28 cm	7.34 cm	7.24 cm	7.61 cm	7.24 cm	7.29 cm	6.98 cm	7.27 cm
SSD	1.91 cm	2.21 cm	1.99 cm	1.63 cm	1.96 cm	1.86 cm	1.85 cm	1.91 cm

NOTES:

Figures under each correction indicate alongtrack variability (RMS) of each difference profile, with that particular correction applied throughout.

$\bar{\sigma}$ is the mean alongtrack variability over the ensemble of difference profile variabilities

SSD is the sample standard deviation of the ensemble of difference profile variabilities

* indicates that the change in variability on a repeat due to a correction exceeds an instrument noise of 3 cm (RMS).

Table 2.1 ARC 82 RMS variability of the difference profiles about the mean sea surface height profile, cm (1σ)

REPEAT	NO	EM BIAS	STIDE	OTIDE	WFNOC	WSMMR	DFNOC	IONO	INVB
		CORRECTED	CORRECTED	CORRECTED	CORRECTED	CORRECTED	CORRECTED	CORRECTED	CORRECTED
1	7.39	7.27	7.06	6.80	7.75	7.38	7.21	7.38	6.88
2	7.63	6.91*	7.22	7.15	7.58	7.54	7.61	7.62	7.73
3	7.35	6.80	7.35	7.57	7.46	7.45	7.44	7.35	8.02*
4	8.57	8.67	8.60	10.49*	8.90	8.75	8.55	8.58	8.61
5	10.69	12.92*	10.44	12.20*	10.08*	11.09	9.90*	10.71	7.90*
6	8.25	7.71	8.09	8.36	8.40	8.29	8.31	8.26	8.69
8	6.37	6.25	6.36	7.10*	6.32	6.32	6.39	6.38	6.97
9	10.29	13.03*	10.34	7.82*	8.84*	9.97	10.29	10.29	10.36
10	6.26	5.89	6.19	6.44	5.95	6.36	6.67	6.28	8.73*
11	9.80	10.33*	9.75	9.73	9.79	10.21	9.28*	9.84	7.89*
12	7.73	7.69	7.72	6.49*	7.54	7.37	7.73	7.70	8.14
13	5.67	5.85	5.72	7.94*	5.61	6.05	5.62	5.68	5.53
14	7.58	7.15	7.51	7.52	7.11	7.48	7.89	7.56	9.04*
17	8.92	8.71	8.61	5.54*	7.52*	8.35*	9.24	8.90	10.35*
$\bar{\sigma}$	8.04 cm	8.23 cm	7.93 cm	7.94 cm	7.78 cm	8.04 cm	8.01 cm	8.04 cm	8.20 cm
SSD	1.50 cm	2.34 cm	1.48 cm	1.78 cm	1.33 cm	1.52 cm	1.35 cm	1.50 cm	1.30 cm

NOTES:

See Table 2.1

Table 2.2 ARC 209 RMS variability of the difference profiles about the mean sea surface height profile, cm (1 σ)

REPEAT	NO CORRECTION	STIDE CORRECTED	OTIDE CORRECTED	WFNOC CORRECTED	WSMMR CORRECTED	DFNOC CORRECTED	IONO CORRECTED	INVB CORRECTED
1	17.47	16.71*	8.86*	18.18*	17.80*	17.22	17.45	16.66*
2	19.03	18.13*	6.53*	18.67*	19.63*	18.79	19.00	18.09*
3	12.61	12.23	6.86*	12.11*	12.94	12.06*	12.59	10.84*
4	6.35	6.59	6.91	6.85	6.40	6.66	6.34	8.32*
5	8.28	9.02*	6.80*	8.10	8.38	8.61	8.26	9.95*
6	5.96	6.17	6.55	6.23	5.94	5.52	5.95	7.21*
7	5.22	5.34	4.70	4.97	5.42	5.46	5.22	7.29*
8	6.14	6.24	5.16*	6.46	6.16	6.29	6.09	7.21*
9	7.73	7.68	5.40*	8.07	7.65	7.96	7.76	8.76*
10	11.19	11.24	6.14*	10.98	10.94	10.56*	11.17	8.66*
11	5.72	5.88	5.60	5.43	5.35	5.95	5.68	7.21*
12	9.95	10.49*	6.19*	10.33	9.39*	9.91	9.88	9.83
13	17.46	18.16*	9.56*	17.79*	17.37	16.33*	17.40	12.71*
14	8.91	9.51*	6.16*	8.15*	9.40	8.97	8.87	9.57*
15	4.63	4.77	6.45*	4.48	5.00	4.73	4.62	5.82*
16	9.66	9.57	5.16*	9.64	10.87*	9.45	9.63	8.76*
17	4.78	4.89	5.95*	4.13	4.46	4.60	4.78	4.68
18	7.67	8.49*	4.79*	7.66	7.72	7.90	7.65	9.00*
σ	9.37 cm	9.50 cm	6.32 cm	9.35 cm	9.49 cm	9.28 cm	9.35 cm	9.48 cm
SSD	4.54 cm	4.35 cm	1.26 cm	4.63 cm	4.67 cm	4.31 cm	4.53 cm	3.42 cm

NOTES:

See Table 2.1

Table 2.3 ARC 293 RMS variability of the difference profiles about the mean sea surface height profile, cm (1σ)

TIDE	EQUILIBRIUM AMPLITUDE (cm)	SOURCE	PERIOD, T (hrs)	ALIASED PERIOD, τ (days)
M2	16.83	LUNAR	12.420601	316.98
K1	9.83	LUNAR/ SOLAR	23.934470	175.47
S2	7.83	SOLAR	12.000000	168.86
O1	6.99	LUNAR	25.819342	112.95

NOTES:

- 1) All information except alias periods due to Parke et al. (1987).
- 2) Deep water tidal amplitudes reach up to about 4 times the equilibrium values.

Table 2.4 GEOSAT aliasing of ocean tidal components

CHAPTER THREE - USING THE DATA

3.1 OVERVIEW

The purpose of this chapter is to describe the use of GEOSAT data to investigate oceanic variability in the northeast Pacific, after editing it according to the lessons learned in Chapter 2. The collinear algorithm presented previously was slightly modified to handle data dropouts while maintaining the alongtrack matchup of data points between the repeat passes. Its steps are as follows:

- 1) Purge data points over land or flagged bad.
- 2) Subtract the Rapp geoid and Ocean Tide from the H values of each pass on the arc.
- 3) Remove spikes from the corrected profiles.
- 4) Detrend the profiles.
- 5) Identify a pass with no data dropouts; and starting with the second data point, define the latitude of every third point as a reference latitude.
- 6) For each pass, identify the set of data points which lie within $\pm\Delta/2$ of the reference latitudes, and make them the center points of the three point block averages. Assign an average sea surface height value to each of the center points unless a data dropout prevents the use of three points at the normal interval Δ . In that case, assign a latitude and height of zero to the center point involved.
- 7) Average a collinear ensemble of these edited profiles together to form a mean profile for the arc. If an edited profile is missing a center point for a particular reference latitude (i.e., zeroes assigned), interpolate for the sea surface height from the neighboring values.
- 8) Subtract the mean profile from each edited pass profile in the ensemble to create the set of difference profiles.

This algorithm was applied to an ensemble of 18 repeat passes on arc 293. The resultant difference profiles are shown in figures 3.1 through 3.4. The following section shows what knowledge of the oceanic mesoscale may be inferred from such data.

3.2 VARIABILITY ON ARC 293

Many observations may be made from the full set of arc 293 difference profiles. Perhaps the best place to start is by noting how generally quiet the Pacific ocean appears to be in them. Arc 293 runs roughly parallel to the California coastline, some 1000 km offshore; and except for its northern section near Alaska, it is largely removed from significant current systems and their associated mesoscale features. The ensemble average of the RMS alongtrack variabilities computed from the difference profiles ($\bar{\sigma}$) is only 5.6 cm, and the quietest repeats such as 8 and 9 have RMS values down near 4.5 cm.* If the ocean itself is fairly quiescent at these times, the latter figure may be thought of as representing a lower bound on the noise of the GEOSAT system. This limit is a combination of the instrument noise, positioning errors (including orbit and horizontal offsets), ocean tide modelling errors, and the environmental effects not corrected for. It is well within the worst case limits presented in the table 1.2 Error Budget, and certainly low enough to justify post facto the use of linear detrending rather than some higher order means of reducing the orbit error.

The difference profiles are by no means featureless, however, and one's eye is quickly drawn to a number of things. For example, what are the short wavelength oscillations seen on repeats 1 and 3 (among others), and what are the periodic undulations found in the northern regions of repeats 10 and 13? Is the U-shaped feature at $\sim 30^\circ\text{N}$, seen in various stages of growth and decay on repeats 6 through 9, a cold eddy or some environmental effect not corrected for? At longer wavelengths; what is the dip in sea surface height in repeat 2 centered on 50°N , or the gentle rise in the northern region of repeat 13? Are these real oceanographic features or something else? The signatures seen on the difference profiles will be investigated in order of increasing wavelength within the following subsections.

* These variabilities are smaller than those seen in table 2.3 in the OTIDE column, due to the 3 point averaging.

Short Wavelength Features

"Short wavelength" refers to the features of smallest horizontal extent seen on all the difference profiles - the spikes. Each spike is the result of one sea surface height being significantly (~5-10 cm) different from its neighbors. A single outlying height results in a simple spike with a horizontal extent of some 40 km (the distance spanned by the outlier and its neighbors to either side). Two successive outlying points, one high and one low, create alternating spikes with a combined "wavelength" of 60 km. A reasonable choice as the upper limit for short wavelength features provides some extra margin, and is here defined to be 100 km.

The assertion is that these signatures on the difference profiles are not real oceanographic features. Rather, they are a manifestation of the high wavenumber altimeter noise seen previously - aliased down by the increased sampling interval. Aside from spectral methods, this assertion is supported by two observations. First, as mentioned in Section 1.4, there is simply no independent data which suggests that the sea surface height fluctuates some 10 cm or more within such a short distance. Second, the short wavelength features appear to be highly correlated with regions of large significant wave height. Such regions were seen in Chapter 2 to be associated with a worsening of the altimeter precision and a corresponding rise in instrument noise - not with mesoscale features. Comparison of figure 3.5 (which plots SWH along five of the arc 293 repeat passes) and the difference profiles demonstrates this association.

Spectral methods give further support to the idea of the spikes being non-oceanographic in origin. If one accepts that the spikes are random noise, then an increase in their number and/or amplitude should serve only to raise the general power level at high wavenumbers. This is demonstrated in figure 3.6. Repeats 4 and 5 have very similar difference profiles, except that repeat 5 has larger and more numerous spikes (although not pictured, repeat 4 had an average SWH alongtrack of <3 m). Their respective power density plots show that the high wavenumber power has risen rather evenly from repeat 4

to 5, indicating that the spikes are probably random in nature. Further indication that the short wavelength spikes are system noise may be seen in coherence plots between successive difference profiles. As an example, figure 3.7 indicates the coherence phase and amplitude between repeats 4 and 5. Note how the amplitude drops rapidly below the 95% level of no significance as wavelengths get smaller than ~ 100 km; indicating that the short wavelength features are essentially uncorrelated between the repeat passes. This is characteristic of random noise.*

It must be remarked that the above behavior is by no means isolated. The power spectra of the profiles with the most spikes all have elevated power densities at wavelengths ≤ 100 km; and coherence plots between successive passes show no significant coherence in the same wavelength regime. The conclusion is as proposed - the short wavelength features are altimeter noise. As such, even more successive point averaging could be applied to the sea surface heights, with five points instead of three being a reasonable choice.

In order to complete the discussion of short wavelength features, mention must be made of the effects of clouds and rain upon the altimeter measurement. Goldhirsh and Rowland (1982) have shown that any delaying of the radar pulses due to the presence of rain and clouds results in a height error which is small enough (< 2 cm) to be ignored. Clouds and rain may create a significant height error, however, if they attenuate the radar pulse in a spatially variable manner over the radar footprint area. Monaldo et al. (1986) showed that this variable attenuation distorts the return waveform and so causes the half-power point to be mistracked. The tracking error results in erroneous pulse travel time calculations; giving RMS sea surface height errors (after 3s of averaging, as performed

* Non-sinusoidal features such as those on the difference profiles cannot be linked with one particular wavenumber on a power spectrum. Thus the 100 km cutoff in the power spectra should not be confused with the horizontal size of the short wavelength features. The wavenumber regime is used more in a qualitative sense here, to indicate the noise-like behavior of the shortest horizontal scales in the difference profiles.

here) of up to 0.6 cm and 14.9 cm respectively, for idealized single-cloud and rain-cell models encountered by a SEASAT class altimeter (with a 2 m SWH). The cloud induced error is therefore negligible, and Goldhirsh (1983) has estimated that the spatial scales of rain cells are very short - about 3 km on the average for cells with a rain rate ≥ 10 mm/hr. Thus, rain-induced altimeter error occurs on much too short a scale to be mistaken for oceanographic phenomena, and may just be considered as increased altimeter noise.

Mid Wavelength Features

Mid wavelength is here defined as those features having a horizontal extent from 100 to 500 km on the difference profiles. This range includes such features as the U-shapes seen around 30°N in repeats 6 through 9, and the periodic variations in sea surface height found in the northern regions of repeats such as 10 and 13. The mid wavelength regime is a good one in which to find oceanography - for two reasons. First, it contains most mesoscale features (Pond and Pickard, 1983). Second, it lies above the upper wavelength limit of the altimeter noise and below the horizontal scales of many corrections. Thus it is less likely than either the short or long wavelength regimes to be contaminated by these non-oceanographic effects.

There are three possible sources for the mid wavelength features seen in the arc 293 difference profiles. These are geoid contamination, environmental effects, and mesoscale oceanography. Geoid contamination is examined first.

Geoid contamination was seen in Chapter 2 to be a result of collinear processing in those areas where the geoid is changing rapidly with horizontal distance. Contamination was the reason why regions of test arcs 82 and 209 were excluded from the analysis conducted on the corrections; but was not deemed to be enough of a problem to warrant any deletions from arc 293. Nevertheless, the mean sea surface height profile and its alongtrack gradient for arc 293, shown in figure 3.8, indicate that geoid contamination may not be completely ignored. Note especially the large gradients in the mean sea surface (which is mainly a reflection of the geoid) at 40°N and north of ~44°N. Any repeat passes

which are not coincident with the mean profile, either along or across track, will incur false signatures in these areas on their difference profiles. The horizontal scale of these signatures will be the same as the horizontal scale of the geoid variation (~ 140 km wavelength for the somewhat sinusoidal variations seen north of 44°), and their magnitude may be estimated from the alongtrack gradient. This latter value is around 3-4 cm/km in the most troublesome regions. Since the sliding scheme discussed earlier allows any pass to be as much as ~ 3.4 km ($\Delta/2$) away from the reference latitudes of the mean profile; features of around 10-15 cm in magnitude may appear on the difference profiles, due to geoid contamination. (Note that crosstrack offset between the repeat passes also gives rise to geoid contamination. In general, this is not a problem, as crosstrack offsets are limited by the orbit to ± 1 km. In the case of arc 293, there is even less difficulty, because the arc is roughly perpendicular to the strike of the Aleutian island chain - which means that the geoid variations seen in that region are of greatest magnitude along the arc).

The regions of large alongtrack sea surface gradient in the mean profile are the ones which must be scrutinized most carefully for geoid contamination on the difference profiles. As remarked, these are at 40°N and north of 44°N for arc 293. A particularly fortunate occurrence is the periodic nature of the geoid variation in the northern region of the arc; making contamination easy to spot in this case. Using this periodicity as a guideline, one is immediately drawn to the regular features north of 44° which appear to some extent in many of the difference profiles (figures 3.1 through 3.4); but are most noticeable in repeats 10, 13, and 16. The scale and amplitude of these signatures closely match those just predicted as being geoid-induced; and output data from the collinear sliding scheme indicate these passes as being the furthest south of all 18 passes in the ensemble. Thus they are the most likely ones to be contaminated by the geoid, as expected. Further proof of the artificial nature of the periodic features may be seen by sliding passes 10, 13, and 16 even more to the south, which should exacerbate any geoid contamination. This is exactly what happens, as seen in figure 3.9. Note how features longer than the mid

wavelength ones are relatively unchanged by the sliding, but mid wavelength ones grow all along the arcs, especially north of 44° and at 40° . In general, all the periodic features north of 44° , as well as signatures at 40°N seen on the arc 293 difference profiles, behaved in this way and so were classified as non-oceanographic in origin.

Two other aspects of geoid contamination bear discussion before finishing with the topic. The first regards the effect which geoid contamination has on the power spectra of the arc 293 difference profiles, and is a result of the periodic geoid fluctuations seen in that arc's mean profile. These regular features result in increased energy in the power spectrum of the mean profile at those wavelengths surrounding the periodic one. This increase can be seen in figure 3.10, which shows a definite peak in the power density of the mean profile at a wavelength of around 130 km. When a repeat pass is shifted in an alongtrack sense from the mean, that mid wavelength energy will bleed into the difference profile, as shown in figure 3.11a. Note the very large coherence at 130 km between the arc 293 mean profile and the highly shifted repeat 10. (The 90° phase difference is a direct result of the shift). This bleedover results in a peak in the wavenumber spectrum of the contaminated difference profile (figure 3.11b). Since a number of the difference profiles for arc 293 contained some sort of geoid contamination, a mean spectrum formed from their individual power spectra would also show increased energy at wavelengths around 130 km. This explains the significant peak at this wavelength in the arc 293 average power spectrum, shown at the end of Chapter 2 (figure 2.26).*

The final aspect of geoid contamination which should be covered concerns the feasibility of investigating oceanographic features in regions of large geoid gradient. Although there are no cut and dried answers to this question, a few general comments may be made. First, areas of large geoid gradient often correspond with regions of high

* The narrowness of the peak seen in Chapter 2 is a result of the increased wavenumber resolution afforded by averaging fewer Fourier coefficients together. This could be done without degree of freedom limitations, as 18 spectra were always available for averaging.

oceanographic activity, so these places are ignored at the investigator's peril. If the activity is vigorous enough, or the offsets happen to be small enough, then oceanographic features may still be detected with no special data processing. If these cases are not in effect, more care must be taken in the collinear algorithm to minimize alongtrack offsets between the repeat passes. This may be done by interpolating between the original data points with a cubic spline, for example, and then resampling the resultant continuous profiles at the exact reference latitudes desired. Alongtrack offsets may be almost completely eliminated in this way, although at the expense of increased computer time and storage space.

Unfortunately, if the crosstrack geoid gradient is large enough, the difference profiles will remain contaminated even after alongtrack offsets are removed. The interpolation technique is not used here, as a number of difference profiles such as repeats 2 and 6 are still able to pick up interesting features without it.

The second possible source of mid wavelength features on the difference profiles is the altimeter error caused by environmental effects. Within the mid wavelength range, table 1.2 indicated that only the EM BIAS and wet troposphere effects should have any significant affect on the difference profiles. Chapter 2's investigation of all the GDR corrections confirmed that these two phenomena could be quite noticeable at times (especially the true wet troposphere effect; which often exceeds the modelled WFNOC correction). The lack of consistent variability reduction when corrections were made for these effects prevented their use in the data set used in this chapter, however. Thus, the difference profiles for arc 293 (figures 3.1 through 3.4) may well show mid wavelength features which are due to EM BIAS or the wet troposphere effects, rather than oceanography.

There are ways of picking out the environmental signatures from the difference profiles, however. First, Chapter 1 related how increases in the EM BIAS and wet troposphere effects depress the apparent sea surface when not corrected for. Thus, isolated increases in sea surface height are probably not due to these phenomena, as intuition and

experience suggests that highly localized decreases in wave height and water vapor are uncommon. This observation is not of much use on the arc 293 difference profiles; but it does, for example, disqualify EM BIAS or the wet troposphere effects as having caused the peak in sea surface height seen in the repeat 13 difference profile on arc 82 (figure 2.5).

The second way of spotting the environmental signatures is based upon knowledge of the time scale of these phenomena. Both EM BIAS and water vapor evolve with the time scale of weather - which is only a few days. Therefore, features which persist through successive difference profiles are very likely not environmental but oceanographic in origin (assuming geoid contamination has already been ruled out).

Given a set of difference profiles and the known geoid and environmental effects, the identification of mid wavelength oceanographic features may be summarized as follows: First, line up the difference profiles vertically in time order (as done in figures 3.1 through 3.4). Then, look for features which persist in the same general region over two or more repeat cycles. This is the time scale over which most mesoscale activity occurs, and it also rules out false signatures from the EM BIAS or wet troposphere effects. If the features move noticeably between the repeats, geoid contamination may be ruled out, as this effect's movement is limited to $\pm\Delta/2$ (i.e., ± 3.4 km) by the sliding technique. If the features appear stationary, the mean sea surface height profile and its gradient may be checked in that area to determine the magnitude of any geoid contamination. The product of $\Delta/2$ and the maximum local gradient give a good estimate of the contamination magnitude. If the observed features exceed it, they are likely oceanographic in nature.

Use of the above technique highlighted some interesting mid wavelength features on the arc 293 difference profiles as being probably oceanographic in origin. The most striking of these is the U-shaped dip in the sea surface which first appears in repeat 6 at $\sim 30^\circ\text{N}$, grows through repeats 7 and 8, and decays by repeat 9. The dip is located approximately at 29.5°N , 128°W , putting it about 1000 km southwest of Los Angeles and 750 km from the California shelf break (see figure 1.3 for the arc location). It has a

magnitude of at most ~15 cm, a horizontal extent of around 240 km (using repeat 8), and persists through at least 3 repeat cycles (50+ days). These are reasonable values for a cold eddy in this region (e.g., McNally[1981], Pickard and Emery [1982]). A likely source for such an eddy would be the southward flowing California current, which regularly sheds cold mesoscale features (the eddy is classified as cold because the observed difference profile dip is an indication of the increased density of cold water). There is also some indication that the eddy could be moving to the southwest (perpendicular to the arc), as it does not appear to change position with respect to the arc, but does change in horizontal size. Thus, the small, weak signature seen in repeat 6 could signify the first intersection of the arc with an eddy moving from the northeast. As the eddy passes through the arc, its cross section increases through repeat 8, and then decreases as it moves to the southwest of the arc. A rough estimate of the eddy speed may be made from its maximum diameter (~240 km in repeat 8) and time of passage (estimate 60 days), as being 4 km/day. This figure is reasonable (e.g., Pickard and Emery [1982], Chap. 7).

Mid wavelength features which appear less simple than the cold eddy, but nevertheless seem to be oceanographic in origin, may be seen from 28° to 32°N on difference profiles 11 through 14 (figure 3.3). A suggestion for future work would be to compare these signatures with other data sources such as infrared imagery or tomographic data. Work of this kind could eventually catalogue typical difference profile expressions of mesoscale features and so allow the altimeter data to stand alone as a primary source of descriptive oceanography. Future goals notwithstanding, the encouraging result of this subsection is that the GEOSAT data picks up probable oceanographic features of relatively small amplitude, even with rather unsophisticated processing.

Long Wavelength Features

Long wavelength features are defined as those having a horizontal extent greater than 500 km on the difference profiles. It is difficult to find oceanographic signatures in this wavelength range, because it is here that the altimeter errors have their greatest

expression. In addition, oceanographic features with wavelengths approaching the arc length will not appear in the difference profiles anyway, as seen in Section 1.2.

The prevalence of altimeter errors in the long wavelength features seen in figures 3.1 through 3.4 was verified by comparing the difference profiles with the most energetic GDR corrections identified in Chapter 2, and with meteorological data. For example, meteorological surface analysis charts indicated that the long wavelength features seen in repeats 1 (32° - 54° N), 3 (34° - 48° N), 6 (50° N+), and 13 (44° N+) could all be attributed to the inverse barometer effect. Plots of the WFNOC correction and satellite maps of integrated atmospheric water vapor accounted for the long wavelength variations all along repeats 4 and 17, as well as the significant dip in sea surface height from 46° to 54° N on repeat 2. Electromagnetic bias explained the smooth curve in the sea surface beginning at 28° N on repeat 5.

The reader should remember that these three significant environmental errors remain in some of the difference profiles because they were not modelled well enough overall to allow correcting for them. Two things would largely alleviate these deficiencies, however. First, a water vapor measurement coincident with the altimeter reading would pick up many of the fluctuations in this phenomenon which are not adequately depicted in the FNOG model. The upcoming TOPEX/POSEIDON mission should provide this capability with an onboard SMMR. Second, an accurate frequency/wavenumber dependent inverted barometer correction would not only remove this phenomenon from the sea surface heights, but allow the EM BIAS correction to be more effective as well (see Chapter 2 for discussion on the interplay between EM BIAS and the inverted barometer effect).

In addition to the long wavelength features that are caused by uncorrected altimeter errors; any errors in applied corrections will also result in false signatures on the distance profiles. For example, non-linear orbit error will not be removed with the bias and tilt correction, and will result in very long wavelength curvature in the difference profiles (see repeat 15 in figure 3.3). Also, the large error (10 cm RMS) in the applied ocean tide model

may produce unwanted difference profile features in the 500-1000 km wavelength range. This can be especially serious due to the previously mentioned aliasing of the ocean tide; which may result in correlated model errors over several repeat cycles.

Upon examining the full set of arc 293 difference profiles for long wavelength features, no signatures were found that could be considered as probably oceanographic in origin. This is not unexpected, and will continue to be a problem with altimeter data until better orbits and corrections are calculated.

3.3 DATA COMPARISON

Section 3.2 indicated that mesoscale variability may be observed in GEOSAT difference profiles if one knows how and where to look. With this basic capability thus established, the current section compares GEOSAT - derived variability results for the northeast Pacific with two other studies of the region. The comparisons not only aid in determining the general accuracy of the GEOSAT product, but also lend new insights into the dynamics of the test area.

Wavenumber Spectra

Fu (1983) used SEASAT data from repeat orbits during the last 24 days of its operation to calculate wavenumber spectra along the satellite tracks. The spectra were determined from difference profiles using the collinear technique, and so were actually spectra of the oceanic variability. Fu calculated average wavenumber spectra for two types of oceanic regions - those of high and low energy (i.e., variability). The regions were chosen according to the eddy-energy maps of Wyrki et al. (1976), compiled from ship-drift data; and of Cheney et al. (1983), who utilized SEASAT data.

One of Fu's low energy regions (his area 3) closely corresponds with the test region of this work. Within it, Fu chose 6 SEASAT arcs; each having approximately 8 repeats along it (the SEASAT repeat period was 3 days). Alongtrack wavenumber spectra for each of the 50 odd difference profiles in the region were calculated, and then averaged together. From the resultant regional spectrum, Fu found that SEASAT system noise

extended from the shortest wavelengths out to 100 km, and that the regional spectrum followed a k^{-1} slope between wavelengths of 100 and 1000 km.

Arcs 209 and 293 were chosen to compare GEOSAT data with the results of Fu. For each arc, a wavenumber spectrum for each difference profile was calculated, and the resultant set of spectra was averaged together. These averaged spectra, one each for arcs 209 and 293, appear in figure 3.12. For comparison, the power density of the Fu regional spectrum is plotted as circles at wavelengths of 100, 1000, and ~ 1100 km, within their 95% confidence intervals. The confidence interval in the upper right of the figure is appropriate to the arc 209 spectrum and is slightly larger than the one (not shown) for arc 293, which had more spectra available for averaging.

A number of important observations may be obtained from figure 3.12. First, note how closely the power levels of the three spectra correspond at 100 km. This similarity is to be expected, as power at 100 km consists primarily of altimeter system noise (see Section 3.2), which is comparable between SEASAT and GEOSAT (~ 0.1 m, as shown in Chapter 1). While Fu's spectrum went fully white (i.e., horizontal) at wavelengths shorter than 100 km, however, observe how the GEOSAT spectra still continue to drop, albeit not as steeply as at longer wavelengths. This would indicate that GEOSAT is actually slightly more accurate than SEASAT, which is not surprising, as the GEOSAT noise floor was estimated in this region as ~ 5 cm RMS (see Section 3.2), while SEASAT is usually rated at ~ 13 cm RMS.

At the longest wavelengths, note how Fu's power level decreases at wavelengths longer than 1000 km. Fu attributed this decrease to his use of a quadratic trend removal, rather than the linear one used herein. Even without this power drop, the SEASAT regional spectrum is still somewhat lower in the mid to long wavelengths compared to those of GEOSAT. Some of this difference may be attributed to the fact that Fu's data had all corrections applied, while only ocean tide was removed from the GEOSAT data. Most of the difference in power, however, is due to Fu's use of only 24 days of SEASAT repeat

data; which is all that was available to him. Over such a short period of time, much of the long wavelength mesoscale variability simply cannot be seen, and so power levels at those long wavelengths will be lower than when measurements cover a longer time span. The lower powers at long wavelengths led Fu to fit a k^{-1} slope to the ocean variability spectrum in the northeast Pacific from 1000 to 100 km. Using the GEOSAT data available over some 10 months, however, one sees that the spectrum is actually closer to behaving as $k^{-1.5}$ in this wavelength range. As more GEOSAT repeats become available, oceanographers may be able to find some length of time beyond which the ocean variability spectrum does not change with increased time. This discovery would aid in defining the "mean" state of the ocean - a problem which has heretofore eluded solution.

As was shown in Section 3.2, the peak at around 130 km seen on the GEOSAT arc 293 wavenumber spectrum is due to geoid contamination. Similar analysis confirms that this contamination is also the cause of the peak at a slightly shorter wavelength found on the arc 209 spectrum. Fu's regional spectrum appeared to have a small peak at ~ 130 km as well, though it is difficult to tell, as that spectrum was plotted amidst 4 others. In any case, there is no indication in Fu's results of a peak at 130 km of the magnitude seen in the GEOSAT spectra. This is not unexpected, however, as Fu interpolated for sea surface heights alongtrack using a cubic spline, and so did not incur alongtrack geoid contamination (the lesser crosstrack errors caused by the ± 2.5 km SEASAT repeat tracks would explain any small peaks at wavelengths near 130 km).

Additional information about both the ocean and the altimeter data may be gained from comparing the two GEOSAT spectra. Note how, at wavelengths longer than ~ 200 km, the arc 209 power is noticeably greater than the arc 293 power. There are three possible reasons for this. First, the environmental errors which are not corrected for may be more severe along arc 209. This seems unlikely, as one would expect, if anything, greater environmental variability near the California and Alaska coastal regions than in the middle of the Pacific. Second, arc 209 may be an area of greater mesoscale variability than

arc 293. Figure 3.13 shows these two arcs plotted on the mesoscale variability map of Cheney et al. (1983), which was compiled from SEASAT repeat track data. Even after truncating the northern part of arc 209 (due to geoid contamination), it still appears that this arc covers a region of slightly higher oceanic activity than arc 293. This is especially the case northeast of Hawaii, where arc 209 passes quite close to the higher variability region surrounding the Hawaiian islands. An example of this variability may be seen near 25°N on a number of the arc 209 difference profiles (figure 2.17).

The third possible reason for the difference in power between arcs 209 and 293 is due to the ocean tide and its correction. As shown in Section 2.6, the aliasing of this phenomenon into the arc 209 mean caused increased variability in its difference profiles. Additionally, as the behavior of the sample standard deviation indicated before and after making the GDR Ocean Tide correction to arc 209; it is quite possible that the ocean tide is not as well modelled along this arc as it is for arc 293. Section 2.6 indicated how poor modelling of a correction would increase the difference profile variabilities, which would in turn raise the power density in the applicable wavelengths (the mid to long ones, in this case).

Overall, the GEOSAT-derived wavenumber spectra agree very well with the regional spectrum of Fu. As just seen, spectra of this sort are valuable not only in indicating the presence and level of mesoscale activity; but also in spotting areas for improvement in the altimeter product. It should be noted that oceanic wavenumber spectra of the scope and accuracy shown here are nearly unobtainable with conventional hydrography, which is better suited to taking repeated measurements in a limited area. Continued oceanic coverage by GEOSAT and follow on altimeters will provide additional information on oceanic activity in the wavenumber domain.

Variability as a Function of Position

The other domain within which GEOSAT provides valuable information on oceanic mesoscale variability is the frequency domain. That is, rather than investigating how the

sea surface height changes alongtrack (as was done in the prior subsection), one may ask how it varies with time at a given location. Such a calculation was performed by Cheney et al. (1983), using the same SEASAT repeat-track data as Fu.

Cheney et al. used a collinear processing scheme on SEASAT arcs divided worldwide into 2000 km long segments. Most geophysical phenomena were corrected for, including the delay of the radar pulse due to the ionosphere and troposphere (both wet and dry components), tidal effects, and electromagnetic bias. The data was smoothed by fitting a quadratic curve to every eight successive 1/sec data points, with iterative outlier rejection. The resultant curves, centered on each data point, also allowed for alongtrack interpolation of sea surface height. All repeats on each arc segment were processed in this way and a mean profile was formed on each segment from their averages. Difference profiles were then calculated, with linear detrending being used to reduce the orbit error. Due to the alongtrack interpolation of sea surface height, the set of ~8 difference profiles for each arc segment had their 1/sec values aligned to be as close as possible to one another - greatly reducing geoid contamination. RMS variability at each 1/sec aligned point could then be determined by calculating the standard deviation of the corresponding sea surface heights on the 8 difference profiles. The resultant set of variabilities, determined approximately every 7 km on the SEASAT groundtracks, were then gridded using a bilinear modelling function. Cheney et al.'s subsequent map of mesoscale sea height variability is reproduced in figure 3.13. The overall map is remarkably consistent with what is independently known of the oceans, and so is valuable for comparison with the GEOSAT data.

Five GEOSAT arcs were chosen for comparison with the results of Cheney et al. for the northeast Pacific. They were arcs 321, 293, 265, 237, and 209, spaced at an approximate 700 km interval from the California coast west to Hawaii. These arcs are also indicated on figure 3.13. On each arc, RMS variability as a function of latitude was determined by calculating the standard deviation of the 18 sea surface heights available there from the difference profiles (only 14 profiles were used for arc 209). To reduce short

wavelength jitter in the variability plots, three consecutive sea surface heights were averaged together around each chosen latitude before computing the standard deviation. The results of the GEOSAT variability calculations appear in figure 3.14. The arcs are arranged from top to bottom going westwards through the test area. As a reminder, the GEOSAT data used to create these plots was corrected only for ocean tide and was not interpolated alongtrack, although the 3 point block average was applied to reduce noise.

Comparing figures 3.13 and 3.14, one sees that the GEOSAT data agrees very well with the results of Cheney et al. in mapping the qualitative picture of mesoscale variability in the northeast Pacific. The GEOSAT variabilities do tend to be higher, though, for a number of reasons: First, the SEASAT arc segments were less than half as long as those used in this thesis, resulting in smaller orbit error in its difference profiles (as well as more limited wavelengths within which to spot oceanic variability). Second, Cheney et al.'s alongtrack data interpolation significantly reduced their geoid contamination (although SEASAT, with its ± 2.5 km repeat, would have a larger crosstrack component of this effect than GEOSAT). Third, SEASAT's SMMR allowed for computation of a coincident wet tropospheric correction to its sea surface heights. Fourth, the SEASAT results were determined from only 24 days of data, over which time oceanic variability would be less than for the 307 days used in the GEOSAT calculations. Fifth, Cheney et al.'s gridding scheme resulted in reduction of variability for narrow current systems, such as the Alaskan and Californian ones.

Quantitative estimates of the effects on variability calculations caused by these differences may be made as follows: Tai (1988) derived analytically the average error committed in representing the orbit error along a groundtrack segment by a bias and tilt. For a known RMS bias difference between the various repeats on an arc, and a given arc length (expressed in degrees relative to a 360° earth circumference), his table 1 gives the RMS error of the final sea surface height variability calculations. Using GEOSAT arc 209, with an arc length of 3600 km (remember that arc 209 was truncated due to geoid

contamination), and an RMS bias difference over 14 repeats of 101 cm, Tai's table gives a 1.18 cm RMS error in the arc 209 variability estimates. If Cheney et al.'s 2000 km arc length was used instead, the RMS error would be only 0.38 cm. Each of these errors reflects the tendency of the difference profiles to overestimate oceanic variability when orbit error remains in them - the longer arcs used in the GEOSAT calculations thus overestimate the oceanic variability by $(1.18^2 - 0.38^2)^{1/2} = 1.18$ cm more than shorter arcs would have (this corresponds to a variance difference of 1.25 cm^2). Now refer again to figures 3.13 and 3.14. Integrating the location-dependent variabilities along arc 209, the GEOSAT-determined variability is 7.0 cm, while the Cheney et al. variability appears to be about 3.5 cm. The difference in variance between the two estimates is thus $(7.0^2 - 3.5^2) = 36.8 \text{ cm}^2$. The portion of this difference which may be attributed to the residual orbit error difference just calculated is only about 3%.

The contribution of alongtrack geoid contamination to the difference in variance between the GEOSAT and SEASAT results may be estimated in the following way: The spectral peak seen at wavelengths of about 130 km on the mean spectra of the various GEOSAT arcs was shown in Section 3.2 to be largely due to geoidal effects. Using the arc 209 mean spectrum in figure 3.12, the variance of this peak is calculated to be 0.72 cm^2 ; which accounts for some 2% of the variance difference between the GEOSAT results and those of Cheney et al.* Since crosstrack offsets are less than the alongtrack ones, the crosstrack geoid contamination contribution to the variance calculations is negligible in this case (remember also that the geoid is changing most rapidly with location in the alongtrack direction for arc 209).

* Note that the geoid variance estimate comes from alongtrack calculations of sea surface height, while the arc 209 variance estimates are temporal in nature. Meaningful comparisons of spatial and temporal variance may be made under the assumption that the ocean is essentially homogeneous in space and time (if the ocean is completely homogeneous, spatial and temporal variance are equivalent). This is a fairly good assumption for the test area, which is largely free of major current systems and their accompanying inhomogeneity.

Assuming that the SEASAT SMMR provided an accurate wet tropospheric correction for Cheney et al., a significant portion of the higher variance of the GEOSAT results may be attributed to not making any such correction for the latter data set. This portion may be roughly estimated by calculating the variance of the wet FNOC correction along the GEOSAT repeats on arc 209, from table 2.2 (see Section 3.4 for the methodology). This calculation gives a wet-tropospheric variance of 21.14 cm^2 , which accounts for about 57% of the GEOSAT-SEASAT variance difference.

The fact that the GEOSAT data spans a longer time than the SEASAT data allows GEOSAT to see more of the low-frequency oceanic variance than SEASAT. Using the tide-free power spectrum of Honolulu sea level from 1938 to 1957, calculated by Munk and Cartwright (1966), the increased sea surface height variance seen over 307 days (as opposed to 24 days) is graphically estimated as 13 cm^2 . This extra oceanic variance seen by GEOSAT explains some 35% of its difference with the SEASAT variances calculated by Cheney et al.

The reduction of variance in strong current regions caused by Cheney et al.'s gridding technique is difficult to estimate; but when the variance is integrated alongtrack, the effect should be minimal. Overall, the other four calculated effects account for some 97% of the difference in integrated alongtrack variance between GEOSAT arc 209, and the corresponding results of Cheney et al. This is outstanding agreement.

Returning to qualitative results, it is apparent that the two altimeters provide a very consistent view of the northeast Pacific. For example, all five GEOSAT arcs pick up the variability of the Alaskan current (seen in figure 3.13) at their northern ends, although arc 293 almost misses it as the current veers into the Gulf of Alaska. GEOSAT arcs 237 and 209 also show the increasingly southward location of the Alaskan current as one looks further west along the Aleutian island chain. Similarly, the GEOSAT arcs all see slightly higher variabilities in the south; at the northernmost reaches of the North Equatorial Current

system. In addition, arc 209's southern segment (up to $\sim 38^\circ\text{N}$) indicates the additional region of high oceanic variability near the Hawaiian islands depicted by Cheney et al.*

The latitudes covered by the middle portions of the GEOSAT arcs provide more information about variability in the northeast Pacific. Refer to figure 3.14 and note the region of high variability around 38°N on arc 321, corresponding to the most energetic portion of the California current. In addition, observe the ability of GEOSAT to pick up Cheney et al.'s isolated region of slightly elevated variability (>3 cm RMS), corresponding to the central segment of arc 265. The GEOSAT arcs to either side of arc 265 do not show this elevated signature, which is consistent with Cheney et al.

Each of the GEOSAT variability plots of figure 3.14 may be integrated alongtrack to determine its temporal RMS variability (as was done for arc 209). The following variabilities are determined: Arc 321-7.53 cm, arc 293-5.27 cm, arc 265-6.76 cm, arc 237-6.76 cm, and arc 209-7.00 cm (the figure for arc 237 is slightly high, due to the residual spikes in its difference profiles). GEOSAT data thus describes a northeastern Pacific with high temporal variability at its eastern California boundary, a relatively quiet central portion, and increased variability again in the west. This qualitative picture is consistent with Cheney et al. and the work of others using non-altimetric sources (see Wyrki et al. [1976]).

It may be noted that oceanic quantities of interest such as the eddy kinetic energy can also be calculated with the collinear scheme. Here, the sea surface slope variability is computed as a function of position, and then converted to surface current variability (from which eddy kinetic energy arises) through the geostrophic equations. Menard (1983), for

* The GEOSAT difference profiles from which the plots in figure 3.14 originated were examined to ensure that regions of high variability could not have been due to geoid contamination, orbit error, etc. The only regions of falsely high variability which were noted, appear as peaks at 31°N and 45°N on arc 237, and are due to data spikes not fully eradicated in the editing process.

example, performed these calculations for the Gulf Stream and Kuroshio Current regions using the SEASAT repeat-track data.

3.4 ERROR BOUNDS ON GEOSAT VARIABILITY CALCULATIONS

The integrated temporal variabilities for the five GEOSAT arcs were shown to agree in a qualitative manner with a priori knowledge of the northeastern Pacific. An important question to answer, however, is what are the error bounds on these variabilities? That is, do the non-modelled and poorly-modelled effects discussed in earlier sections cause enough uncertainty in the final GEOSAT results to warrant concern? At the two extremes of the wavenumber range, the answer is no. Instrument noise is largely averaged out, and residual orbit error for a 4400 km long arc is only some 1.80 cm RMS, after bias and tilt removal (using Tai's [1988] table with a typical RMS bias difference between repeats of 1 m). Within the mid wavelengths, the effects of geoid contamination on the final variances of a typical arc were estimated as 0.72 cm^2 , giving an RMS error of only 0.85 cm. These errors are not significant compared to the typical temporal variability estimates of 5+ cm (RMS).*

The remaining causes of error in the arc variability estimates stem from the corrections studied in Chapter 2. Of these corrections, the ocean tide was usually the most energetic, and was applied in the final editing scheme. Its error may be roughly determined in the following way (using arc 209 as the example): Observe from table 1.2 that the ocean tide correction error has a magnitude 1/10 of the correction itself. From table 2.2, the effect of the ocean tide correction upon the actual difference profiles can be seen in their change in variance after making that correction. Using only the 7 repeats marked with an asterisk (denoting those repeats where the OTIDE correction had a significant effect on the variance of the difference profiles), the average change in difference profile variance caused by the

* Recall that Tai's calculations were for the average residual orbit error. The maximum error seen on a particular difference profile might be greater.

OTIDE correction is 31.87 cm^2 .^{*} Assuming the error is 1/10 of the correction, then the GEOSAT OTIDE error variance is 3.19 cm^2 . This corresponds to an ocean tide-induced error of 1.79 cm (RMS) in the arc 209 variability estimate, and is not significant.

Three other corrections were seen in Chapter 2 to be energetic enough to be a problem in any GEOSAT results. These involved the electromagnetic bias, inverted barometer, and wet troposphere phenomena. Since these effects were not corrected for in the editing scheme used here, their total effect on the difference profiles must be considered - not the residual error after correcting for them (as in the ocean tide). Using the method described in the previous paragraph, the average change in difference profile variance caused by these phenomena for arc 209 are as follows: electromagnetic bias - 34.42 cm^2 , inverted barometer - 30.80 cm^2 , and wet FNOC - 21.14 cm^2 . These correspond to errors in the arc 209 variability estimate of 5.87 cm, 5.55 cm, and 4.60 cm (RMS), respectively. Recall from Chapter 2, however, that the simple inverted barometer correction tends to overcorrect the sea surface heights, while the wet FNOC correction tends to undercorrect them. Thus, the error in the arc 209 variability estimate due to no IB correction being made is likely smaller than 5.55 cm, while the error due to not making a wet troposphere correction is probably larger than 4.60 cm. In any case, these three effects can be a significant source of error in any GEOSAT oceanic variability estimates.

The reader should remember that the electromagnetic bias, inverted barometer, and wet troposphere error estimates given here are rough, and are biased towards the worst case. In practice, the phenomena themselves can usually be separated from oceanographic signals in the difference profiles, with knowledge of their spatial and temporal characteristics - as demonstrated in Section 3.2. Nevertheless, the manual separation of non-oceanographic signals from GEOSAT difference profiles is a tedious process at best,

^{*} No attempt is made to distinguish tidal phases, or whether the OTIDE correction increased or decreased the variance - this is just a zero-order estimation of the magnitude of the correction. It is assumed that any model error is uncorrelated with the difference profiles.

and rather defeats the goal of near real-time sampling of the oceans. Therefore, further work is called for in correcting these three major sources of error, as already seen in Section 3.2.

3.5 SUMMARY AND CONCLUSIONS

A region of the northeast Pacific, from 20° to 55°N and 115° to 180°W, was chosen within which to evaluate and use altimetric data from the U.S. Navy Geodetic Satellite GEOSAT. A 4400 km satellite track (arc 82) spanning the region was used to verify the zero order accuracy of the major GEOSAT geophysical data record (GDR) channels; including time, position, orbit height, sea surface height, geoid height, significant wave height, tidal values, and environmental corrections. No discrepancies in the data were noted, and the information gained in the accuracy check allowed for the presentation of a concise GEOSAT error budget, listed in table 1.2. While the available GEOSAT data looked good, a number of gaps in altimeter coverage were noted, especially in the descending passes. These gaps limited the choice of arcs for later processing.

The effects of applying various geophysical corrections to the GEOSAT sea surface heights were investigated using a collinear processing scheme: For a given repeat pass, bad data points were edited/smoothed, the low order Rapp geoid was removed, and the resultant alongtrack sea surface height profile was detrended of bias and tilt (to reduce orbit and other long wavelength errors). All repeat passes on a chosen arc were processed in this way and then averaged together to form a mean sea surface height profile for the arc. No interpolation for height between alongtrack data points was done, although the various repeats were slid to be within $\pm\Delta/2$ of gridded reference latitudes (where $\Delta = 6.7$ km). This was performed to reduce geoid contamination.* The mean profile was then subtracted from each repeat profile on the arc to create a set of difference profiles, which highlighted the variable features of the ocean.

* Regions of very high spatial geoid variability were too much for the sliding scheme to handle on portions of arcs 82 and 209, so these regions were not processed.

The various GEOSAT corrections were examined with the collinear scheme by individually applying them to the repeat profiles on three test arcs (#'s 82,209,293), and observing their effect on the alongtrack RMS variability of the resultant difference profiles. Derivations using the theory of coherent and incoherent power showed that a well-modelled correction would tend to decrease the alongtrack variability when applied, while a poorly modelled one would increase it. Corrections which varied only slightly over the length of the test arcs (~4400 km) would have very little effect on the difference profile variabilities.

The results from applying the GEOSAT GDR corrections to the three test arcs indicated that only the ocean tide, electromagnetic bias, and inverted barometer corrections varied enough over the arc length to warrant using them to adjust the sea surface heights. Referral to satellite maps of integrated atmospheric water vapor, in conjunction with difference profiles, indicated that the true wet tropospheric correction could also be significant; but the GEOSAT wet FNOG and wet SMMR corrections did not reflect it. Of the three significant GDR corrections, the electromagnetic bias and inverted barometer effects were shown to be (negatively) correlated with one another, through the atmospheric pressure. The dependence of a static inverted barometer response upon the temporal and spatial scales of the atmospheric forcing was demonstrated, which explained the failure of a simple model to correct for it. Therefore, no correction for the inverted barometer effect was made, and the resultant contamination of the difference profiles by the atmospheric pressure prevented the GDR EM BIAS correction from working well, either. It, too, was therefore not recommended for application. The remaining ocean tide correction did work well enough to warrant its use, although the long alias period (~317 days) of its M2 component led to the recommendation of using multiples of 18 repeat cycles to form the arc mean profiles.

Spectral analysis indicated that a three-point block average of ocean tide-corrected sea surface heights would result in the loss of very little oceanographic information, and so was recommended to reduce short wavelength instrument noise and lessen computer

storage space requirements. The GEOSAT data used in the rest of the thesis had this averaging performed, was corrected for ocean tide, and used 18 repeat cycles worth of data.

A set of 18 difference profiles on arc 293 was investigated for mesoscale variability. The overall alongtrack variability on this arc was quite low, with the quietest difference profiles having an RMS variability of ~ 4.5 cm. This figure was suggested as a reasonable estimate of GEOSAT's working precision.

Oceanographic features could be found on the arc 293 difference profiles, but only after sifting through a variety of other signals. At scales of less than 100 km, the difference profiles were seen to be dominated by instrument noise. At scales from 100 to 500 km, geoid contamination was seen to be a problem, although the alongtrack gradient of the arc mean profile could be used to identify it. The electromagnetic bias and wet troposphere effects also significantly affected these length scales, but knowledge of their temporal variation allowed their signatures to be catalogued on the difference profiles. Scales longer than 500 km were seen to be dominated by altimeter errors, and no oceanographic features were noted within them. Oceanic mesoscale signals were seen in the 100 to 500 km range, however, and included a probable cold eddy lasting for 50+ days, with a horizontal extent of some 200 km and a surface dynamic expression of 10-15 cm.

Edited GEOSAT data from the area was then compared with other investigations of the region - mostly from SEASAT data. Mean alongtrack wavenumber spectra of oceanic variability for arcs 209 and 293 were compared with a regional variability spectrum of Fu (1983), with good overall agreement. Differences included slightly less system noise for GEOSAT, and higher power densities at long wavelengths in the GEOSAT spectra (mainly due to the longer time span covered by the GEOSAT data). These differences in power led to a $k^{-1.5}$ fit at wavelengths from 100 to 1000 km in the GEOSAT spectra; slightly steeper than the k^{-1} slope determined by Fu.

Sea surface temporal variability as a function of location was determined along 5 GEOSAT arcs for comparison with similar calculations by Cheney et al. (1983), who used SEASAT data. Qualitative agreement was excellent, with GEOSAT picking up the variability of the Alaskan, Californian, and North Equatorial currents, as well as the region of elevated variability near the Hawaiian islands. Absolute variability levels were higher for the GEOSAT results, due mainly to lack of a wet tropospheric correction and a greater span of covered time. These two factors accounted for some 92% of the difference in variance between GEOSAT and SEASAT calculations for one arc. The temporal variability as a function of latitude along each of the 5 GEOSAT arcs was then integrated alongtrack to estimate an overall temporal arc variability. These estimates showed elevated variabilities at the eastern and western boundaries of the test area, surrounding a quiet central region; which was consistent with independent knowledge of the northeast Pacific. Error bounds on the arc variabilities were estimated for arc 209; and the uncertainties in oceanic variability caused by the uncorrected electromagnetic bias, inverted barometer, and wet tropospheric effects were seen to be significant.

A number of areas for improvement in altimetric methods were noted through the course of the thesis: First, more accurate orbit determination is necessary to monitoring the ocean over longer length scales - currently, monitoring is limited to the relatively short arc segments over which simple detrending can be used. These long scales are the ones in which the "planetary" oceanic waves (Rossby and Kelvin) may be studied. Second, independent gravimetric geoids must be determined if there is to be much open in using satellite altimeters to study the mean oceanic circulation. Third, collinear processing should include interpolating for sea surface height between the 1/sec data points. A fair amount of GEOSAT data was unusable in this work due to the simple sliding scheme being unable to sufficiently reduce the alongtrack geoid error. In addition, geoid error had to be manually identified on a number of difference profiles, in order that it not be mistaken for oceanographic features. Alongtrack interpolation would alleviate much of these problems.

Finally, a call is made for continued improvement in error modelling and correction. A good frequency/wavenumber inverted barometer model would be a great asset to future altimetric studies. Radiometer measurements of integrated atmospheric water vapor, coincident with the altimeter measurement, are further desired for correcting the sea surface height data. Perhaps the bottom line to the necessity of having good corrections is that it allows data analysis to be more automated, as one then need not continually sift through difference profiles to remove unwanted features. The real attraction of satellite altimetry is its potential of providing accurate, near real-time sampling of the oceans, and anything which helps to realize that goal is to be pursued.

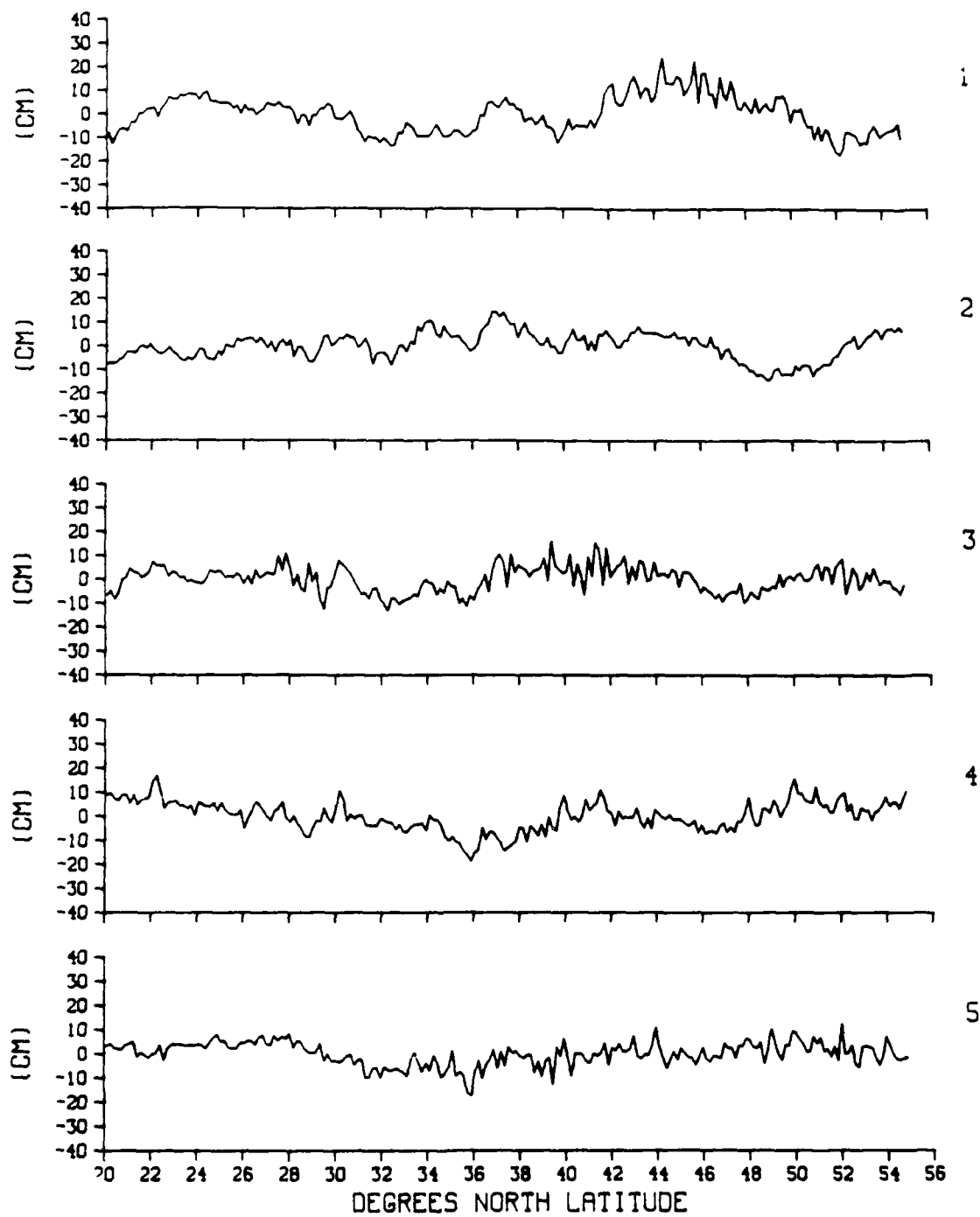


Fig. 3.1 Difference profiles along arc 293. Three-point block average and ocean tide correction applied.

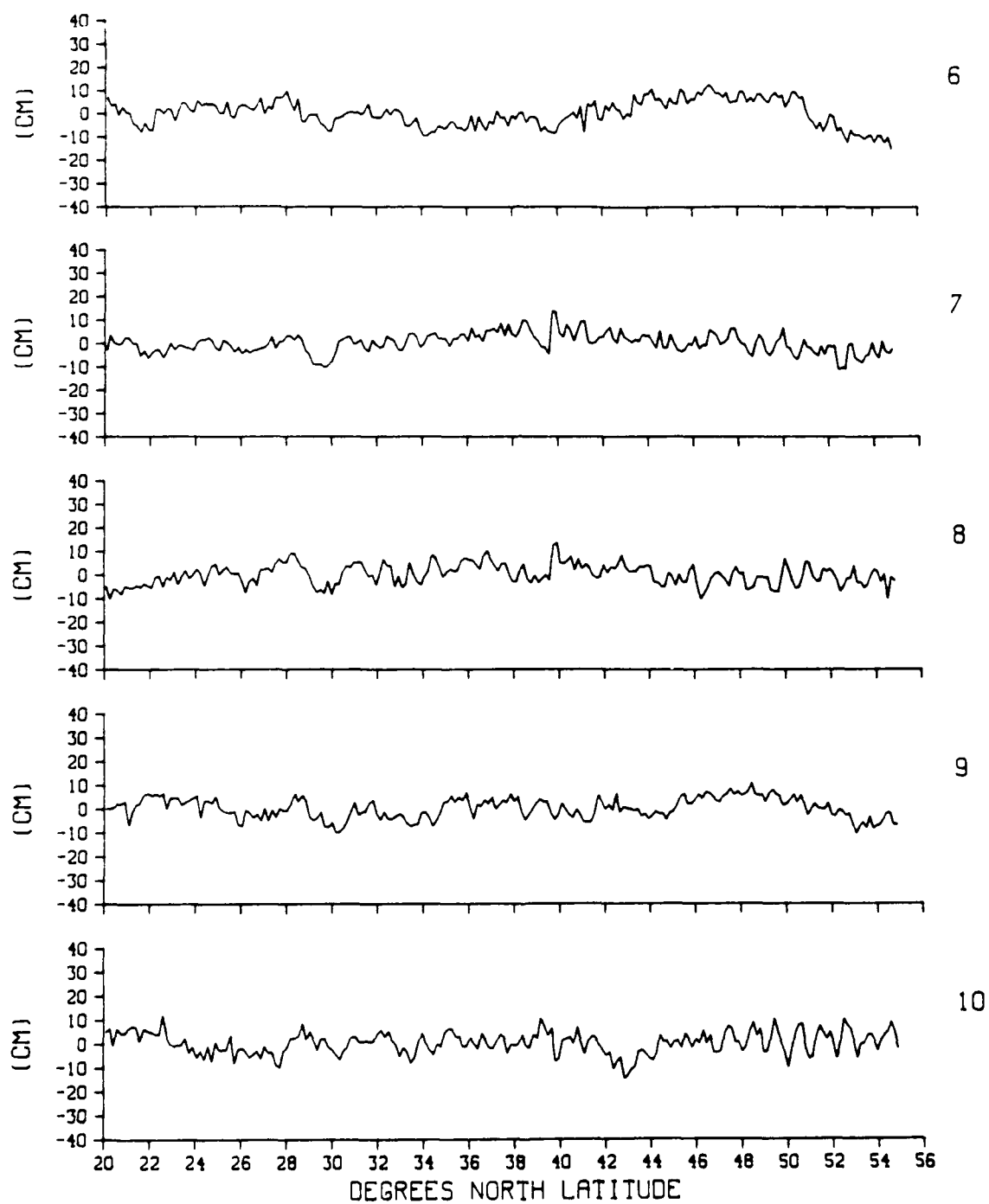


Fig. 3.2 Difference profiles along arc 293. Three-point block average and ocean tide correction applied.

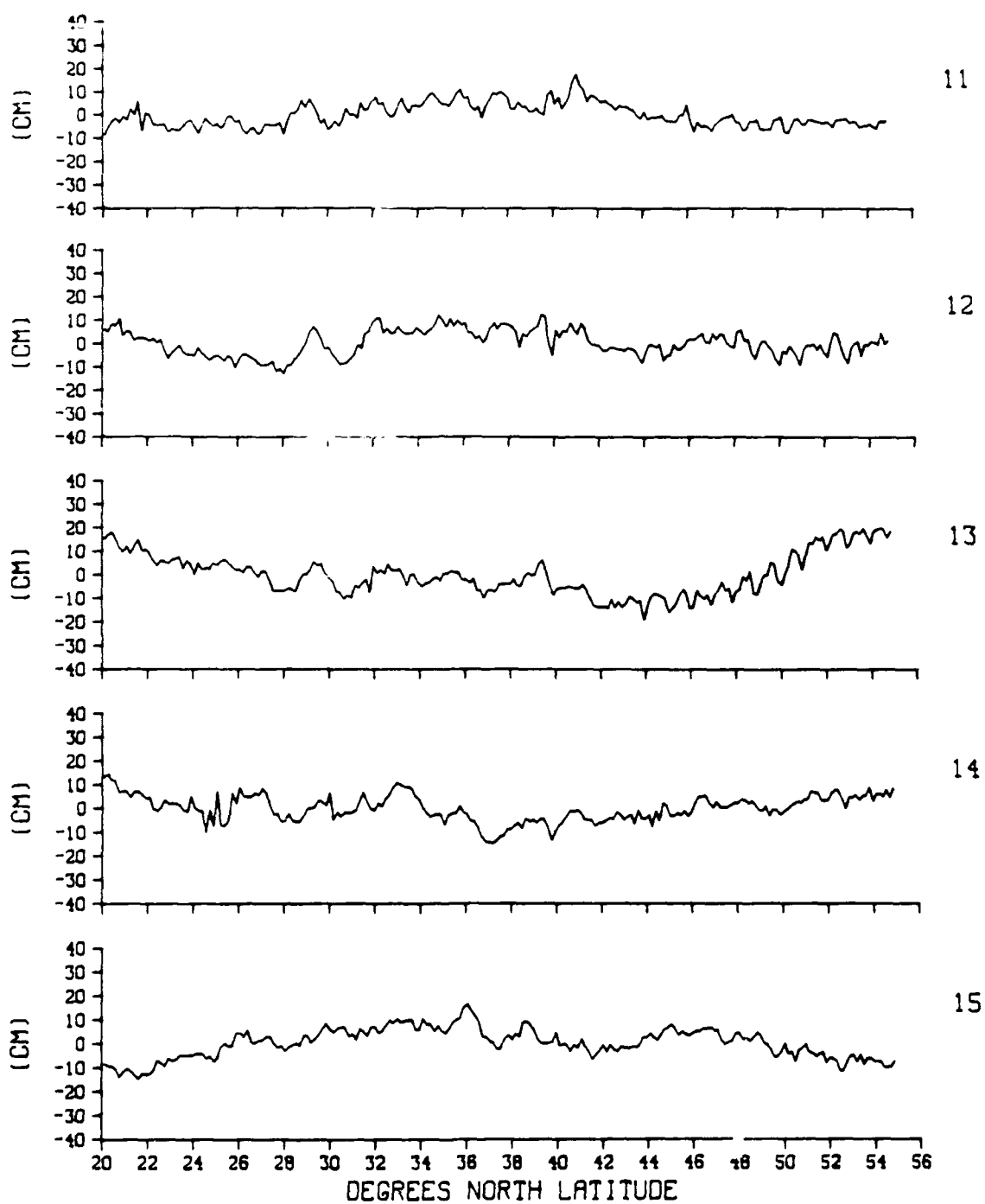


Fig. 3.3 Difference profiles along arc 293. Three-point block average and ocean tide correction applied.

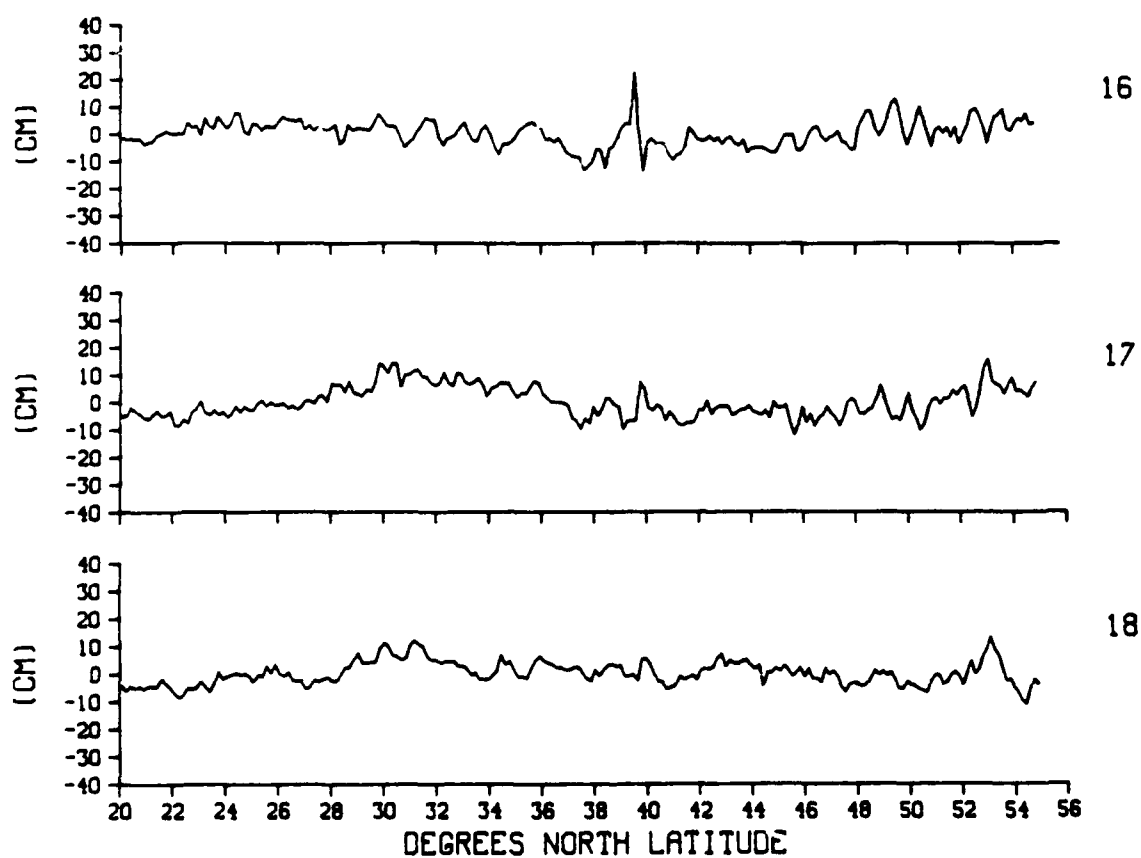


Fig. 3.4 Difference profiles along arc 293. Three-point block average and ocean tide correction applied.

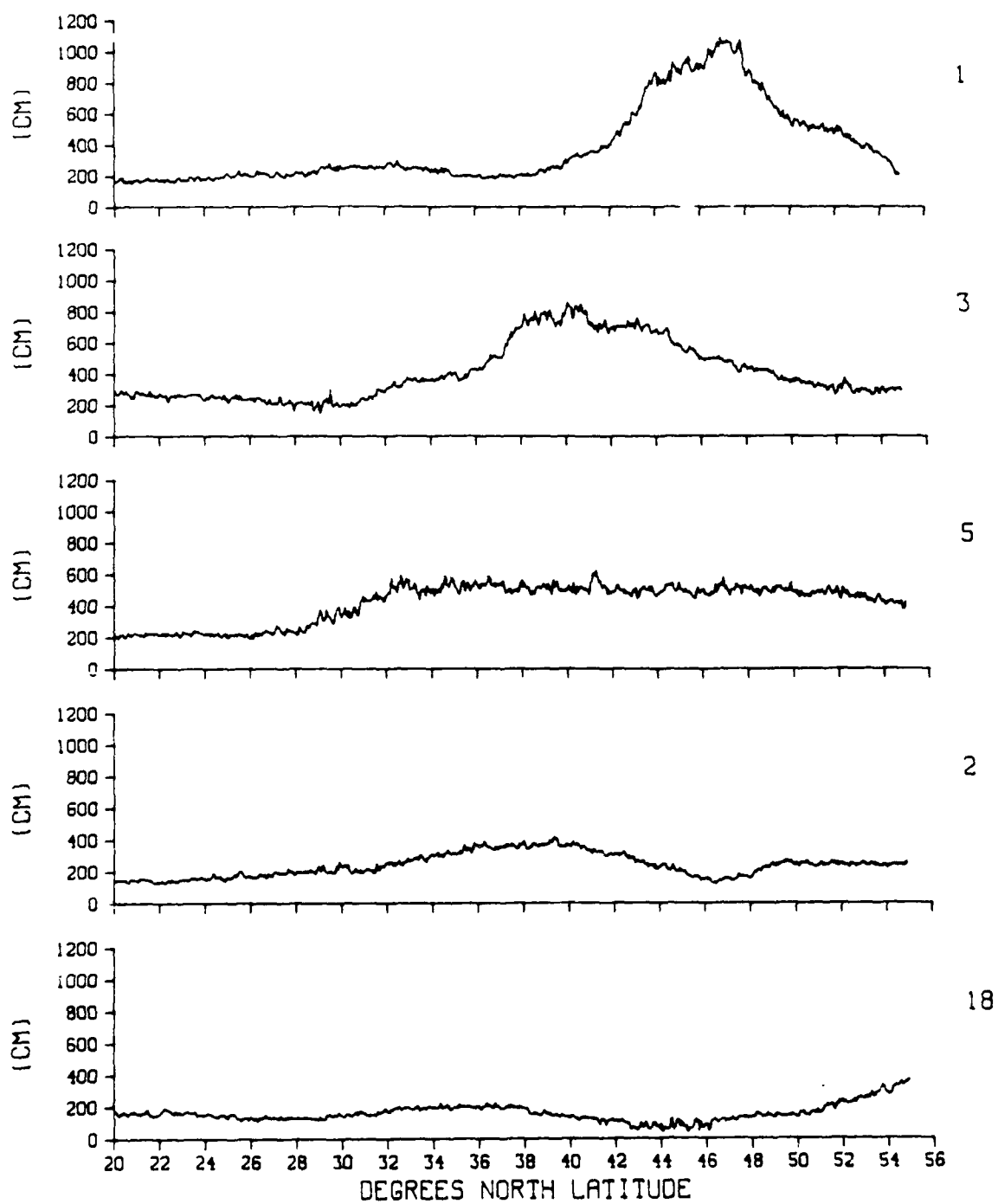


Fig. 3.5 Significant wave height along arc 293.

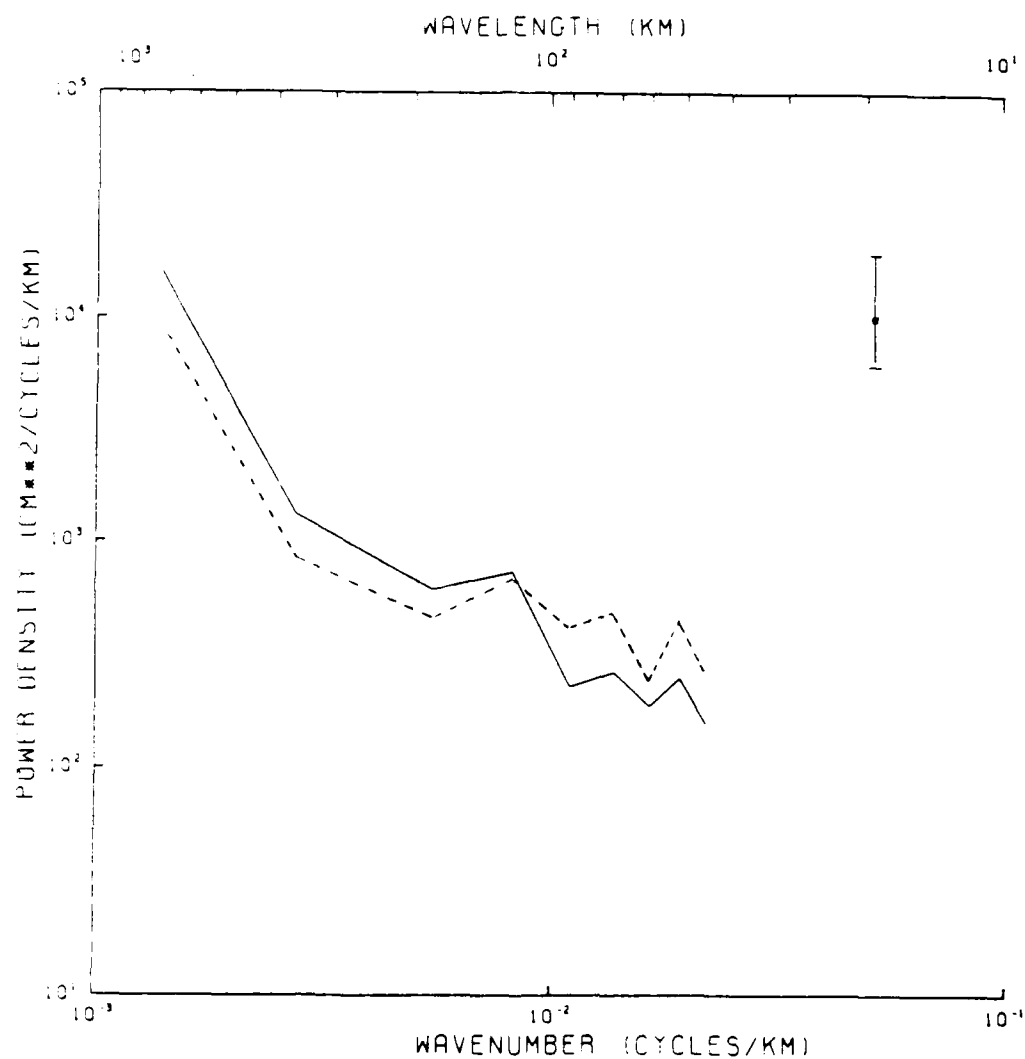


Fig. 3.6 Power spectra of the difference profiles for repeat 4 (solid line) and repeat 5 (dashed line) on arc 293. The cutoff at 40 km is due to the increased sampling interval caused by the three-point block average.

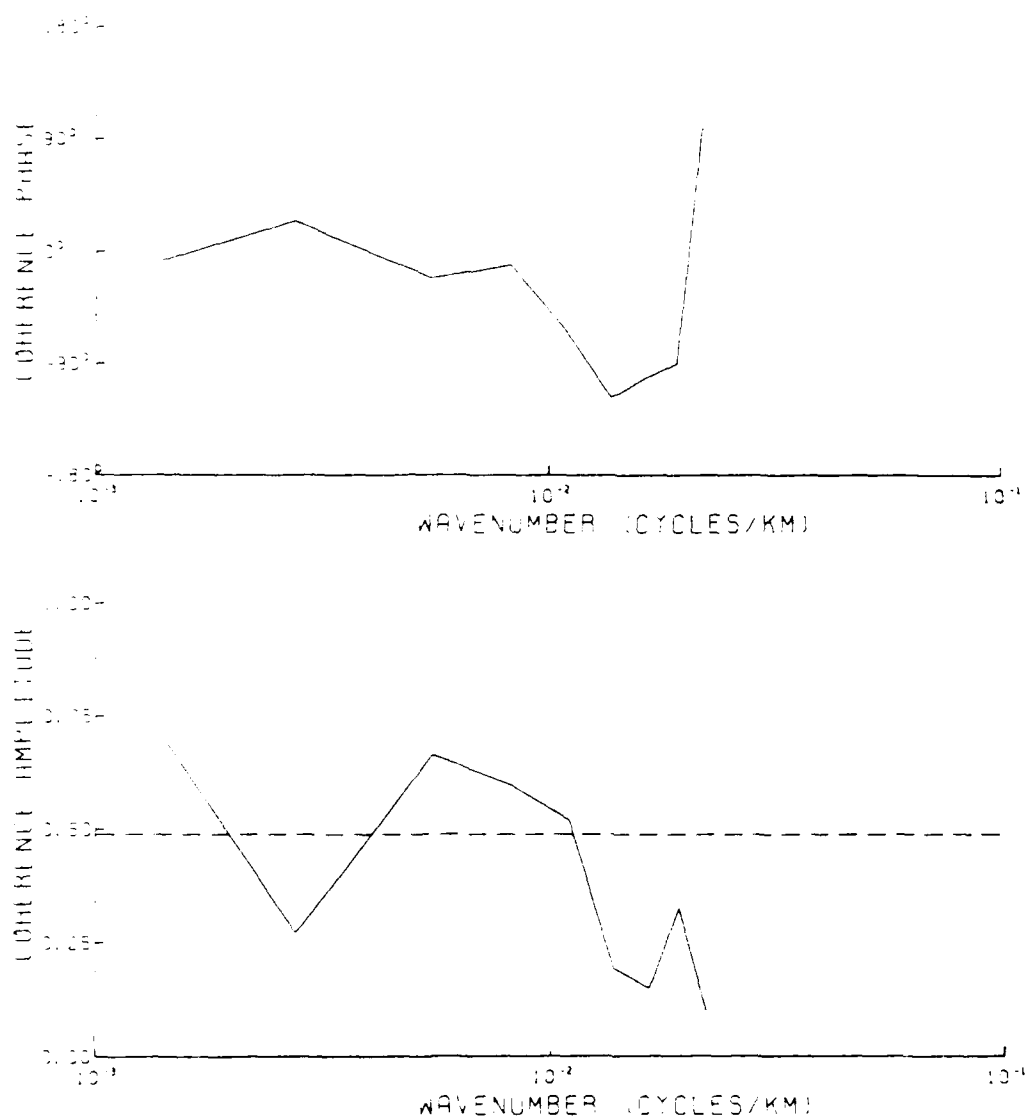


Fig. 3.7 Coherence phase and amplitude between the difference profiles of repeats 4 and 5 on arc 293. Note the lack of significant coherence at wavelengths shorter than 100 km.

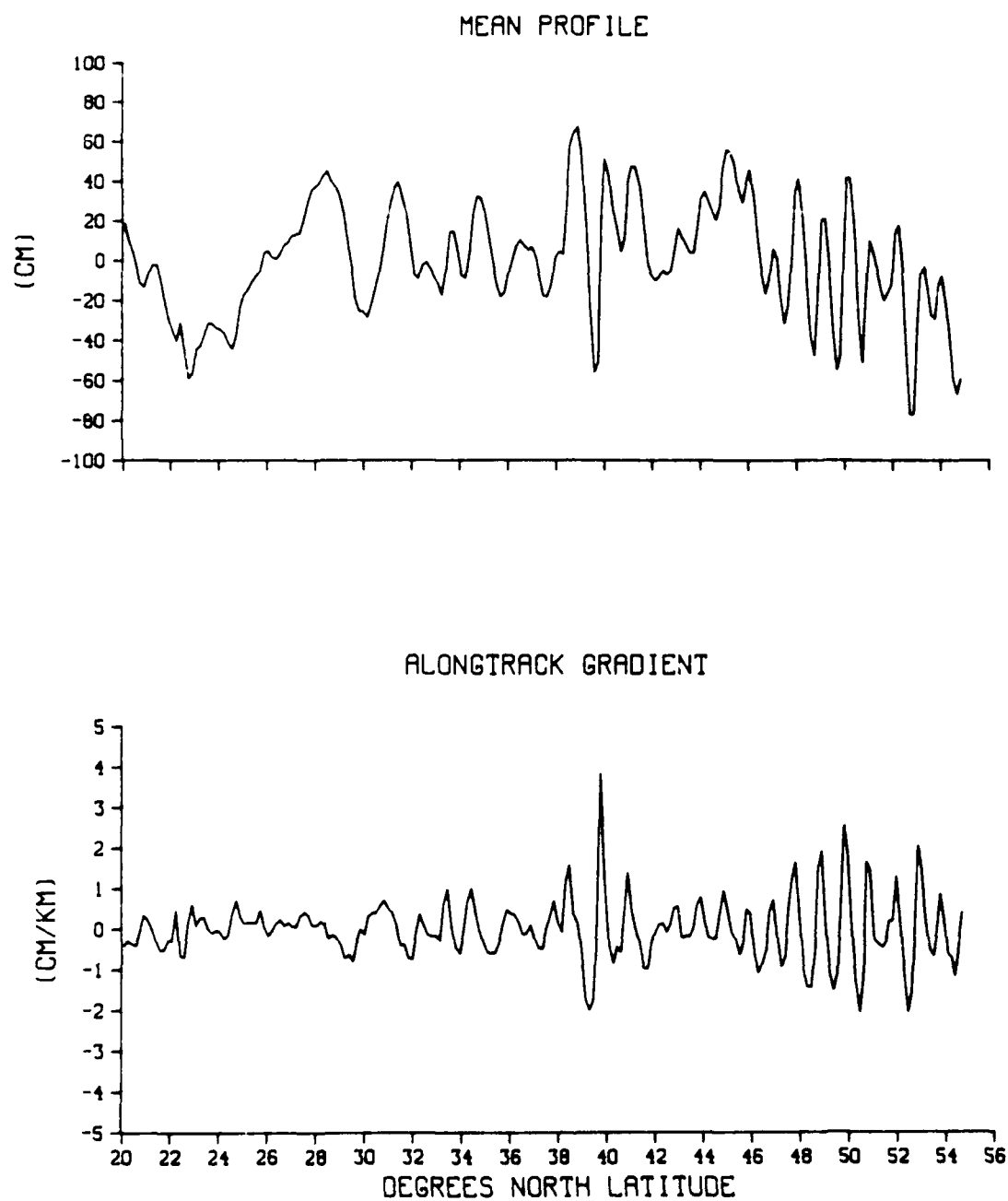


Fig. 3.8 Mean sea surface height profile and alongtrack gradient for arc 293. Three-point block average and ocean tide correction applied.

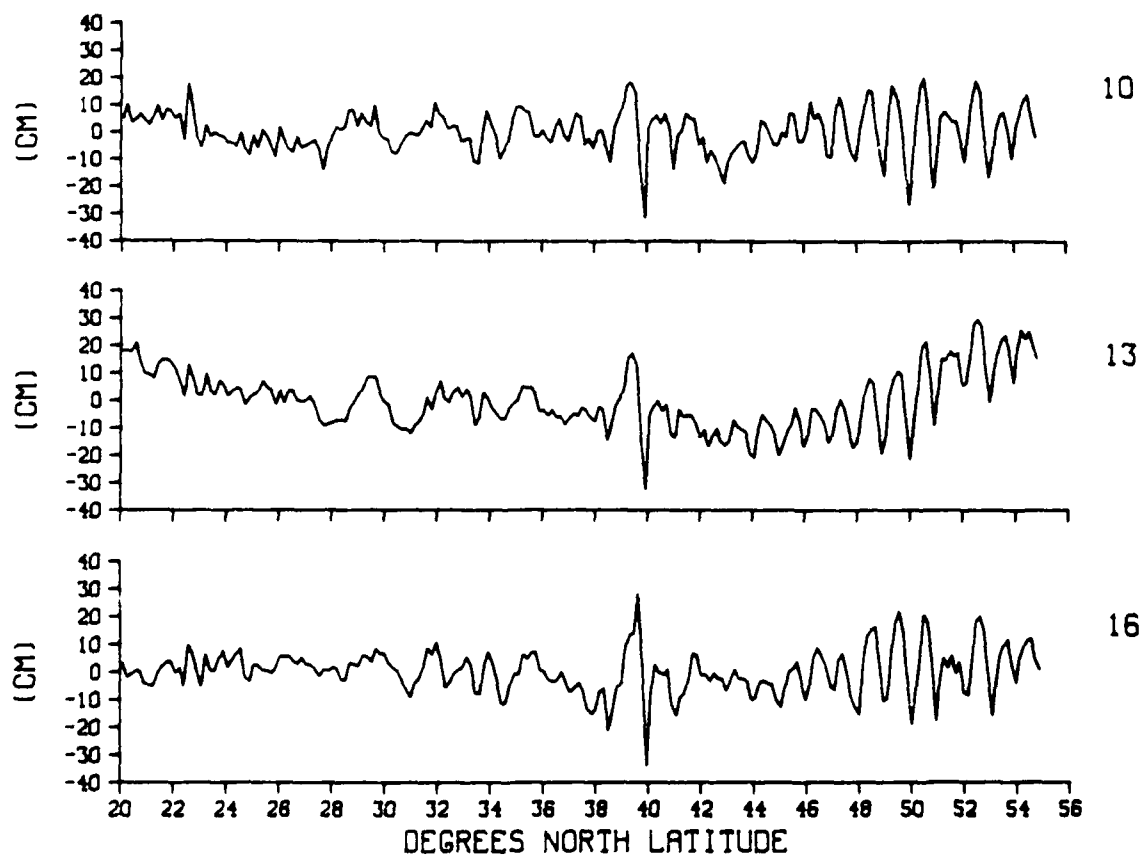


Fig. 3.9 Difference profiles along arc 293. Three-point block average and ocean tide correction applied. The passes from which the profiles originated were shifted south alongtrack by 6.7 km.

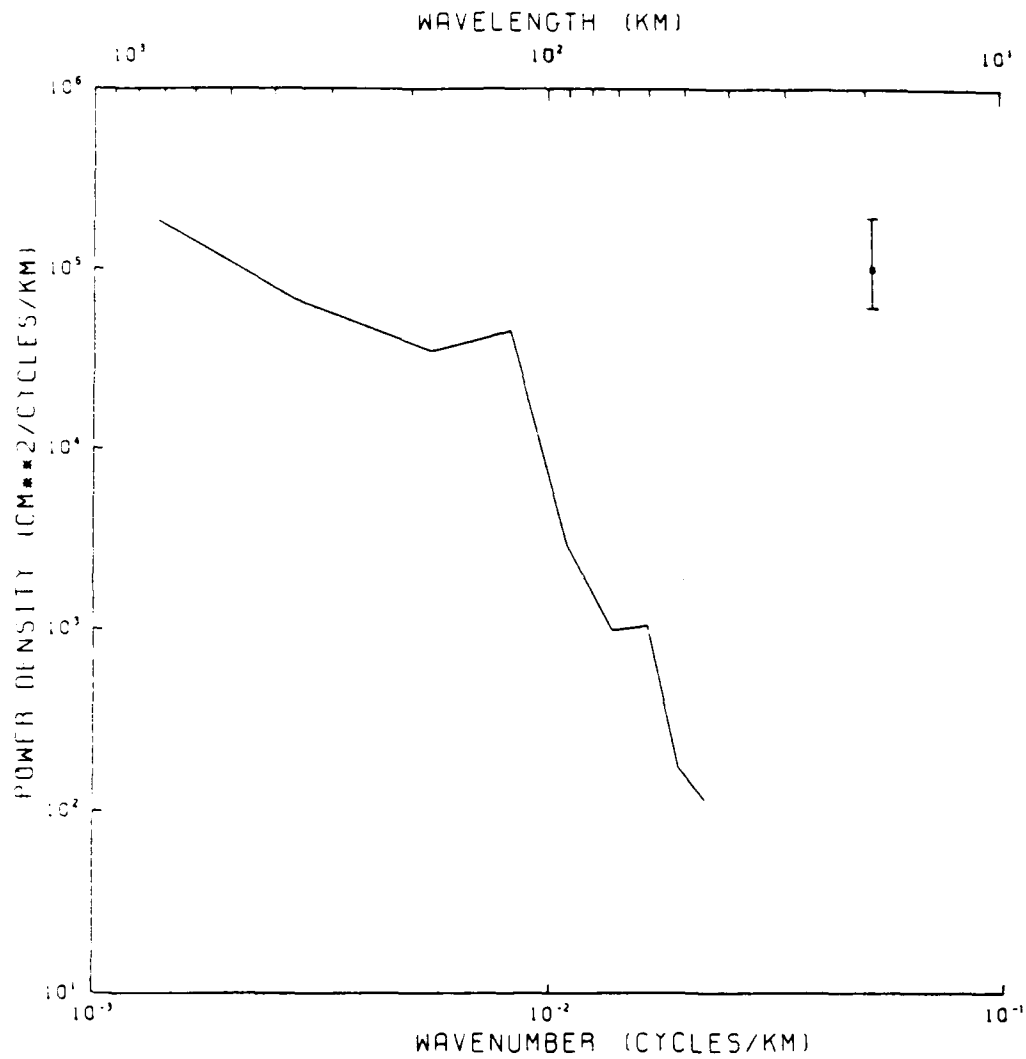


Fig. 3.10 Power spectrum of the mean sea surface height profile along arc 293. The peak at 130 km is due to geoid contamination.

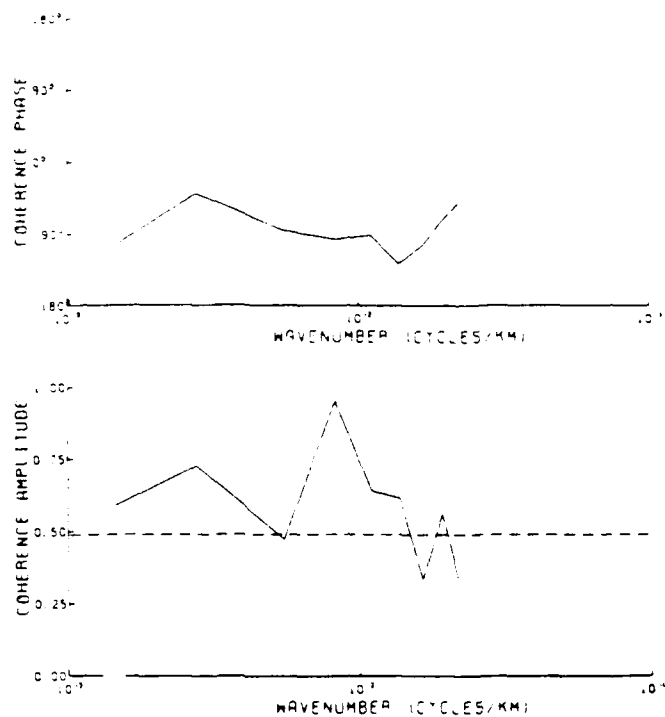


Fig. 3.11a Coherence phase and amplitude between the arc 293 mean profile and its difference profile for repeat 10. The high coherence at 130 km indicates that the geoid contamination seen in the mean profile has worked its way into the difference profile.

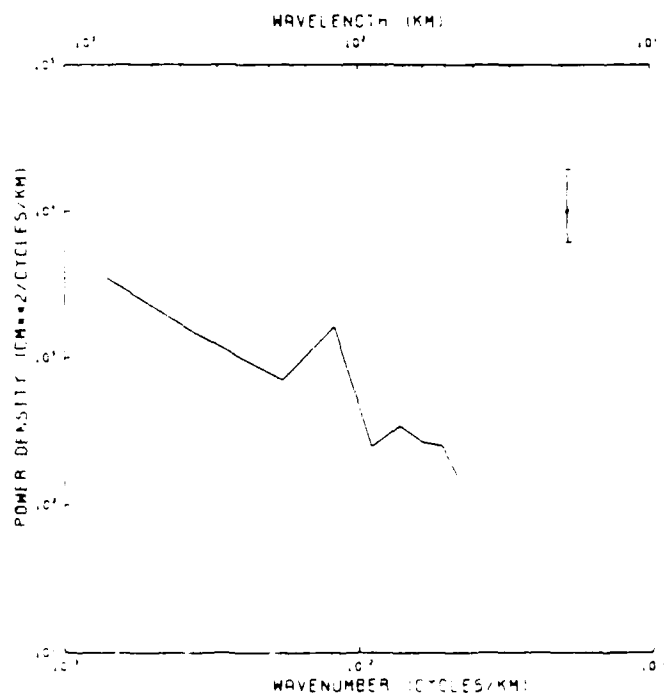


Fig. 3.11b Power spectrum of the difference profile for repeat 10 on arc 293. Note the significant geoid contamination at 130 km.

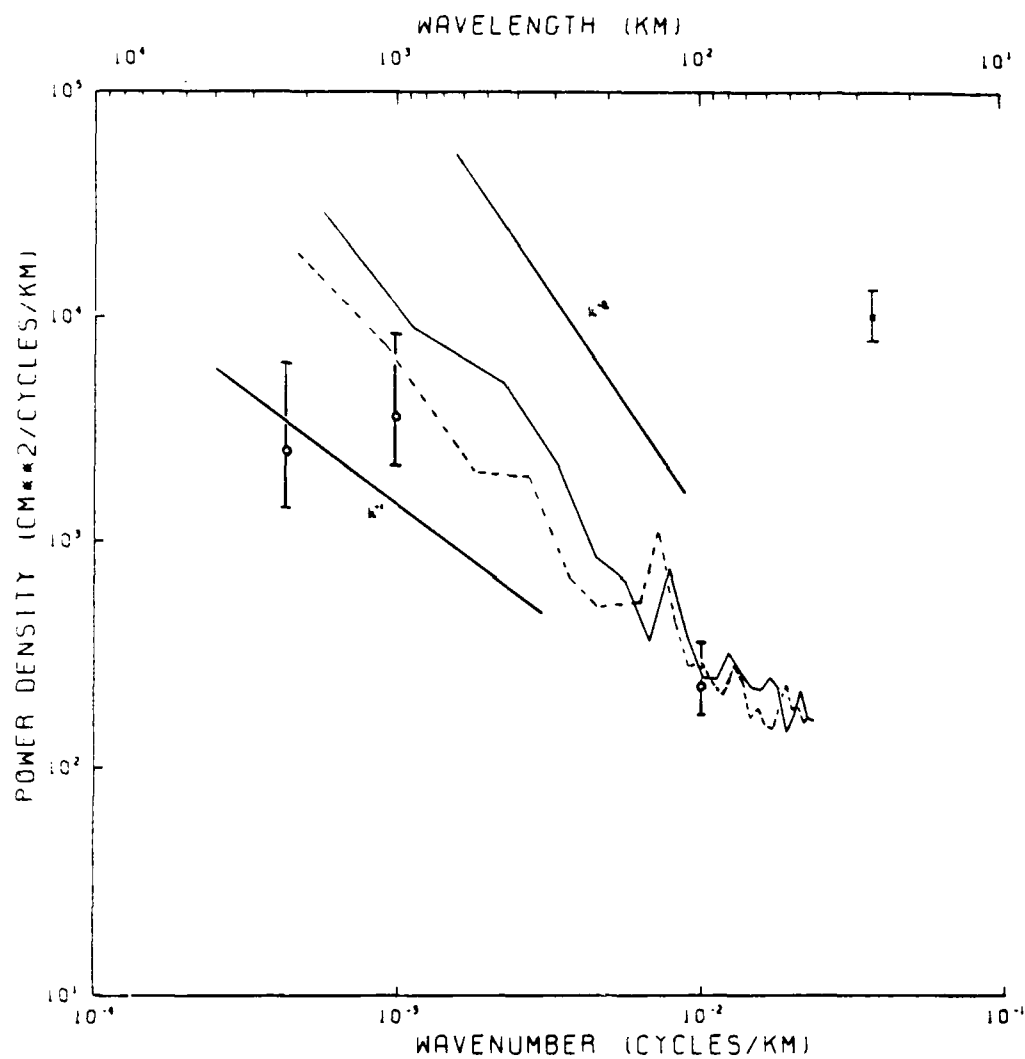


Fig. 3.12 Mean power spectra of the difference profiles of arcs 209 (solid line) and 293 (dashed line). The circles indicate values on a corresponding regional spectrum calculated by Fu (1983), using SEASAT data.

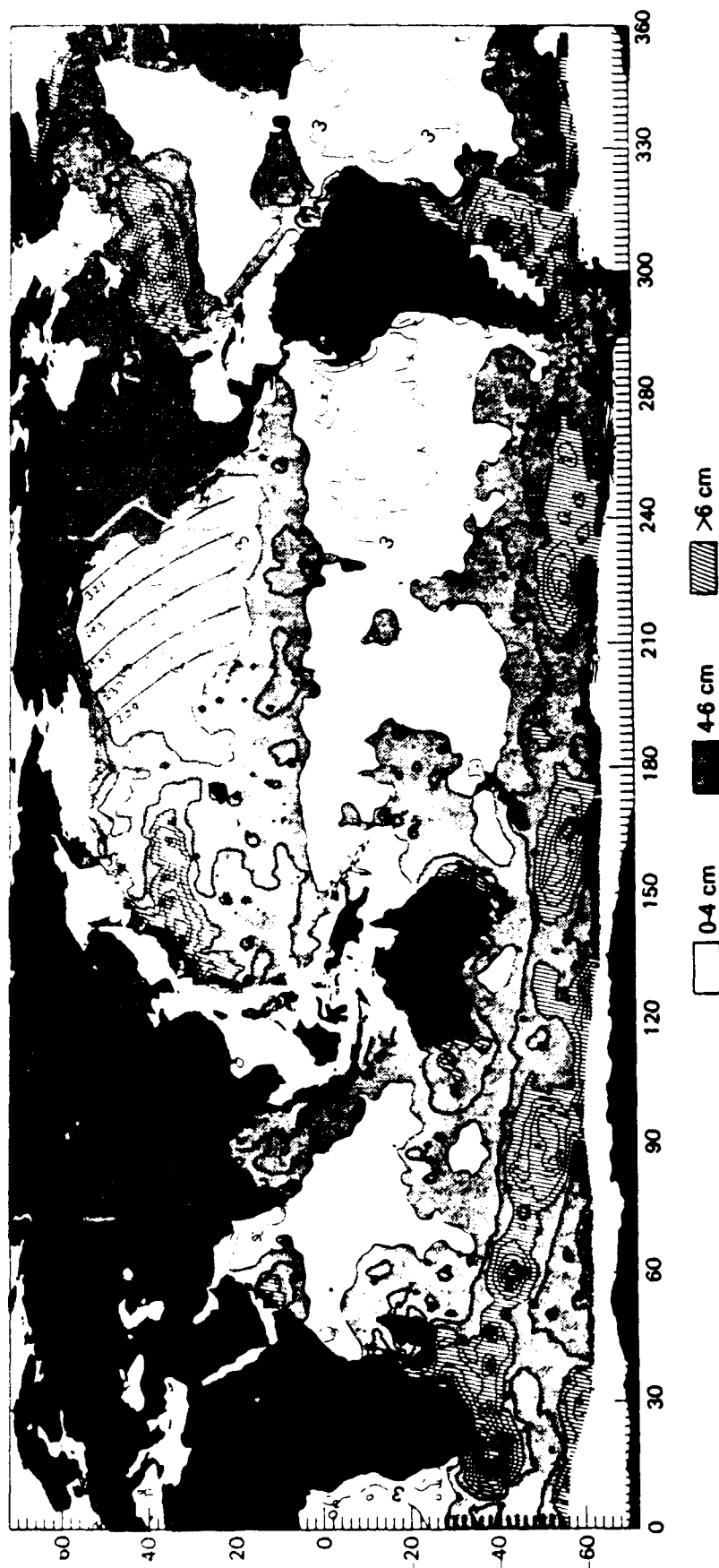


Fig. 3.13 Global mesoscale sea height variability measured by SEASAT, from September 15 to October 10, 1978 (from Cheney et al. [1983]). Five GEOSAT arcs used in comparison are inscribed in the northeast Pacific Ocean.

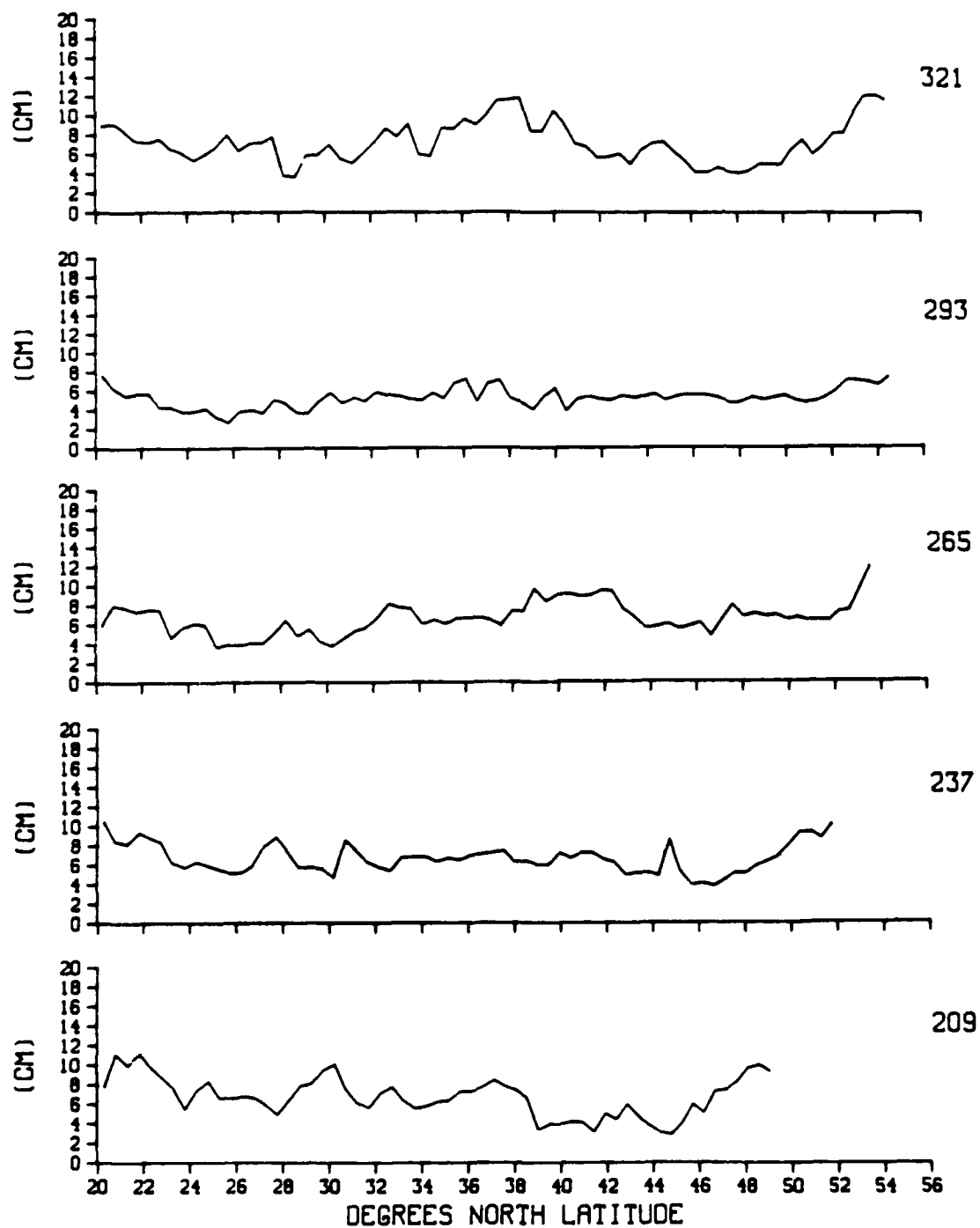


Fig. 3.14 Sea surface height variability (RMS) as a function of latitude, for five GEOSAT arcs.

APPENDIX A

We seek a simple measure of the effect a single spike in a difference profile has on the RMS variability of that profile. For a large number of points N making up the profile, the variability σ is calculated from

$$\sigma = \left(\frac{1}{N} \sum_i^N V_i \right)^{1/2} \quad (1)$$

where the V_i are the squares of the individual sea surface heights on the difference profile. Now suppose that all the V_i but one represent "good" data such that the true variability $\bar{\sigma}$ is the square root of their average, \bar{v} . The remaining "bad" data point is denoted as v' . Separating (1) into good and bad constituents gives the calculated variability σ_c as

$$\sigma_c = \left[\frac{1}{N} (v' + \sum_{i=1}^{N-1} V_i) \right]^{1/2} \quad (2)$$

where for large N , $\frac{1}{N} \sum_{i=1}^{N-1} V_i \approx \bar{v}$. Thus, (2) may be rewritten as

$$\sigma_c \approx \left(\bar{v} + \frac{v'}{N} \right)^{1/2}$$

or

$$\sigma_c \approx \bar{\sigma} \left(1 + \frac{v'}{N\bar{v}} \right)^{1/2} \quad (3)$$

The difference plots have shown that the spike editor keeps individual spikes smaller than 40 cm, corresponding to a v' of 1600 cm². For a conservative $N = 540$ and $\bar{v} = 40$ cm² (from $\bar{\sigma} = 6.3$ cm) this still makes $\frac{v'}{N\bar{v}} \ll 1$ allowing use of the binomial theorem on (3) to give

$$\sigma_c \approx \bar{\sigma} \left(1 + \frac{v'}{2N\bar{\sigma}} \right)$$

or

$$\sigma_c \approx \bar{\sigma} + \frac{v'}{2N\bar{\sigma}} \quad (4)$$

Using equation (4), a difference profile consisting of 540 points with a true variability of 6.0 cm and a spike of 40 cm, will have a calculated variability of 6.25 cm. This variability is not significant compared to the noise bounds discussed in Chapter 2.

The perturbation term in (4) may be approximated by $\frac{v'}{2N\bar{\sigma}_c}$ to estimate the true variability from the calculated variability. This was done occasionally during Chapter 2 when investigating the correction channels and had no bearing on the outcome; mainly because the corrections themselves had no effect on the spikes.

REFERENCES

- Born, G.H. 1988. Geosat orbit determination accuracy-plans for water vapor correction. Geosat Users Meeting, 22 March 1988. Laurel, MD: The Johns Hopkins University.
- Born, G.H., Mitchell, J.L., and Heyler, G.A. 1987. Design of the Geosat exact repeat mission. *Johns Hopkins APL Technical Digest* 8(2): 260-266.
- Born, G.H., Richards, M.A., and Rosborough, G.W. 1982. An empirical determination of the effects of sea state bias on Seasat altimetry. *J. Geophys. Research* 87(C5): 3221-3226.
- Bracewell, R.N. 1986. *The Fourier Transform and its Applications*. Second edition, revised. New York: McGraw-Hill, 474 pp.
- Brown, R.D., and Hutchinson, M.K. 1981. Ocean tide determination from satellite altimetry. In: *Oceanography From Space*, edited by J.F.R. Gower, 897-906. New York: Plenum Press.
- Calman, J. 1987. Introduction to sea-surface topography from satellite altimetry. *Johns Hopkins APL Technical Digest* 8(2): 206-211.
- Cartwright, D.E., and Alcock, G.A. 1981. On the precision of sea surface elevations and slopes from Seasat altimetry of the northeast Atlantic ocean. In: *Oceanography From Space*, edited by J.F. R. Gower, 885-895. New York: Plenum Press.
- Cartwright, D.E., and Edden, A.C. 1973. Corrected tables of tidal harmonics. *Geophys. J. Roy. Soc.* 33:253-264.
- Cartwright, D.E., and Tayler, R.J. 1971. New computations of the tide-generating potential. *Geophys. J. Roy. Soc.* 23:45-74.
- Cheney, R.E., Douglas, B.C., Agreen, R.W., Miller, L.L., and Porter, D.L. 1987. Geosat altimeter geophysical data record (GDR) user handbook. Rockville, MD: NOAA National Ocean Service.
- Cheney, R.E., and Marsh, J.G. 1981. Seasat altimeter observations of dynamic topography in the Gulf Stream region. *J. Geophys. Research* 86(C1):473-483.
- Cheney, R.E., and Marsh, J.G. 1981b. Oceanic eddy variability measured by Geos 3 altimeter crossover differences. *EOS Trans. AGU* 62(45): 743-752.
- Cheney, R.E., Marsh, J.G., and Beckley, B.D. 1983. Global mesoscale variability from collinear tracks of Seasat altimeter data. *J. Geophys. Research* 88(C7): 4343-4354.
- Cheney, R.E., Miller, L.L., Douglas, B.C., and Agreen, R.W. 1987b. Monitoring equatorial Pacific sea level with Geosat. *Johns Hopkins APL Technical Digest* 8(2):245-250.
- Cole, T.D. 1985. Geosat-A data users/ground system interface control document (ICD). Laurel, MD: The Johns Hopkins University Applied Physics Laboratory Report 7292-9510. First revision.

- Diamante, J.M., and Nee, T.S. 1981. Application of satellite radar altimeter data to the determination of regional tidal constituents and the mean sea surface. In: *Oceanography From Space*, edited by J.F. R. Gower, 907-918. New York: Plenum Press.
- Dobson, E., Monaldo, F., Goldhirsh, J., and Wilkerson, J. 1987. Validation of Geosat altimeter-derived windspeeds and significant wave heights using buoy data. *Johns Hopkins APL Technical Digest* 8(2): 222-233.
- Douglas, B.C., Agreen, R.W., and Sandwell, D.T. 1984. Observing global ocean circulation with Seasat altimeter data. *J. Mar. Geod.* 8:67-83.
- Douglas, B.C., and Gaborski, P.D. 1979. Observation of sea surface topography with Geos 3 altimeter data. *J. Geophys. Research* 84 (B8):3893-3896.
- Douglas, B.C., and Goad, C.C. 1978. The role of orbit determination in satellite altimeter data analysis. *Boundary-Layer Meteorology* 13:245-251.
- Fedor, L.S., and Brown, G.S. 1982. Waveheight and wind speed measurements from the Seasat radar altimeter. *J. Geophys. Research* 87(C5): 3254-3260.
- Fu, L.L. 1983. On the wave number spectrum of oceanic mesoscale variability observed by the Seasat altimeter. *J. Geophys. Research* 88(C7):4331-4341.
- Fu, L.L., and Cheiton, D.B. 1984. Temporal variability of the Antarctic circumpolar current observed from satellite altimetry. *Science* 226 (4672):343-346.
- Goldhirsh, J. 1983. Rain cell size statistics as a function of rain rate for attenuation modeling. *IEEE Trans. Antennas Propagat.* AP-31 (5):799-801.
- Goldhirsh, J., and Rowland, J.R. 1982. A tutorial assessment of atmospheric height uncertainties for high precision satellite altimeter missions to monitor ocean currents. *IEEE Trans. Geosci. Remote Sensing* GE-20(4):418-434.
- Hendershott, M.C. 1981. Long waves and ocean tides. In: *Evolution of Physical Oceanography: Scientific Surveys in Honor of Henry Stommel*, edited by B.A. Warren and C. Wunsch, 292-341. Cambridge, MA: The MIT Press.
- Huang, N.E., Leitaio, C.D., and Parra, C.G. 1978. Large-scale Gulf Stream frontal study using Geos 3 radar altimeter data. *J. Geophys. Research* 83(C9): 4673-4682.
- Hurlburt, H.E. 1986. Dynamic transfer of simulated altimeter data into subsurface information by a numerical ocean model. *J. Geophys. Research* 91(C2):2372-2400.
- Jackson, F.C. 1979. The reflection of impulses from a nonlinear random sea. *J. Geophys. Research* 84(C8):4939-4943.
- Jones, S.C., Tossman, B.E., and Dubois, L.M. 1987. The Geosat ground station. *Johns Hopkins APL Technical Digest* 8(2):190-196.
- Lerch, F.J., Klosko, S.M., Laubscher, R.E., and Wagner, C.A. 1979. Gravity model improvement using Geos-3 (GEM 9 and 10). *J. Geophys. Research* 84(B8):3897-3916.

- Lerch, F.J., Putney, B.H., Wagner, C.A., and Klosko, S.M. 1981. Goddard earth models for oceanographic applications (GEM 10B and 10C). *J. Mar. Geod.* 5(2):145-187.
- Lipa, B.J., and Barrick, D.E. 1981. Ocean surface height-slope probability density function from Seasat altimeter echo. *J. Geophys. Research* 86(C11):10921-10930.
- Lorell, J., Colquitt, E., and Anderle, R.J. 1982. Ionospheric correction for Seasat altimeter height measurement. *J. Geophys. Research* 87(C5):3207-3212.
- Lybanon, M., and Crout, R.L. 1987. The NORDA Geosat ocean applications program. *Johns Hopkins APL Technical Digest* 8(2):212-218.
- MacArthur, J.L., Marth, P.C. Jr., and Wall, J.G. 1987. The Geosat radar altimeter. *Johns Hopkins APL Technical Digest* 8(2):176-181.
- Marsh, J.G., and Chang, E.S. 1978. 5' detailed gravimetric geoid in the northwestern Atlantic ocean. *J. Mar. Geod.* 1(3):253-261.
- Marsh, J.G., and Martin, T.V. 1982. The Seasat altimeter mean sea surface model. *J. Geophys. Research* 87(C5):3269-3280.
- Marsh, J.G., Martin, T.V., McCarthy, J.J., and Chovitz, P.S. 1980. Mean sea surface computation using Geos-3 altimeter data. *J. Mar. Geod.* 3:359-378.
- Mather, R.S., Coleman, R., and Hirsch, B. 1980. Temporal variations in regional models of the Sargasso sea from Geos-3 altimetry. *J. Phys. Oceanog.* 10(2):171-185.
- Mazzega, P. 1983. The M2 oceanic tide recovered from Seasat altimetry in the Indian Ocean. *Nature* 302(5908):514-516.
- McNally, G.J. 1981. Satellite-tracked drift buoy observation of the near-surface flow in the eastern mid-latitude North Pacific. *J. Geophys. Research* 86(C9):8022-8030.
- Menard, Y. 1983. Observations of eddy fields in the northwest Atlantic and northwest Pacific by Seasat altimeter data. *J. Geophys. Research* 88(C3):1853-1866.
- Mitchell, J.L. 1983. A position paper: mesoscale oceanography from Geosat. Bay St. Louis, MS:Naval Ocean Research and Development Activity Technical Note 226.
- Monaldo, F.M., Goldhirsh, J., and Walsh, E.J. 1986. Altimeter height measurement error introduced by the presence of variable cloud and rain attenuation. *J. Geophys. Research* 91(C2):2345-2350.
- Mueller, I.I. 1981. Reference coordinate systems for earth dynamics: a preview. In: *Reference coordinate systems for Earth dynamics*, edited by E.M. Gaposchkin and B. Kolaczyk, 1-22. Holland: D. Reidel.
- Munk, W.H., and Cartwright, D.E. 1966. Tidal spectroscopy and prediction. *Philosophical Transactions of the Royal Society of London* 259(1105):533-581.

- Parke, M.E., Stewart, R.H., and Farless, D.L. 1987. On the choice of orbits for an altimetric satellite to study ocean circulation and tides. *J. Geophys. Research* 92(C11):11693-11707.
- Pickard, G.L., and Emery, W.J. 1982. *Descriptive Physical Oceanography, An Introduction*. Fourth edition. New York: Pergamon Press, 249 pp.
- Pond, S., and Pickard, G.L. 1983. *Introductory Dynamical Oceanography*. Second edition. New York: Pergamon Press, 329 pp.
- Prabhakara, C., Short, D.A., and Vollmer, B.E. 1985. El Nino and atmospheric water vapor: observations from Nimbus 7 SMMR. *J. Clim. and Appl. Met.* 24(12):1311-1324.
- Rapp, R.H. 1978. A global $1^\circ \times 1^\circ$ anomaly field combining satellite, Geos-3 altimeter and terrestrial anomaly data. Columbus, OH: The Ohio State U. Research Foundation Scientific Report No. 22.
- Rapp, R.H. 1979. Geos 3 data processing for the recovery of geoid undulations and gravity anomalies. *J. Geophys. Research* 84(B8):3784-3792.
- Rapp, R.H. 1983. The determination of geoid undulations and gravity anomalies from Seasat altimeter data. *J. Geophys. Research* 88(C3):1552-1562.
- Rihaczek, A.W. 1969. *Principles of high resolution radar*. New York: McGraw-Hill, 498 pp.
- Saastamoinen, J. 1972. Atmospheric correction for the troposphere and stratosphere in radio ranging of satellites. *Geophys. Monogr. AGU* 15:247-252.
- Schwidorski, E.W. 1980. On charting global ocean tides. *Reviews of Geophysics and Space Physics* 18(1):243-268.
- Shuhy, J.L., Grunes, M.R., Uliana, E.A., and Choy, L.W. 1987. Comparison of Geosat and ground-truth wind and wave observations: preliminary results. *Johns Hopkins APL Technical Digest* 8(2):219-221.
- Stacey, F.D. 1977. *Physics of the Earth*. Second edition. New York: John Wiley and Sons, 414 pp.
- Stewart, R.H. 1985. *Methods of satellite oceanography*. Berkeley: University of California Press, 360 pp.
- Stommel, H. 1965. *The Gulf Stream: a physical and dynamical description*. Second edition. Berkeley: University of California Press, 248 pp.
- Tai, C.K. 1988. Error assessments of widely-used orbit error approximations in satellite altimetry. Unpublished manuscript.
- Tai, C.K., and Fu, L.L. 1986. On crossover adjustment in satellite altimetry and its oceanographic implications. *J. Geophys. Research* 91(C2):2549-2554.

- Tai, C.K., and Wunsch, C. 1983. Absolute measurement by satellite altimetry of dynamic topography of the Pacific ocean. *Nature* 301(5899):408-410.
- Tapley, B.D., Born, G.H., and Parke, M.E. 1982. The Seasat altimeter data and its accuracy assessment. *J. Geophys. Research* 87(C5):3179-3188.
- Tapley, B.D., Lundberg, J.B., and Born, G.H. 1982b. The Seasat altimeter wet troposphere range correction. *J. Geophys. Research* 87(C5):3213-3220.
- TOPEX Science Working Group. 1981. Satellite altimetric measurements of the ocean. Pasadena, CA: Jet Propulsion Lab. Doc.400-111.
- U.S. Dept. of Commerce Tide Tables. 1986,1987. Rockville, MD: NOAA National Ocean Service.
- Wunsch, C. 1972. Bermuda sea level in relation to tides, weather, and baroclinic fluctuations. *Reviews of Geophysics and Space Physics* 10(1):1-49.
- Wunsch, C., and Gaposchkin, E.M. 1980. On using satellite altimetry to determine the general circulation of the oceans with application to geoid improvement. *Reviews of Geophysics and Space Physics* 18(4):725-745.
- Wyrski, K., Magaard, L., and Hagar, J. 1976. Eddy energy in the oceans. *J. Geophys. Research* 81(15):2641-2646.

ACKNOWLEDGEMENTS

I would like to thank the following persons and organizations for their contributions to this thesis:

My advisor, Dr. Carl Wunsch - for guidance, advice, knowledge, helpful criticism, and being a pleasure to work with.

The United States Navy - for its commitment to graduate education, and funding my stay at M.I.T. and the Woods Hole Oceanographic Institution through the Naval Postgraduate School Civilian Institutions program.

Barbara Grant, Linda Meinke, and especially Charmaine King - for programming assistance, and computing beyond the call of duty. Barbara and Charmaine are supported in part by ONR grant #N00014-85-J-1241, and Linda is supported in part by ONR grant #M00014-86-K-0751.

Dorothy Frank - for rapid, accurate word processing, and the patience to put up with numerous revisions.

Anne Gettelman - for editorial comments, support, and lots of inspiration.

My parents, Dr. Donn V. and Mrs. Jeanne K. Campbell - for instilling a love of learning in their children, and their support throughout my scholastic years.

DOCUMENT LIBRARY

August 9, 1988

Distribution List for Technical Report Exchange

Attn: Stella Sanchez-Wade
Documents Section
Scripps Institution of Oceanography
Library, Mail Code C-075C
La Jolla, CA 92093

Hancock Library of Biology &
Oceanography
Alan Hancock Laboratory
University of Southern California
University Park
Los Angeles, CA 90089-0371

Gifts & Exchanges
Library
Bedford Institute of Oceanography
P.O. Box 1006
Dartmouth, NS, B2Y 4A2, CANADA

Office of the International
Ice Patrol
c/o Coast Guard R & D Center
Avery Point
Groton, CT 06340

Library
Physical Oceanographic Laboratory
Nova University
8000 N. Ocean Drive
Dania, FL 33304

NOAA/EDIS Miami Library Center
4301 Rickenbacker Causeway
Miami, FL 33149

Library
Skidaway Institute of Oceanography
P.O. Box 13687
Savannah, GA 31416

Institute of Geophysics
University of Hawaii
Library Room 252
2525 Correa Road
Honolulu, HI 96822

Library
Chesapeake Bay Institute
4800 Atwell Road
Shady Side, MD 20876

MIT Libraries
Serial Journal Room 14E-210
Cambridge, MA 02139

Director, Ralph M. Parsons Laboratory
Room 48-311
MIT
Cambridge, MA 02139

Marine Resources Information Center
Building E38-320
MIT
Cambridge, MA 02139

Library
Lamont-Doherty Geological
Observatory
Columbia University
Palisades, NY 10964

Library
Serials Department
Oregon State University
Corvallis, OR 97331

Pell Marine Science Library
University of Rhode Island
Narragansett Bay Campus
Narragansett, RI 02882

Working Collection
Texas A&M University
Dept. of Oceanography
College Station, TX 77843

Library
Virginia Institute of Marine Science
Gloucester Point, VA 23062

Fisheries-Oceanography Library
151 Oceanography Teaching Bldg.
University of Washington
Seattle, WA 98195

Library
R.S.M.A.S.
University of Miami
4600 Rickenbacker Causeway
Miami, FL 33149

Maury Oceanographic Library
Naval Oceanographic Office
Bay St. Louis
NSTL, MS 39522-5001

Marine Sciences Collection
Mayaguez Campus Library
University of Puerto Rico
Mayaguez, Puerto Rico 00708

REPORT DOCUMENTATION PAGE	1. REPORT NO. WHOI-88-48	2.	3. Recipient's Accession No.
4. Title and Subtitle Geostrophic Vortex Dynamics		5. Report Date October 1988	
7. Author(s) Lorenzo M. Polvani		8. Performing Organization Rept. No. WHOI-88-48	
9. Performing Organization Name and Address The Woods Hole Oceanographic Institution Woods Hole, Massachusetts 02543, and The Massachusetts Institute of Technology Cambridge, Massachusetts 02139		10. Project/Task/Work Unit No. 11. Contract(C) or Grant(G) No. (C) (G)	
12. Sponsoring Organization Name and Address The Office of Naval Research through the Massachusetts Institute of Technology		13. Type of Report & Period Covered Ph.D. Thesis 14.	
5. Supplementary Notes This thesis should be cited as: Lorenzo M. Polvani, 1988. Geostrophic Vortex Dynamics. Ph.D. Thesis, MIT/WHOI, WHOI-88-48.			
16. Abstract (Limit: 200 words) By generalizing the method of contour dynamics to the quasigeostrophic two-layer model, we have proposed and solved a number of fundamental problems in the dynamics of rotating and stratified vorticity fields. A variety of rotating and translating potential vorticity equilibria (V-states) in one and two layers have been obtained, shedding new light on potential vorticity dynamics in the geostrophic context. In particular, the equivalent barotropic model is shown to be a singular limit of the two-layer model for scales large compared to the radius of deformation. The question of coalescence of two vortices in the same layer (merger) and in different layers (alignment) is studied in detail. Critical initial separation distances for coalescence are numerically established as functions of the radius of deformation and the relative thickness of the layers at rest. The connection between coalescence and the existence of stable rotating double-connected V-states is shown to be an illuminating generalization of the Euler results. The question of filamentation of two-dimensional vorticity interfaces is addressed from a new geometrical perspective. The analysis of the topology of the streamfunction in a frame of reference rotating with the instantaneous angular velocity of the vorticity distribution (the corotating frame) is shown to yield new powerful insights on the nonlinear evolution of the vorticity field. In particular, the presence of hyperbolic (critical) points of the corotating streamfunction that come in contact with the vorticity interface is found to be directly responsible for the generation of filaments. The importance of the position of the critical points of the comoving streamfunction is found to generalize to the two-layer quasigeostrophic context. They are shown to play the crucial role in determining the limits, in parameter space, on the existence of a number of two-layer rotating and translating potential vorticity equilibria.			
17. Document Analysis a. Descriptors 1. Vortices 2. Two-Layer Model b. Identifiers/Open-Ended Terms c. COSATI Field/Group			
18. Availability Statement Approved for publication; distribution unlimited.		19. Security Class (This Report) UNCLASSIFIED	21. No. of Pages 221
		20. Security Class (This Page)	22. Price